

ETD Archive

2012

Computational Analyses for Fluid Flow and Heat Transfer in Different Curved Geometries

Carlin Miller Lucente
Cleveland State University

Follow this and additional works at: <https://engagedscholarship.csuohio.edu/etdarchive>

 Part of the [Mechanical Engineering Commons](#)

[How does access to this work benefit you? Let us know!](#)

Recommended Citation

Lucente, Carlin Miller, "Computational Analyses for Fluid Flow and Heat Transfer in Different Curved Geometries" (2012). *ETD Archive*. 484.

<https://engagedscholarship.csuohio.edu/etdarchive/484>

This Thesis is brought to you for free and open access by EngagedScholarship@CSU. It has been accepted for inclusion in ETD Archive by an authorized administrator of EngagedScholarship@CSU. For more information, please contact library.es@csuohio.edu.

**COMPUTATIONAL ANALYSES FOR FLUID FLOW AND
HEAT TRANSFER IN DIFFERENT CURVED GEOMETRIES**

CARLIN MILLER LUCENTE

Bachelor of Science in Mechanical Engineering

Wright State University

June, 2007

Submitted in partial fulfillment of requirements for the degree

MASTER OF SCIENCE IN MECHANICAL ENGINEERING

At the

CLEVELAND STATE UNIVERSITY

May, 2012

This thesis has been approved for the
Department of Mechanical Engineering
And the College of Graduate Studies by

Dr. Mounir Ibrahim, Thesis Committee Chairperson

Department/Date

Dr. Emily S. Nelson

Department/Date

Dr. Petru S. Fodor

Department/Date

ACKNOWLEDGEMENTS

I would like to thank all of the individuals who have made this advanced degree possible. Without their help, I could not have done this on my own. I would like to express my sincere gratitude to my advisor, Dr. Mounir Ibrahim, for his encouragement, guidance, and support from beginning to end which enabled me to develop a better understanding of the subject. I would also like to thank the rest of my thesis committee, Dr. Emily Nelson and Dr. Petru Fodor for their support and input through this process.

I am indebted to my student colleagues for providing an exciting and fun learning environment. I am especially grateful to Abhinav Gupta for helping me to better understand the FLUENT software and all of his assistance running cases in the lab.

I wish to thank my entire family for their love and support, especially my mom for aiding in the editing and formatting of this thesis.

Thank you so much.

COMPUTATIONAL ANALYSES FOR FLUID FLOW AND HEAT TRANSFER IN DIFFERENT CURVED GEOMETRIES

CARLIN MILLER LUCENTE

ABSTRACT

Three-dimensional Computational Fluid Dynamics (CFD) models were developed to simulate fluid flow and heat transfer in a variety of helical channel geometries: circular and elliptical. Laminar flow was observed for Reynolds number between 200 and 1000. Code validation was done for developing steady laminar flow in a circular curved channel. The CFD results were compared to previous numerical results to verify that the model was producing valid results.

The curve of the channel has a centrifugal effect on the fluid flow creating secondary flow known as Dean cells. This secondary flow moves the location of the maximum axial velocity towards the outer wall of the channel and alters the developing temperature profiles as well. The helical models were designed to assess if the effect of the curve increases the rate of heat transfer when a constant surface temperature is applied to the wall of the channel. Different channel geometries were used to determine the effects on fluid flow and heat transfer in a helical channel.

A channel with a 180° turn was also modeled in two different ways. One with a rounded 180° curve and the other with three perpendicular channels joined together to create a square 180° turn. The three combined channels are typically easier and less

expensive to manufacture, but the fluid flow and heat transfer properties need to be considered before selecting the design.

The helical models produce similar results. The Dean vortices produced in the secondary flow within the fluid aids in the heat transfer properties of the fluid. Of all the helical cases, a horizontal ellipse cross section achieved the highest outlet-inlet temperature difference, especially for higher Reynolds numbers. Even though the horizontal elliptical helix model produced the highest temperature difference, the circular helix model produced the highest percent increase over its straight model. Using a figure of merit to compare the Nusselt numbers and friction factors for each case, the circular helix geometry proved to me the best design option. The three combined channels produced better heat transfer results than the rounded channel for higher Reynolds numbers, with higher mean outlet temperatures. At lower Reynolds numbers, the results were very similar with only a 0.4% difference in results.

TABLE OF CONTENTS

ABSTRACT.....	iv
LIST OF TABLES.....	viii
LIST OF FIGURES.....	ix
NOMENCLATURE.....	xiii
CHAPTER I.....	1
INTRODUCTION.....	1
1.1 Background.....	1
1.2 Objectives of the Research.....	3
1.3 Scope of Work.....	4
CHAPTER II.....	6
LITERATURE REVIEW.....	6
2.1 Review of Literature on Fluid Flow and Heat Transfer in Curved Channels.....	6
2.2 Review of Papers on Fluid Flow and Heat Transfer in Helical Channels.....	8
CHAPTER III.....	10
GOVERNING EQUATIONS.....	10
3.1 Governing Equations.....	10
CHAPTER IV.....	16
CODE VALIDATION AND COMPUTATIONAL MODEL.....	16
4.1 Code Validation.....	16
4.2 Computational Model.....	16
4.3 Mesh Independence.....	20
4.4 Fully Developed Fluid Flow.....	21
CHAPTER V.....	23
CIRCULAR HELICAL CHANNEL.....	23
5.1 Fluid Flow in a Helical Circular Channel.....	23
5.2 Heat Transfer in a Helical Circular Channel.....	28

CHAPTER VI	35
ELLIPTICAL HELICAL CHANNEL.....	35
6.1 Elliptical Helix Model.....	35
6.2 Fluid Flow in a Helical Elliptical Channel.....	38
6.3 Heat Transfer in a Helical Elliptical Channel	46
6.4 Results Comparison	54
CHAPTER VII.....	64
180° CIRCULAR CHANNEL.....	64
7.1 Computational Models.....	64
7.2 Fluid Flow Results	68
7.3 Heat Transfer Results.....	74
CHAPTER VIII.....	80
CONCLUSIONS.....	80
8.1 Conclusions.....	80
8.2 Future Work	82
REFERENCES.....	84

LIST OF TABLES

Table 1.1: CFD Summary	5
Table 5.1: Circular Channel Summary	24
Table 6.1: Horizontal Elliptical Channel Summary	37
Table 6.2: Vertical Elliptical Channel Summary	38
Table 6.3: Outlet-Inlet Temperature Difference (K) Summary	61
Table 6.4: Nusselt Number Summary	62
Table 6.5: Friction Factor Summary	63
Table 7.1: 180° Circular Channel Summary	66
Table 7.2: Temperature Difference Summary for 180° Channel.....	79

LIST OF FIGURES

Figure 3.1: Curved Channel Geometry	12
Figure 3.2: Helical Coordinate System	13
Figure 4.1: Helical Models.....	17
Figure 4.2: Helical Horizontal Mid-Plane Locations.....	18
Figure 4.3: Developing Axial Velocity for a 180° Circular Helix.....	18
Figure 4.4: Developing Axial Velocity for a 360° Circular Helix.....	19
Figure 4.5: Developing Axial Velocity for a 720° Circular Helix.....	19
Figure 4.6: Circular Mesh Cross Sections	20
Figure 4.7: Outlet Axial Velocity Profiles for Mesh Refinement.....	21
Figure 4.8: CFD Code Validation.....	22
Figure 5.1: Developing Axial Velocity Profiles in a Circular Helical Channel (Re = 242, De = 129.4)	25
Figure 5.2: Developing Axial Velocity Profiles in a Circular Helical Channel (Re = 492, De = 263.0)	26
Figure 5.3: Developing Axial Velocity Profiles in a Circular Helical Channel (Re = 900, De = 481.1)	27
Figure 5.4: Developing Temperature Profiles in a Circular Helical Channel (Re = 242, De = 263.0)	30
Figure 5.5: Mean Temperature in a Circular Helical Channel.....	30
Figure 5.6: Developing Temperature Profiles in a Circular Helical Channel (Re = 492, De = 263.0)	31
Figure 5.7: Mean Temperature in a Circular Helical Channel.....	31

Figure 5.8: Developing Temperature Profiles in a Circular Helical Channel ($Re = 900, De = 481.1$)	32
.....	32
Figure 5.9: Mean Temperature in a Circular Helical Channel.....	32
Figure 6.1: Elliptical Mesh Cross Sections.....	36
Figure 6.2: Elliptical Helical Channels.....	36
Figure 6.3: Developing Axial Velocity Profiles in a Horizontal Elliptical Helical Channel ($Re = 242,$ $De = 129.4$)	39
Figure 6.4: Developing Axial Velocity Profiles in a Horizontal Elliptical Helical Channel ($Re = 492,$ $De = 263.0$)	40
Figure 6.5: Developing Axial Velocity Profiles in a Horizontal Elliptical Helical Channel ($Re = 900,$ $De = 481.1$)	41
Figure 6.6: Developing Axial Velocity Profiles in a Vertical Elliptical Helical Channel ($Re = 242,$ $De = 129.4$)	43
Figure 6.7: Developing Axial Velocity Profiles in a Vertical Elliptical Helical Channel ($Re = 492,$ $De = 263.0$)	44
Figure 6.8: Developing Axial Velocity Profiles in a Vertical Elliptical Helical Channel ($Re = 900,$ $De = 481.1$)	45
Figure 6.9: Developing Temperature Profiles in a Horizontal Elliptical Helical Channel ($Re = 242,$ $De = 129.4$)	47
Figure 6.10: Mean Temperature in a Horizontal Elliptical Helical Channel ($Re = 242, De = 129.4$)	48
Figure 6.11: Developing Temperature Profiles in a Horizontal Elliptical Helical Channel ($Re = 492,$ $De = 263.0$)	48
Figure 6.12: Mean Temperature in a Horizontal Elliptical Helical Channel ($Re = 492, De = 263.0$)	49

Figure 6.13: Developing Temperature Profiles in a Horizontal Elliptical Helical Channel ($Re = 900$, $De = 481.1$)	49
Figure 6.14: Mean Temperature in a Horizontal Elliptical Helical Channel ($Re = 900$, $De = 481.1$)	50
Figure 6.15: Developing Temperature Profiles in a Vertical Elliptical Helical Channel ($Re = 242$, $De = 129.4$)	52
Figure 6.16: Mean Temperature in a Vertical Elliptical Helical Channel ($Re = 242$, $De = 129.4$)....	52
Figure 6.17: Developing Temperature Profiles in a Vertical Elliptical Helical Channel ($Re = 492$, $De = 263.0$)	53
Figure 6.18: Mean Temperature in a Vertical Elliptical Helical Channel ($Re = 492$, $De = 263.0$)....	53
Figure 6.19: Developing Temperature Profiles in Vertical Elliptical Helical Channel ($Re = 900$, $De = 481.1$)	54
Figure 6.20: Mean Temperature in a Vertical Elliptical Helical Channel ($Re = 900$, $De = 481.1$)....	54
Figure 6.21: Mean Temperature Comparison for $Re = 242$, $De = 129.4$	56
Figure 6.22: Nusselt Number Comparison for $Re = 242$, $De = 129.4$	57
Figure 6.23: Mean Temperature Comparison for $Re = 492$, $De = 263.0$	58
Figure 6.24: Nusselt Number Comparison for $Re = 492$, $De = 263.0$	59
Figure 6.25: Mean Temperature Comparison for $Re = 900$, $De = 481.1$	60
Figure 6.26: Nusselt Number Comparison for $Re = 900$, $De = 481.1$	61
Figure 6.27: Figure of Merit	64
Figure 7.1: 180° Circular Channel Models	65
Figure 7.2: Cross Sectional Planes for (a) Curved Channel and (b) Squared Channel.....	67
Figure 7.3: Developing Axial Velocity Profiles in 180° Channel ($Re = 242$)	71
Figure 7.4: Developing Axial Velocity Profiles in 180° Channel ($Re = 492$)	72

Figure 7.5: Developing Axial Velocity Profiles in 180° Channel (Re = 900).....	73
Figure 7.6: Developing Temperature Profiles in a 180° Channel (Re = 242)	76
Figure 7.7: Mean Temperature in a 180° Channel (Re = 242)	76
Figure 7.8: Developing Temperature Profiles in a 180° Channel (Re = 492)	77
Figure 7.9: Mean Temperature in a 180° Channel (Re = 492)	77
Figure 7.10: Developing Temperature Profiles in a 180° Channel (Re = 900)	78
Figure 7.11: Mean Temperature in a 180° Channel (Re = 900)	78

NOMENCLATURE

a	Radius of Channel
CFD	Computational Fluid Dynamics
C_p	Specific Heat Capacity
De	Dean Number
D_h	Hydraulic Diameter
h	Heat Transfer Coefficient
k	Thermal Conductivity
Nu	Nusselt Number
P	Pressure
p	Pitch
Pr	Prandtl Number
R	Radius of Curvature
r	Radius
Re	Reynolds Number
Re_{cr}	Critical Reynolds Number
r_s	Surface Radius
T	Temperature
T_s	Surface Temperature
V	Axial Velocity

δ	Curvature Ratio
μ	Dynamic Viscosity
ρ	Density

CHAPTER I

INTRODUCTION

1.1 Background

Fluid flow and heat transfer in curved and helical channels are of practical and fundamental interest in engineering as well as other fields. Helical heat exchangers are becoming more commonly used as a means to increase the amount of heat transfer in a small space as a helical heat exchanger utilizes a fraction of the space compared to a straight channel heat exchanger of equivalent length. Fluid flow through curved channels has become of interest to the medical field as it applies to blood flow through the arteries of the body. Siggers and Waters (2005) simulated blood flow through a curved artery to determine the sites at which plaques develop.

The key parameter for that determines whether pipe flow is laminar or turbulent is a dimensionless number known as Reynolds number (Re). Reynolds number is the ratio of inertial forces to viscous forces on a fluid.

$$Re = \frac{\rho V D_h}{\mu}$$

The Reynolds number is based on the density of the fluid (ρ), fluid velocity (V), hydraulic diameter (D_h), and dynamic viscosity (μ). The hydraulic diameter is as

$$D_h = \frac{4A_c}{P_w}$$

where A_c is the cross-sectional area of the pipe and P_w is the wetted perimeter of the pipe.

Flow through a curved channel develops secondary flow due to centrifugal effects acting on the fluid. Dean (1928) showed that flow through a curved channel depends on a non-dimensional parameter known as the Dean number.

$$De = Re\sqrt{2\delta}$$

The Dean number is based on Reynolds number for the axial velocity of the fluid and the curvature ratio (δ). The curvature ratio is based on the radius of the channel (a) and the radius of curvature of the channel (R).

$$\delta = \frac{a}{R}$$

This secondary flow creates Dean vortices, which allow the fluid to circulate within the primary flow. Zitny et al. (2004) utilized a bend in a pipe as a flow inverter to observe the effect on heat transfer. The use of CFD software showed that the effects on the fluid flowing through the bent pipe increased the heat transfer of the fluid. Nusselt number (Nu) was calculated for the bent pipe as well as a straight pipe for comparison.

$$Nu = \frac{hD_h}{k}$$

The Nusselt number is based on the local heat transfer coefficient (h), hydraulic diameter (D_h), and thermal conductivity of the fluid (k). The Nusselt number increases as the heat transfer of the fluid increases. The friction factor is analyzed for design considerations of the channel geometries.

$$f = \frac{\Delta P}{\frac{1}{2}\rho V^2}$$

The friction factor is based on the pressure drop (P), density (ρ), and velocity (V). An increase in friction factor could contribute to an increase in operating costs of a system.

Typically in curved geometries, two symmetric vortices appear in the channel. Both Yang and Keller (1986) and Nobari and Amani (2009) show that at higher Dean numbers, above 522, the secondary flow becomes unstable, developing more than two vortices within the fluid or even eliminating the vortices altogether. In the cases for this thesis, the Dean number will remain below 522 for stability, the limit for stability given by Nobari and Amani (2009).

One of the attributes of fluid flow through a helical coil is the critical Reynolds number, the point at which laminar flow begins to transition to turbulent flow. The critical Reynolds number for fluid flow through a straight channel is 2300. The critical Reynolds number for a helical channel is higher than that of a straight channel, allowing the flow to remain laminar at higher Reynolds numbers. Grundmann (1984) developed a correlation for the critical Reynolds number of a helically coiled channel.

$$Re_{cr} = 2300 \left[1 + 8.6 \left(\frac{a}{R} \right)^{0.45} \right]$$

This correlation allows for an increase in the critical Reynolds number allowing the flow to stay in the laminar phase for a longer period of time.

1.2 Objectives of the Research

Heat exchangers are used in many aspects of the engineering industry. As curved and helical heat exchangers become increasingly more popular, more research is needed to study the effects of the curvature on the fluid flow and heat transfer.

The majority of the research for curved and helical heat exchangers has been done on pipes with circular or rectangular cross sections. One aspect this thesis aims to

observe is the effect of the secondary flow on other geometric cross sections to see if the heat transfer properties can be optimized by using a different cross sectional shape. Specifically, a helical channel with an elliptical cross section will be studied to observe the secondary flow and its effects.

1.3 Scope of Work

In this study, laminar flow models are created for a circular helical channel to observe the effects of the curve of the helix on the fluid and compare it to existing experimental and CFD data. A constant surface temperature is also applied to examine the effects of the secondary flow on the temperature distribution within the fluid.

Two additional laminar models were created for helical channels with the same cross sectional area, but with an elliptical shape, one in a horizontal position and one in a vertical position. The curvature effects on the elliptical geometries were observed and compared to the circular geometry. Models were created for all three cross sectional geometries in a straight channel to compare the effects and benefits, if any, of the curve of the helix.

Two laminar models were also created for a channel making a net 180° turn; the first with a rounded curve and the second combining three perpendicular channels to create a 180° turn. These models compared the effects of sharp 90° turns against a smooth rounded turn and determined which model is a better design case for fluid flow and heat transfer purposes.

A summary of all CFD models is shown in Table 1.1, each case was considered for three different Reynolds numbers. A heat transfer analysis was also done for each model by applying a constant surface temperature of 360 K.








Re	242, 492, 900			
De	129.4, 263.0, 481.1			
Geometry	Straight	Circular	Horizontal Ellipse	Vertical Ellipse
				
	Helical	Circular	Horizontal Ellipse	Vertical Ellipse
				
	180° Turn	Curved	Square	
				
Fluid	Air			
Inlet Temperature	300 K			
Surface Temperature	360 K			

Table 1.1: CFD Summary

CHAPTER II

LITERATURE REVIEW

2.1 Review of Literature on Fluid Flow and Heat Transfer in Curved Channels

Nobari and Amani (2009) conducted a numerical analysis to study fluid flow and heat transfer in a curved pipe for applications in heat exchangers and the cooling of gas turbine blades. They defined the model using non-dimensional representations for the continuity, momentum, and energy equations in toroidal coordinates. Data was calculated for Prandtl numbers 0.5 and 1.0 and for Dean numbers between 76 and 522. For the heat transfer analysis, two different thermal boundary conditions were used: constant wall temperature and constant heat flux at the wall. Five different curvature ratios were analyzed to encompass a range of loose and tightly curved pipes. They demonstrate that due to centrifugal effects, the location of maximum axial velocity shifts from the center of the pipe towards the outer wall along the entrance region. They note that on the outer wall the thickness of axial flow boundary layer decreases while it increases on the inner wall. Due to strengthening centrifugal forces, as the Dean number increases, the location of axial maximum velocity moves closer to the outer wall. Their evaluation of the relationship between hydrodynamic and thermal entrance length and the Reynolds number in curved pipes in terms of curvature ratios show the difference for

smaller and larger ratios. The hydrodynamic entrance lengths increase as curvature ratios decrease. This was shown for smaller ratios, less than $1/7$. For larger curvature ratios the entrance lengths is dependent only on the Reynolds number. They observed the same trend for thermal entrance lengths. Because curvature ratio has minimal effect on entrance lengths except for very small ratios, Dean number as a function of Reynolds number is not significant when considering entrance length. Their results indicate that the Nusselt number increases as the Dean number increases which is achieved with either the increase of the Reynolds number or the curvature of the pipe. They conclude that regardless of inlet profiles, maximum heat transfer rates occur in the entrance region.

Agrawal, et al. (1978) conducted an experimental investigation of the development of steady laminar incompressible flow in the entry region of a curved pipe. They used two semicircular pipes with curvature ratios of $1/20$ and $1/7$ and Dean number ranges from 138 to 679. Using laser anemometry they measured the axial velocity and a component of secondary velocity. Both curved pipes had the same internal diameter but each had different curvature ratios. They took axial velocity measurements at five horizontal planes perpendicular to the cross section for both pipes and secondary velocity at six stations within the pipe of curvature ratio $1/7$. Due to symmetry in the plane of the pipe access, the researchers reported only the measurements taken in the lower half of the pipe. The data was plotted to show the developing axial flow profile at each of the planes. Results similar to Nobari and Amani (2009) are seen with the location of the maximum axial velocity shifting towards the outer wall of the channel as the profile develops.

2.2 Review of Papers on Fluid Flow and Heat Transfer in Helical Channels

Grundmann (1985) looked at critical Reynolds number and friction factor of a helical pipe coil. Because of the secondary flow in curved pipes the critical Reynolds number increases and depends on the curvature ratio. This critical Reynolds number of a helical coil can be substantially greater than that of a straight pipe with the same diameter. Grundmann developed a correlation of critical Reynolds number for laminar and turbulent flow in smooth pipes with an equation based on the Reynolds number, pipe diameter and curvature diameter. This correlation can be applied to create a correlation for the friction factor, which can then be used to calculate the pressure drop across a helical pipe.

Jayakumar et al. (2008) conducted both an experimental and numerical analysis for heat transfer in a helical coil, using water as their fluid. For their experiment they enclosed a helical coil in a vessel that was done to simulate the shell side of a heat exchanger. The cold fluid flowed upward through a bottom connection. They measured inlet and outlet temperatures using resistance temperature detector (RTD). They recorded measurements after steady values for temperature were attained. The experiments were conducted for five different flow rates and for three different temperatures at the inlet. For the numerical analysis model they used the computational fluid dynamic (CFD) FLUENT software. They considered the transport in thermal properties of the fluid to be temperature dependent. They analyzed heat transfer to the fluid flowing inside a helical tube, heated by a constant surface temperature at the wall. The model consisted of hot water entering the helical coil at the top. There, the boundary condition was the velocity inlet boundary. Water exited at the bottom, which had a pressure outlet boundary

condition. They analyzed data for varying inlet conditions. Their results show maximum velocity is located at the coil's outer side. In their conclusions, a key observation cited is that the use of constant values for thermal and transport properties of the fluid inaccurately predicts heat transfer coefficients.

CHAPTER III

GOVERNING EQUATIONS

3.1 Governing Equations

The motion of a laminar, Newtonian fluid is governed by the Navier-Stokes equations. These equations are fundamental partial differential equations that describe incompressible fluid flow. Applying Newton's Second Law, Cengel and Cimbala (2006) supplies the momentum equations for incompressible flow through a straight circular channel in cylindrical coordinates, they are as follows:

$$\begin{aligned} \rho \left(\frac{\partial u_r}{\partial t} + u_r \frac{\partial u_r}{\partial r} + \frac{u_\theta}{r} \frac{\partial u_r}{\partial \theta} + u_z \frac{\partial u_r}{\partial z} - \frac{u_\theta^2}{r} \right) \\ = -\frac{\partial P}{\partial r} + \mu \left[\frac{1}{r} \frac{\partial}{\partial r} \left(r \frac{\partial u_r}{\partial r} \right) + \frac{1}{r^2} \frac{\partial^2 u_r}{\partial \theta^2} + \frac{\partial^2 u_r}{\partial z^2} - \frac{u_r}{r^2} - \frac{2}{r^2} \frac{\partial u_\theta}{\partial \theta} \right] \end{aligned}$$

$$\begin{aligned} \rho \left(\frac{\partial u_\theta}{\partial t} + u_r \frac{\partial u_\theta}{\partial r} + \frac{u_\theta}{r} \frac{\partial u_\theta}{\partial \theta} + u_z \frac{\partial u_\theta}{\partial z} - \frac{u_r u_\theta}{r} \right) \\ = -\frac{1}{r} \frac{\partial P}{\partial \theta} + \mu \left[\frac{1}{r} \frac{\partial}{\partial r} \left(r \frac{\partial u_\theta}{\partial r} \right) + \frac{1}{r^2} \frac{\partial^2 u_\theta}{\partial \theta^2} + \frac{\partial^2 u_\theta}{\partial z^2} + \frac{2}{r^2} \frac{\partial u_r}{\partial \theta} - \frac{u_\theta}{r^2} \right] \end{aligned}$$

$$\rho \left(\frac{\partial u_z}{\partial t} + u_r \frac{\partial u_z}{\partial r} + \frac{u_\theta}{r} \frac{\partial u_z}{\partial \theta} + u_z \frac{\partial u_z}{\partial z} \right) = -\frac{\partial P}{\partial z} + \mu \left[\frac{1}{r} \frac{\partial}{\partial r} \left(r \frac{\partial u_z}{\partial r} \right) + \frac{1}{r^2} \frac{\partial^2 u_z}{\partial \theta^2} + \frac{\partial^2 u_z}{\partial z^2} \right]$$

The Conservation of Mass law for a fluid with constant properties gives the continuity equation in cylindrical coordinates as:

$$\frac{1}{r} \frac{\partial ru_r}{\partial r} + \frac{1}{r} \frac{\partial u_\theta}{\partial \theta} + \frac{\partial u_z}{\partial z} = 0$$

The energy equation for incompressible flow through a straight circular channel in cylindrical coordinates is

$$\frac{\partial T}{\partial t} + u_z \frac{\partial T}{\partial z} + u_r \frac{\partial T}{\partial r} = \left(\frac{k}{\rho c} \right) \left[\frac{1}{r} \frac{\partial}{\partial r} \left(r \frac{\partial T}{\partial r} \right) + \frac{1}{r^2} \frac{\partial^2 T}{\partial \theta^2} + \frac{\partial^2 T}{\partial z^2} \right]$$

Air at low speeds can be considered an incompressible fluid, so these equations are applicable for this thesis.

When considering flow through a curved channel, the curvature ratio must be taken into consideration. The curvature ratio (δ) is the ratio of the radius of the channel to the radius of the curve of the channel. The equation for the curvature ratio is

$$\delta = \frac{a}{R}$$

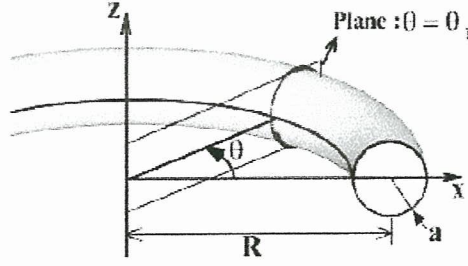


Figure 3.1: Curved Channel Geometry

Flow through curved channels depends on the non-dimensional parameter known as the Dean number. The Dean number is the ratio of viscous forces to the centrifugal forces acting on the fluid. The Dean number is defined as

$$De = \frac{\rho V D}{\mu} \sqrt{2 \frac{a}{R}} = Re_D \sqrt{2 \frac{a}{R}}$$

Dean (1928) determined that the momentum and continuity equations for the steady motion of incompressible fluid. The momentum equations are given below in cylindrical coordinates.

$$u_r \frac{\partial u_r}{\partial r} + u_z \frac{\partial u_r}{\partial z} - \frac{u_\theta}{r} = -\frac{\partial}{\partial r} \left(\frac{P}{\rho} \right) + \frac{\mu}{\rho} \left(\frac{\partial^2 u_r}{\partial r^2} + \frac{1}{r} \frac{\partial u_r}{\partial r} + \frac{\partial^2 u_r}{\partial z^2} - \frac{u_r}{r^2} \right)$$

$$u_r \frac{\partial u_\theta}{\partial r} + u_z \frac{\partial u_\theta}{\partial z} - \frac{u_r u_\theta}{r} = -\frac{1}{r} \frac{\partial}{\partial \theta} \left(\frac{P}{\rho} \right) + \frac{\mu}{\rho} \left(\frac{\partial^2 u_\theta}{\partial r^2} + \frac{1}{r} \frac{\partial u_\theta}{\partial r} + \frac{\partial^2 u_\theta}{\partial z^2} - \frac{u_\theta}{r^2} \right)$$

$$u_r \frac{\partial u_z}{\partial r} + u_z \frac{\partial u_z}{\partial z} = -\frac{\partial}{\partial z} \left(\frac{P}{\rho} \right) + \frac{\mu}{\rho} \left(\frac{\partial^2 u_z}{\partial r^2} + \frac{1}{r} \frac{\partial u_z}{\partial r} + \frac{\partial^2 u_z}{\partial z^2} \right)$$

The continuity equation for flow in a curved channel is as follows:

$$\frac{\partial u_r}{\partial r} + \frac{u_r}{r} + \frac{\partial u_z}{\partial z} = 0$$

Germano (1982, 1989) takes Dean's equations for flow in a curved channel and applies them to a case for a helical channel with a circular cross section. The geometry used by Germano is shown in Figure 3.2.

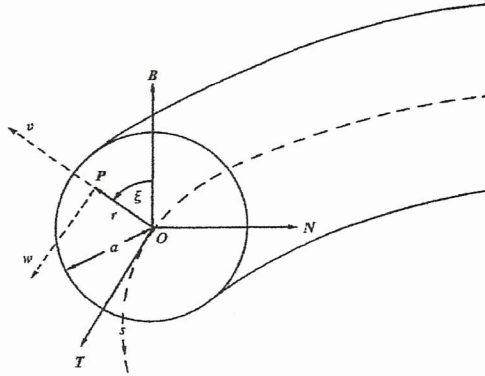


Figure 3.2: Helical Coordinate System

The governing momentum equations for symmetric helical channel are as follows:

$$\begin{aligned} v \frac{\partial u}{\partial r} + \frac{w}{r} \frac{\partial u}{\partial \xi} + \omega u \left(\frac{aR}{R^2 + p^2} \right) \left(v \sin \xi + w \cos \xi - \lambda \frac{\partial u}{\partial \xi} \right) \\ = -\omega \frac{\partial P}{\partial s} + \omega \lambda \left(\frac{aR}{R^2 + p^2} \right) \frac{\partial p}{\partial \xi} + \frac{1}{Re} \left(\frac{1}{r} \frac{\partial \beta}{\partial \xi} - \frac{\partial \gamma}{\partial r} - \frac{\gamma}{r} \right) \\ v \frac{\partial v}{\partial r} + \frac{w}{r} \frac{\partial v}{\partial \xi} - \frac{w^2}{r} - \omega u \left(\frac{aR}{R^2 + p^2} \right) \left(u \sin \xi + \lambda \frac{\partial v}{\partial \xi} \right) \\ = -\frac{\partial P}{\partial r} - \frac{1}{Re} \left[\frac{1}{r} \frac{\partial \alpha}{\partial \xi} + \omega \left(\frac{aR}{R^2 + p^2} \right) \left(\alpha \cos \xi + \lambda \frac{\partial \gamma}{\partial \xi} \right) \right] \end{aligned}$$

$$\begin{aligned}
& v \frac{\partial w}{\partial r} + \frac{w}{r} \frac{\partial w}{\partial \xi} + \frac{vw}{r} - \omega u \left(\frac{aR}{R^2 + p^2} \right) \left(u \cos \xi + \lambda \frac{\partial w}{\partial \xi} \right) \\
& = -\frac{1}{r} \frac{\partial P}{\partial \xi} + \frac{1}{Re} \left[\frac{\partial \alpha}{\partial r} + \omega \left(\frac{aR}{R^2 + p^2} \right) \left(\alpha \sin \xi + \lambda \frac{\partial \beta}{\partial \xi} \right) \right]
\end{aligned}$$

The continuity equation is shown below.

$$\frac{\partial v}{\partial r} + \frac{1}{r} \frac{\partial w}{\partial \xi} + \frac{v}{r} + \omega \left(\frac{aR}{R^2 + p^2} \right) \left(v \sin \xi + w \cos \xi - \lambda \frac{\partial u}{\partial \xi} \right) = 0$$

Where

$$\omega = \frac{1}{1 + r \left(\frac{aR}{R^2 + p^2} \right) \sin \xi}$$

$$\alpha = \frac{\partial w}{\partial r} + \frac{w}{r} - \frac{1}{r} \frac{\partial v}{\partial \xi}$$

$$\beta = \frac{1}{r} \frac{\partial u}{\partial \xi} + \omega \left(\frac{aR}{R^2 + p^2} \right) \left(u \cos \xi + \lambda \frac{\partial w}{\partial \xi} \right)$$

$$\gamma = -\frac{\partial u}{\partial r} - \omega \left(\frac{aR}{R^2 + p^2} \right) \left(u \sin \xi + \lambda \frac{\partial v}{\partial \xi} \right)$$

Kays, Crawford and Weigard (2005) give the boundary conditions for a channel with constant surface temperature as the following:

$$T = T_s, \text{ at } r = r_s$$

$$\frac{\partial T}{\partial r} = 0, \text{ at } r = 0$$

The equations in this chapter along with the given boundary conditions are necessary to solve the given models correctly. For this thesis, the models were solved numerically

using the CFD software, FLUENT. FLUENT is a computer program used for modeling fluid flow and heat transfer in complex geometries. The model geometry and meshes were generated using GAMBIT software, a preprocessor for FLUENT. Boundary conditions were also identified in the GAMBIT models, numerical values for the boundaries were further defined in FLUENT.

CHAPTER IV

CODE VALIDATION AND COMPUTATIONAL MODEL

4.1 Code Validation

Code validation is an important part of the modeling process. Validation compares the computational model to reliable experimental or numerical data. The accuracy of the model will be determined by how closely the model resembles the existing data. For this thesis, a circular curved model will be compared to measured data done by Adler (1934) and CFD data by Nobari and Amani (2009) for fully developed laminar fluid flow. This comparison is to ensure that the model is providing accurate data.

4.2 Computational Model

The circular curved channel geometry was defined in GAMBIT for input into the FLUENT software. The cross section of the channel had a diameter of 25.4 mm and a channel curvature of 88.9 mm, producing a curvature ratio of 1/7. Air was chosen as the fluid because the existing data that the model will be compared to used $Pr = 0.5$ and 1.0 , and air has a $Pr = 0.7$. The constant fluid properties of air from the FLUENT software were used ($\rho = 1.204 \text{ kg/m}^3$, $k = 0.02514 \text{ W/m}\cdot\text{K}$, $\mu = 1.825\text{E-}5 \text{ kg/m}\cdot\text{s}$, and $C_p = 1.005$

kJ/kg·K) for the CFD model. The channel was modeled with a velocity inlet and pressure outlet. A uniform inlet flow velocity was given as 0.2985 m/s which corresponded to a Reynolds number of 492 and a Dean number of 263 which were the values from the existing data that the CFD model will be compared to. The helix spirals downward with a pitch of 30 mm.

In order to compare the model to the existing data, it must be determined when the flow is fully developed. Smaller geometries will reduce computational time, but it must be certain the model will produce the necessary data. To observe the developing flow field, helical models with the same cross section were created for 180°, 360°, and 720° turns. The mesh used for each model had the same element size. These models can be seen in Figure 4.1. The inlet for each channel is shown in blue.

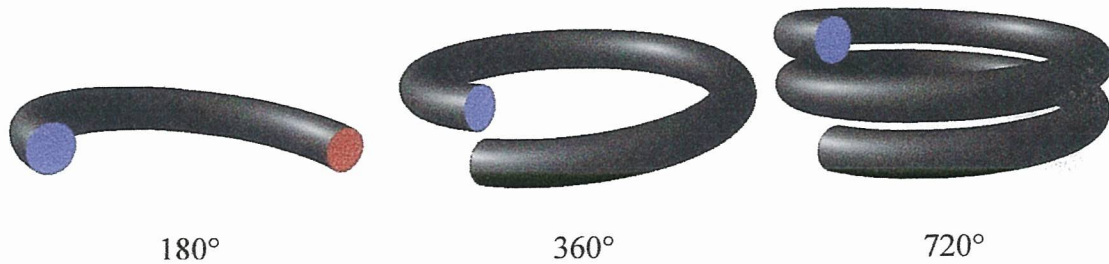


Figure 4.1: Helical Models

The velocity profile was observed at 30° increments along each helical channel. The axial velocity was taken at the horizontal mid-plane of the channel at each increment. Figure 4.2 shows the layout of the cross sectional increments and the corresponding horizontal mid-plane for the 360° channel.

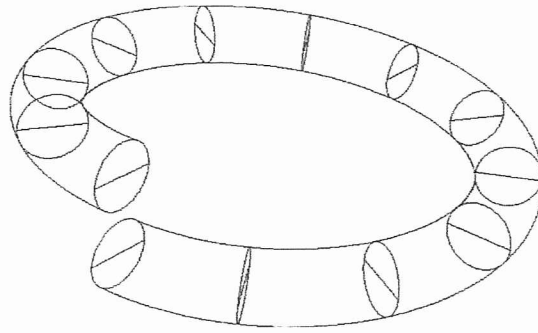


Figure 4.2: Helical Horizontal Mid-Plane Locations

The axial velocity profiles at each 30° increment are plotted against each other to determine when the flow is fully developed. The developing flow profiles for each model can be seen in Figure 4.3, Figure 4.4, and Figure 4.5. Both the axial velocity and the radius are expressed in non-dimensional form. The outer wall of the channel for the data is at $r = -1.00$ and the inner wall is at $r = 1.00$.

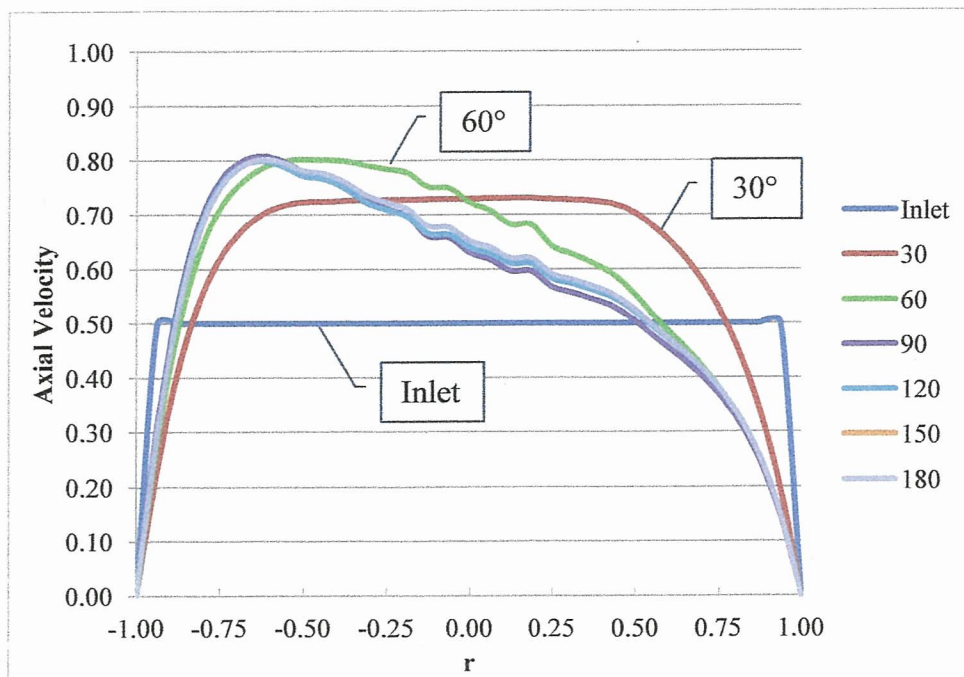


Figure 4.3: Developing Axial Velocity for a 180° Circular Helix

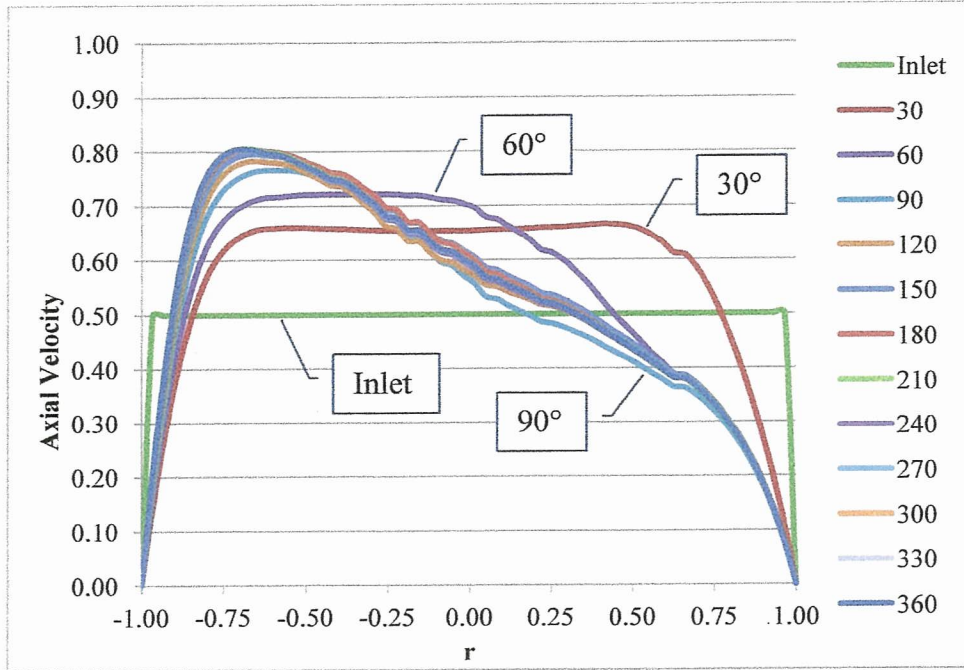


Figure 4.4: Developing Axial Velocity for a 360° Circular Helix

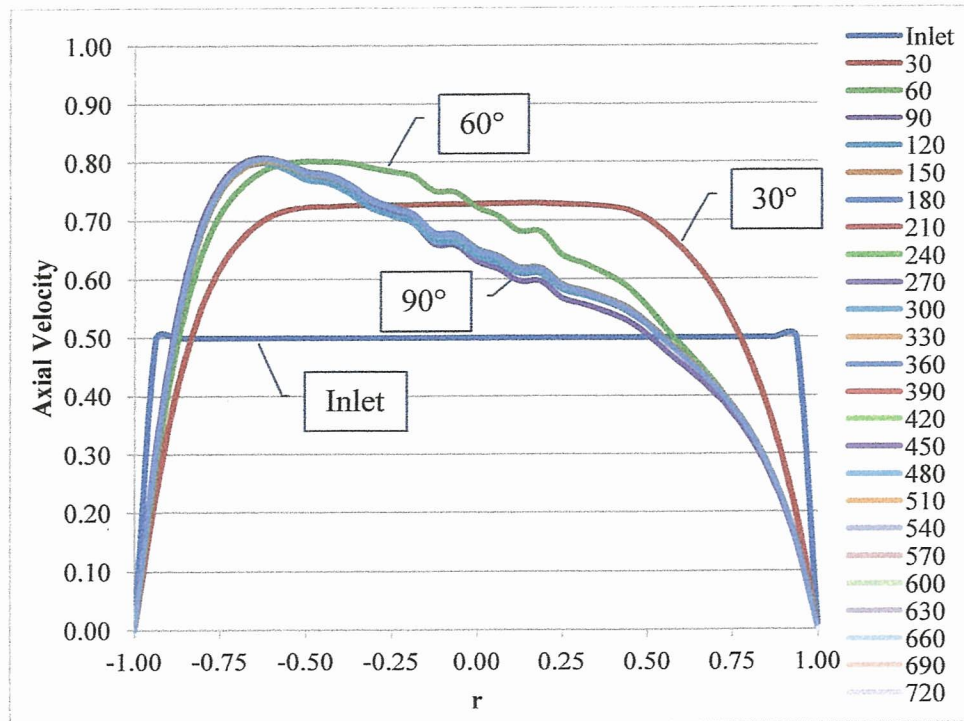


Figure 4.5: Developing Axial Velocity for a 720° Circular Helix

Figure 4.4 shows that at one full turn (360°) the flow is fully developed as the velocity profiles have begun to overlap one another. For further data collection, the 360° helical model will be used to provide sufficient data.

4.3 Mesh Independence

The 360° helix model was evaluated further to ensure that the appropriate mesh size was used so that the results are independent of the mesh size. It is important to refine the mesh to get the most accurate results, but a model with an overly refined mesh can greatly increase the computational time. The mesh for the 360° helix was refined twice into a medium sized mesh and a fine mesh. The coarse mesh which was used to determine fully developed flow has 335,580 elements. The medium mesh has 770,040 elements and the fine mesh has 2,542,248 elements. A cross-sectional view of the three meshes is shown in Figure 4.6.

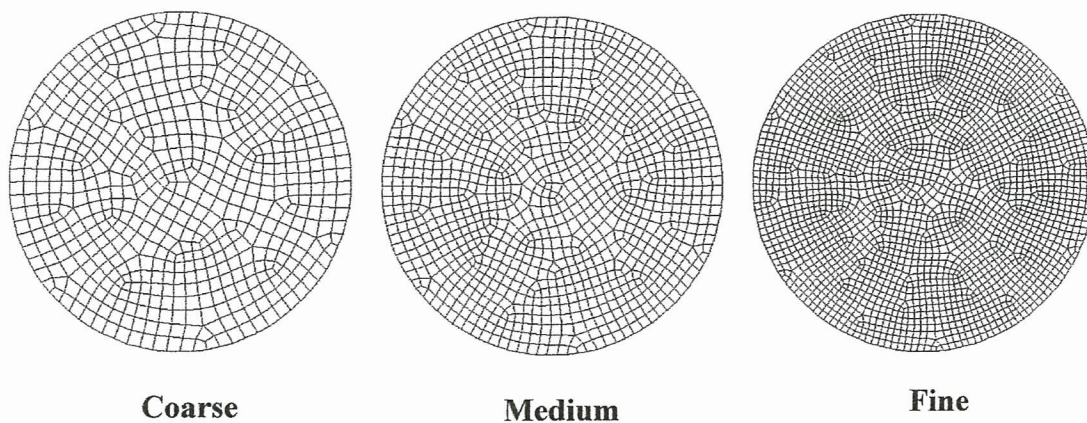


Figure 4.6: Circular Mesh Cross Sections

To determine mesh independence the axial velocity profiles were again taken along the horizontal mid-plane of the channel. The axial velocity profiles for each mesh at the outlet of the channel are plotted against each other and shown in Figure 4.7. Both the axial velocity and the radius have been non-dimensionalized.

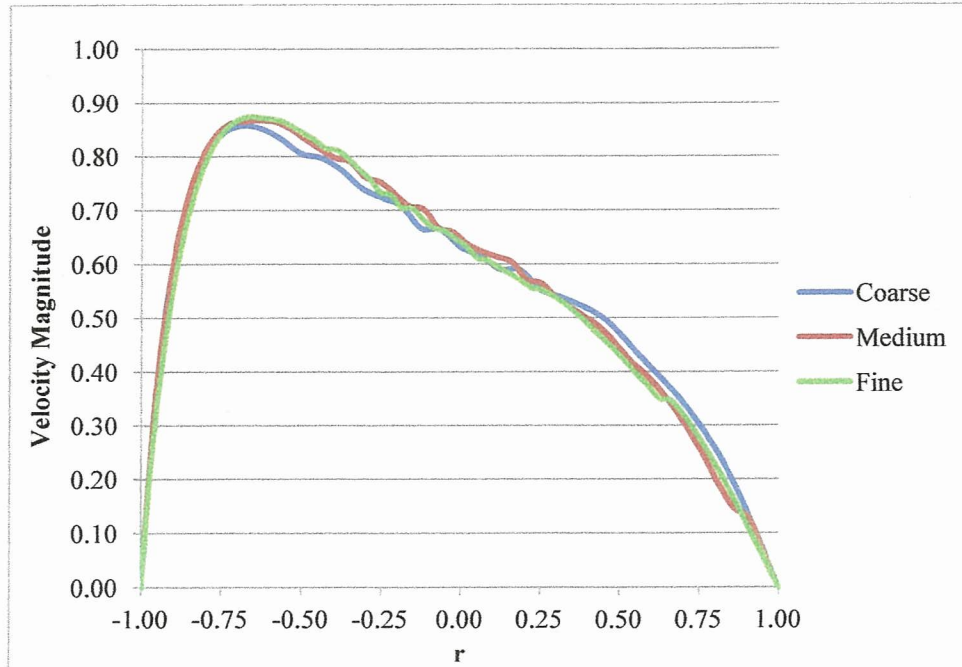


Figure 4.7: Outlet Axial Velocity Profiles for Mesh Refinement

All three meshes produce similar results, but if examined closely, the data for the coarse mesh does not quite line up with the results of the medium and fine meshes. The minimal difference between the medium and fine meshes indicates the data is independent of mesh size. The medium sized mesh was used to save on computational time.

4.4 Fully Developed Fluid Flow

Since it has been determined that the axial velocity is fully developed and the data is independent of the mesh size, the model can now be compared to the existing data by Adler (1934) and Nobari and Amani (2009). Figure 4.8 shows the comparison of the data from the computational model and the existing data.

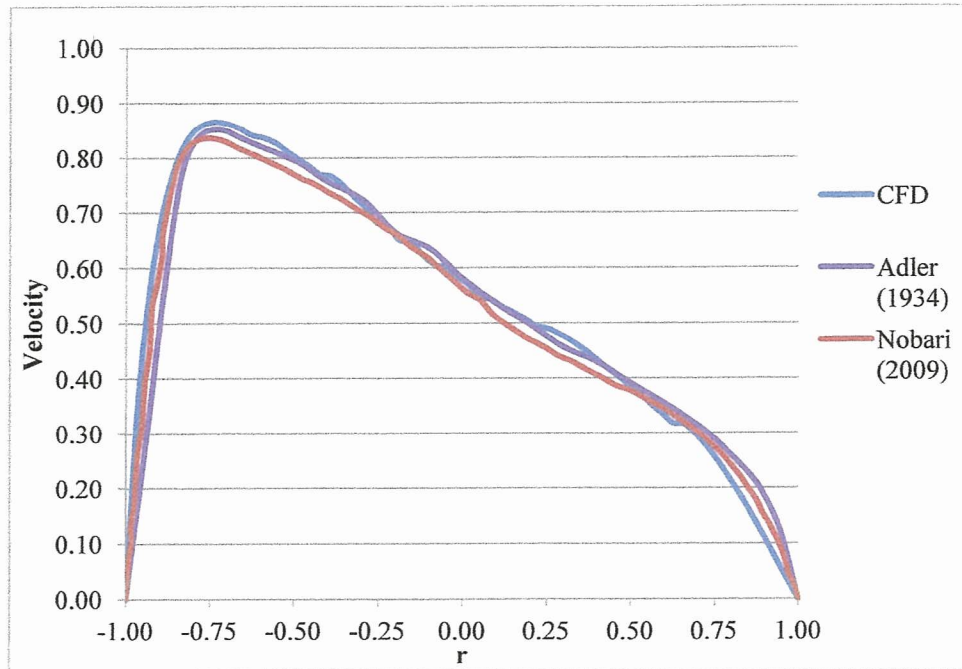


Figure 4.8: CFD Code Validation

The CFD model shows similar results to that of Adler's measured results and Nobari and Amani's CFD data. All three sets of data show the location of the maximum axial velocity shift towards the outer wall of the channel. The data shown in Figure 4.8 validates the code for the CFD model.

CHAPTER V

CIRCULAR HELICAL CHANNEL

5.1 Fluid Flow in a Helical Circular Channel

The 360° circular helix model used for the code validation is used again to observe the effects on the fluid for different Reynolds numbers. Two additional laminar flow situations were simulated for Reynolds numbers of 242 and 900. These Reynolds numbers were selected as they were used for data in Nobari and Amani (2009). For comparison, a straight circular channel model of equivalent length is created to observe the difference between the behaviors of the fluid flow through a straight channel and a helical channel. The information for each of the models is shown in Table 5.1.

Model	Circular Helix Model			Circular Straight Model		
Abbreviation	CH			CS		
Diameter	25.4 mm			25.4 mm		
Curvature Radius	88.9 mm			N/A		
Curvature Ratio	1/7			N/A		
Pitch	30.0 mm			N/A		
Inlet Velocity	0.1468 m/s	0.2985 m/s	0.5461 m/s	0.1468 m/s	0.2985 m/s	0.5461 m/s
Reynolds Number	242	492	900	242	492	900
Dean Number	129.4	263	481.1	N/A	N/A	N/A
Inlet Temperature	300 K					
Surface Temperature	360 K					

Table 5.1: Circular Channel Summary

Figure 5.1, Figure 5.2, and Figure 5.3 show the developing axial velocity profiles of the straight channel and the helical channel, as well as the axial velocity vectors of the helical channel for each of the three Reynolds numbers. The cross sections are shown at 60° increments in the channel. The cross sections for the straight channel are at locations the equivalent length of the 60° arc of the helical channel. The outer wall of the helical channel is shown on the left of the figures.

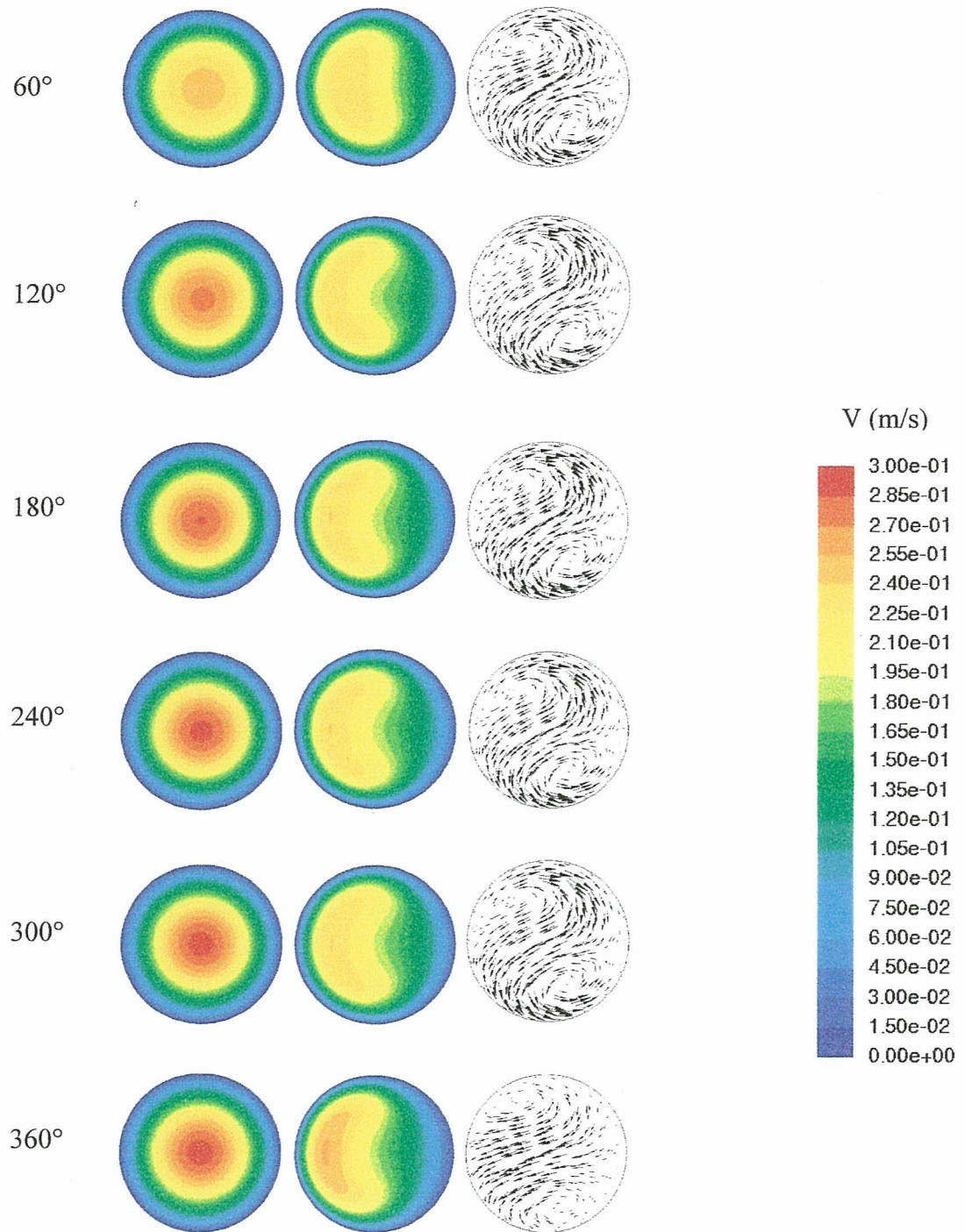


Figure 5.1: Developing Axial Velocity Profiles in a Circular Helical Channel ($Re = 242$, $De = 129.4$)

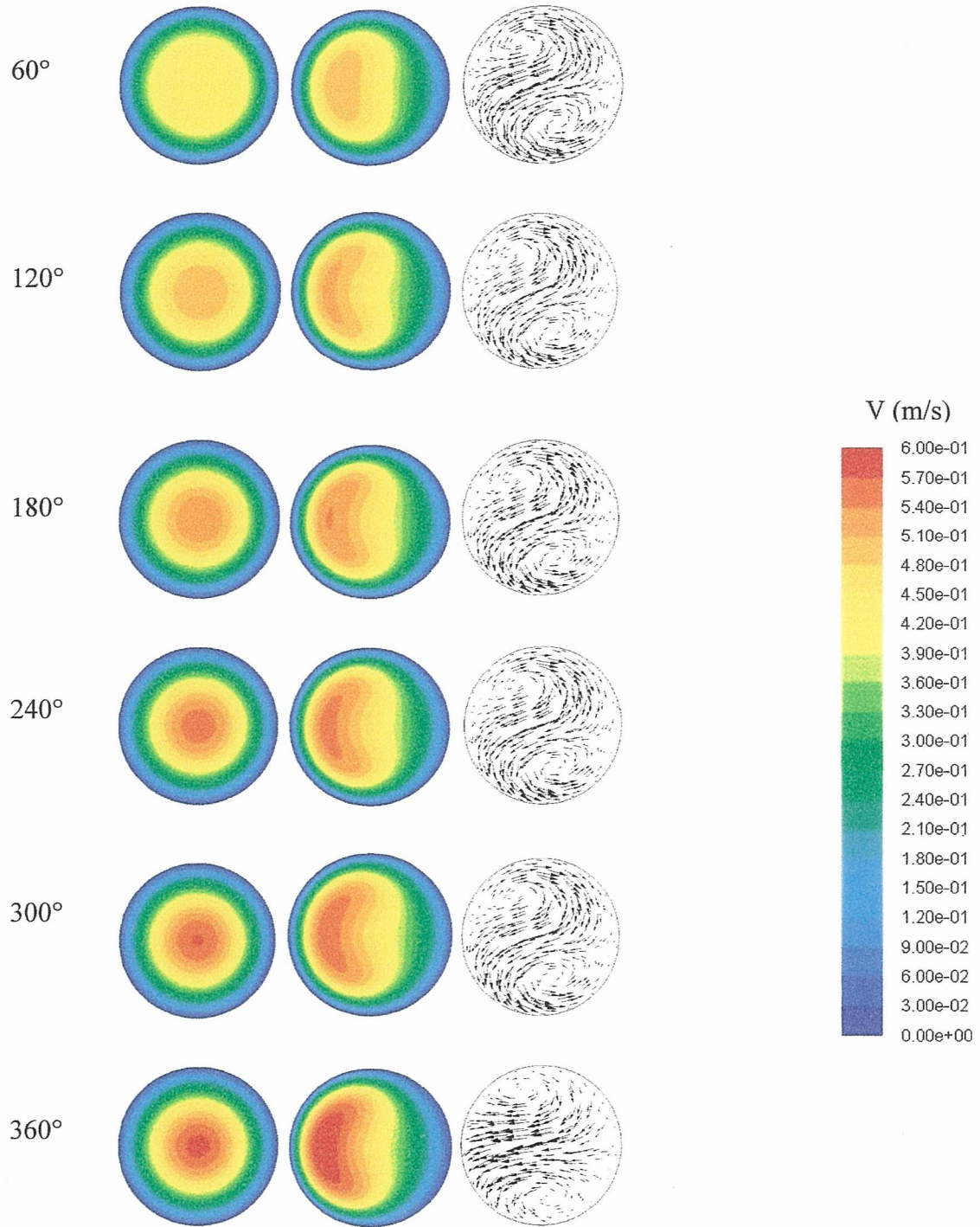


Figure 5.2: Developing Axial Velocity Profiles in a Circular Helical Channel ($Re = 492$, $De = 263.0$)

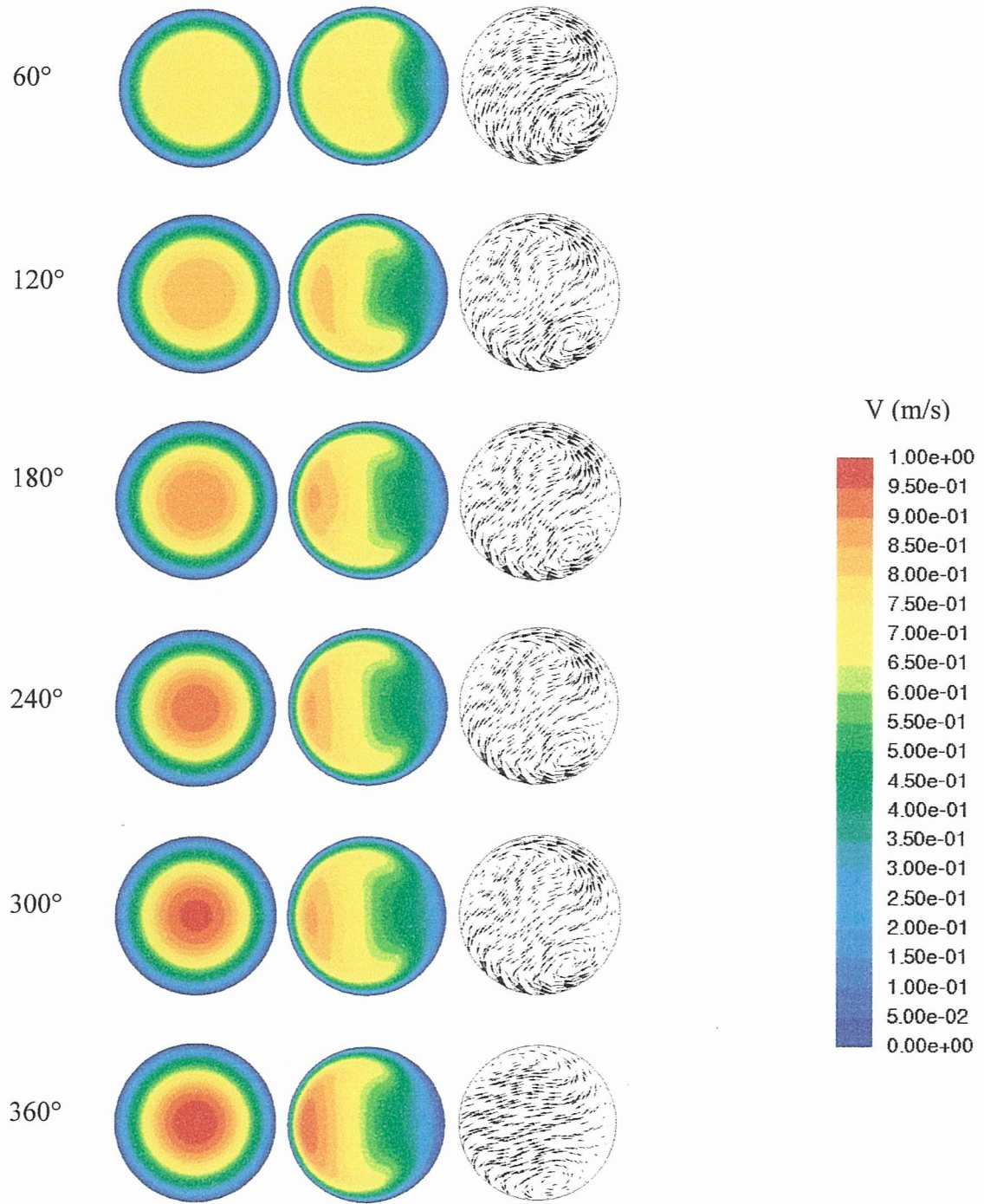


Figure 5.3: Developing Axial Velocity Profiles in a Circular Helical Channel ($Re = 900$, $De = 481.1$)

As expected, as the flow develops the location of the maximum axial velocity shifts towards the outer wall of the channel for each of the three helical cases. In the straight channel, the flow develops symmetrically about the center axis and the maximum axial velocity is located at the center of the channel. The axial velocity profile appears to be nearly symmetric about the horizontal mid-plane of the helical channels. As the Reynolds number increases, increasing the inlet velocity, the location of the maximum axial velocity shifts closer to the outer wall of the channel due to the increased centrifugal force acting on the fluid.

The velocity vectors show the development of Dean vortices within the flow. This secondary flow pushes the fluid flow from the inner wall through the middle of the channel to the outer wall, when the flow then splits and comes back along the top and bottom of the channel to the inner wall. The vortices are not symmetric about the horizontal axis of the channel as they are typically in a flat curved channel. The vortices are in the outer upper quadrant and the inner lower quadrant of the channel. This is most likely due to the helical shape of the channel and its downward pitch. The vortex in the outer upper quadrant appears larger than the second vortex, almost double the size. This could also be due to the downward pitch of the helix, causing the fluid to push down on the bottom of channel.

5.2 Heat Transfer in a Helical Circular Channel

To observe the effects on the heat transfer characteristics of a fluid through a helical channel, a constant surface temperature of 363 K was applied along the full length of the channel. The fluid entering the channel has a uniform temperature of 300 K. The same Reynolds numbers are used from the fluid flow models and a straight channel is

modeled for comparison. For the heat transfer models, the properties of air are temperature dependent because, as fluid is heated, the properties change. The temperature dependent properties were calculated from the air properties table of Cengel and Cimbala (2006). The data was plotted to create a best fit line. The equation from this line was entered as a polynomial in the FLUENT software in order to apply the appropriate properties for density, viscosity, and thermal conductivity.

Figure 5.4, Figure 5.6, and Figure 5.8 show the developing temperature profiles at 60° increments for both a straight circular channel, shown on the left, and a helical circular channel, shown on the right for each Reynolds number. The outer wall of the helical channel is to the left of the channel. Figure 5.5, Figure 5.7, and Figure 5.9 plot the mean temperature of the fluid as it flows through the each channel for each Reynolds number.

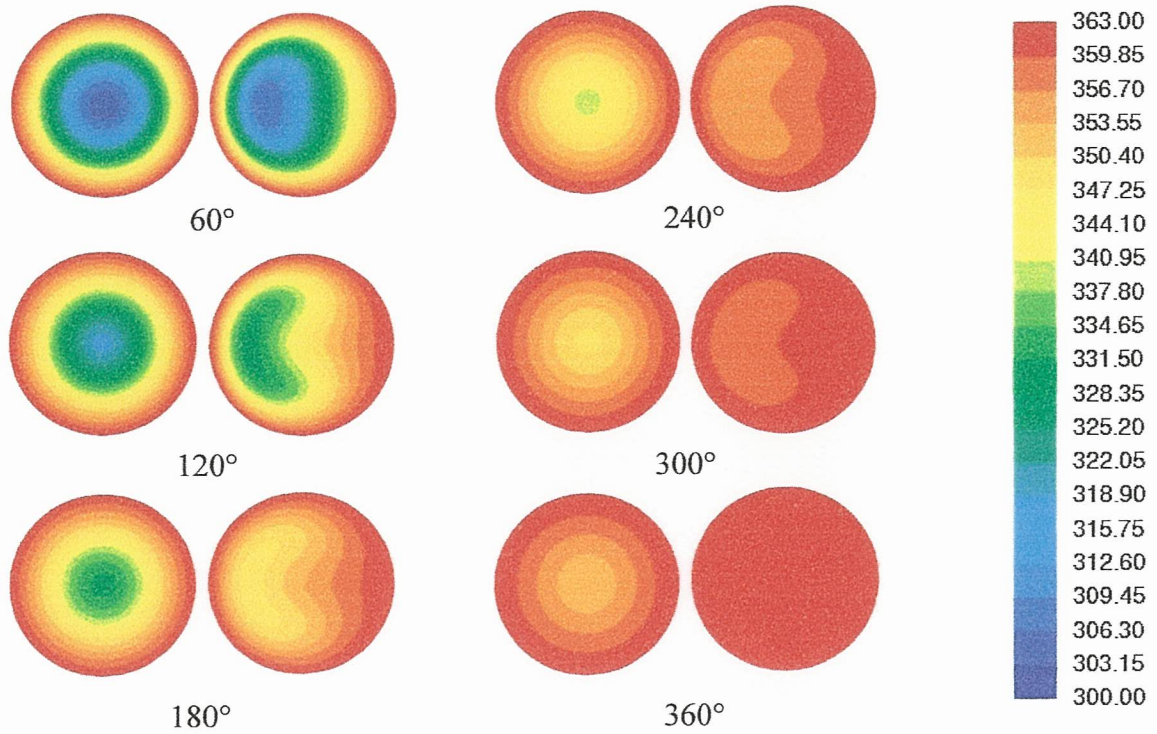


Figure 5.4: Developing Temperature Profiles in a Circular Helical Channel ($Re = 242$, $De = 263.0$)

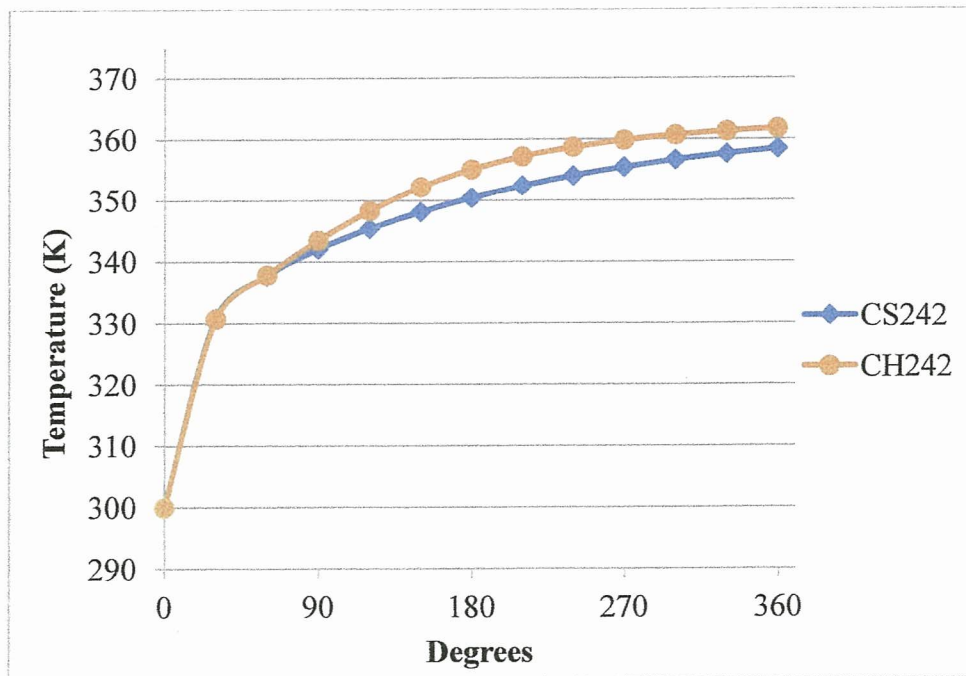


Figure 5.5: Mean Temperature in a Circular Helical Channel ($Re = 242$, $De = 129.4$)

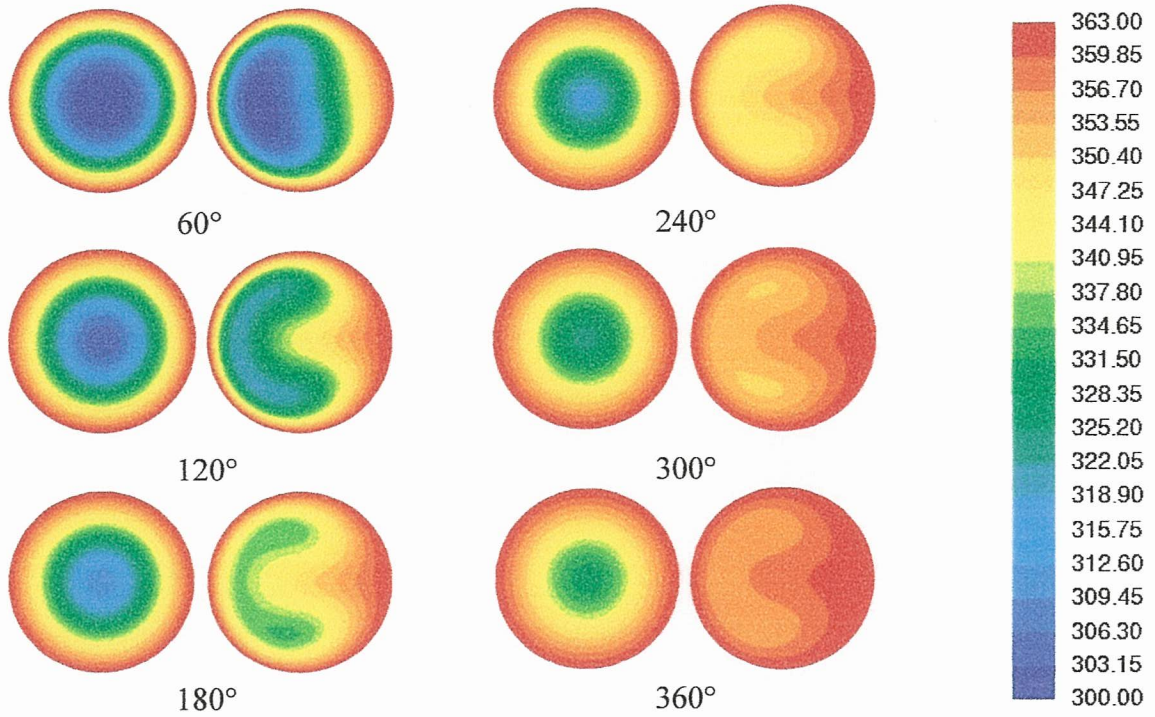


Figure 5.6: Developing Temperature Profiles in a Circular Helical Channel ($Re = 492$, $De = 263.0$)

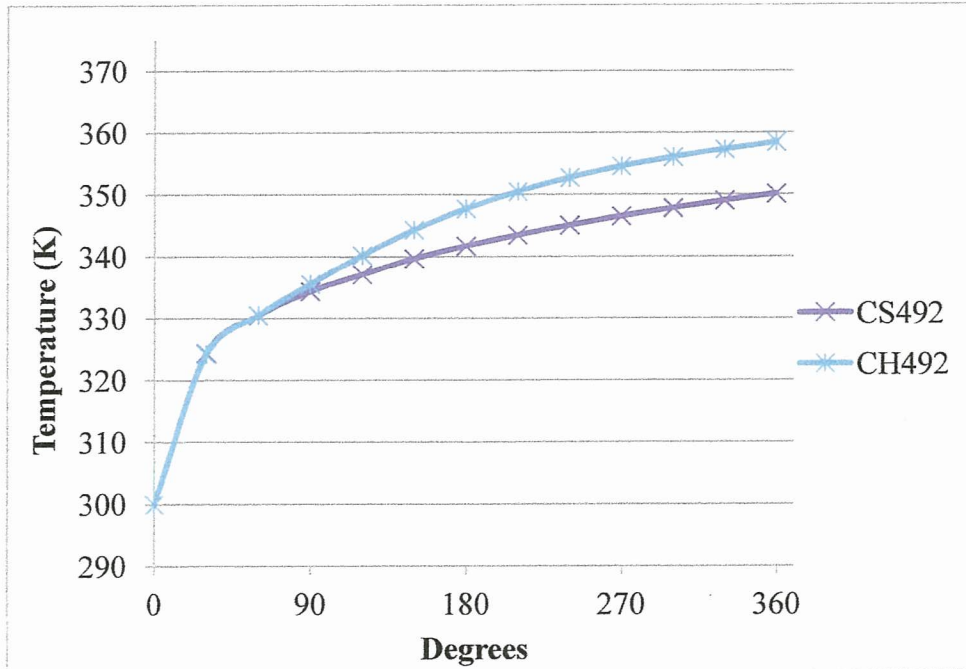


Figure 5.7: Mean Temperature in a Circular Helical Channel ($Re = 492$, $De = 263.0$)

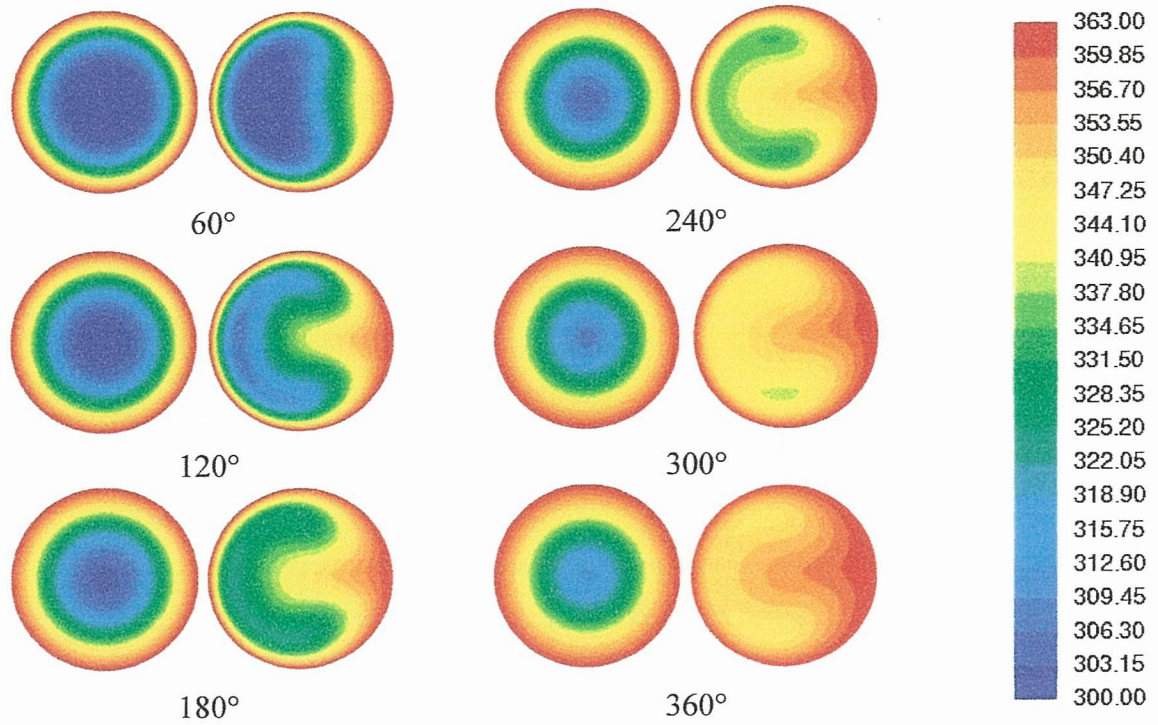


Figure 5.8: Developing Temperature Profiles in a Circular Helical Channel ($Re = 900$, $De = 481.1$)

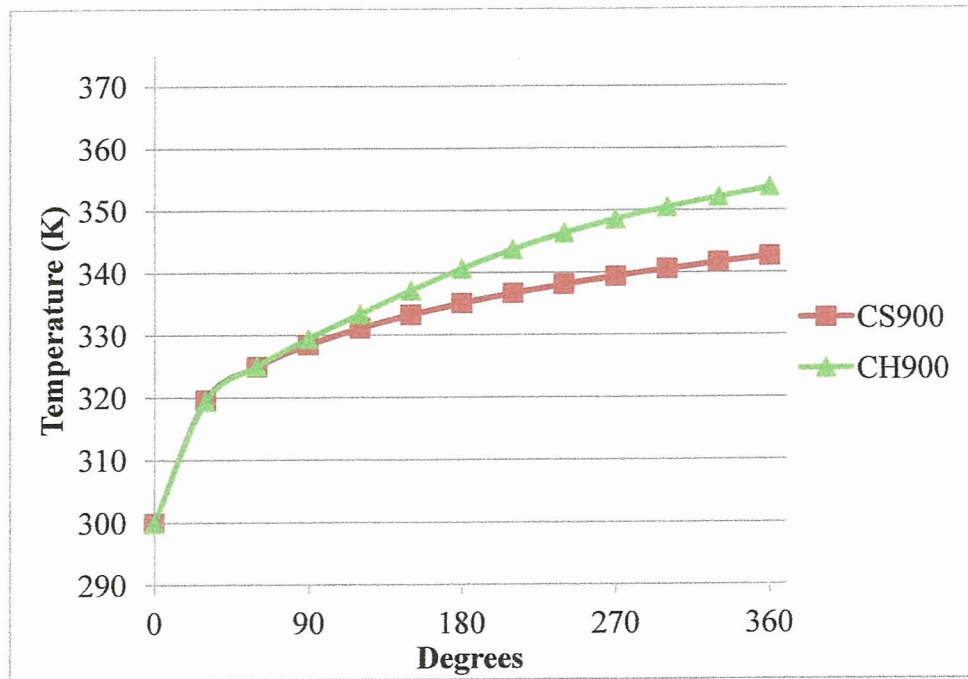


Figure 5.9: Mean Temperature in a Circular Helical Channel ($Re = 900$, $De = 481.1$)

Similar to the axial velocity profiles, the temperature profiles of the straight channel develop symmetrically about the center axis. The fluid in the straight channel is heated from the outside in; the coolest part of the fluid is in the center of the channel. The temperature profiles in the helical channel shift towards the outer wall, similar to the axial velocity profiles. The secondary flow aids in the heat transfer within the fluid as it pushes the cooler fluid, which would normally stay in the center of the straight channel, towards the outer wall, where it comes into contact with the heat source at the wall surface.

For all three Reynolds numbers, the helical model has a higher mean outlet temperature for the helical model. The temperature profile for the outlet of the helical channel for $Re = 242$ appears uniform and nearly equivalent to the surface temperature of 363 K. Figure 5.5 shows the temperature difference of the helical channel to be 61.76 K. The temperature difference between the outlet and inlet of the straight channel is approximately 58.48 K for $Re = 242$; this lower temperature difference is due to the cooler fluid in the center of the channel. The helical channel produces a 5.6% increase in the outlet-inlet temperature difference for $Re = 242$. The other two helical models have not reached a uniform temperature profile at the outlet, but do exhibit a higher mean temperature across the outlet cross section than the outlets for their respective straight circular channels. For $Re = 492$, the temperature difference from the outlet to the inlet of the straight channel is only 50.14 K, whereas for the helical channel, the temperature difference is 58.43 K, a difference of 16.5%. There is an even bigger temperature difference for $Re = 900$; the straight channel reaches only increases 42.66 K and the

helical channel increases 53.74 K from inlet to outlet, nearly a 12 degree difference between the two cases, which is an increase of 26.0%.

CHAPTER VI

ELLIPTICAL HELICAL CHANNEL

6.1 Elliptical Helix Model

Most of the research on curved and helical channels has been done for common cross sectional geometries such as a circle or rectangle. That data has been well documented, but much less is known about other cross-sectional geometries. For this thesis, an elliptical cross-section was considered to see if the Dean vortices can optimize the benefits of the secondary flow in the fluid. Two models were created with the same cross-sectional area as the circular model, one with the major axis along the horizontal axis and the other with the major axis along the vertical axis. The meshed cross sections are shown in Figure 6.1.

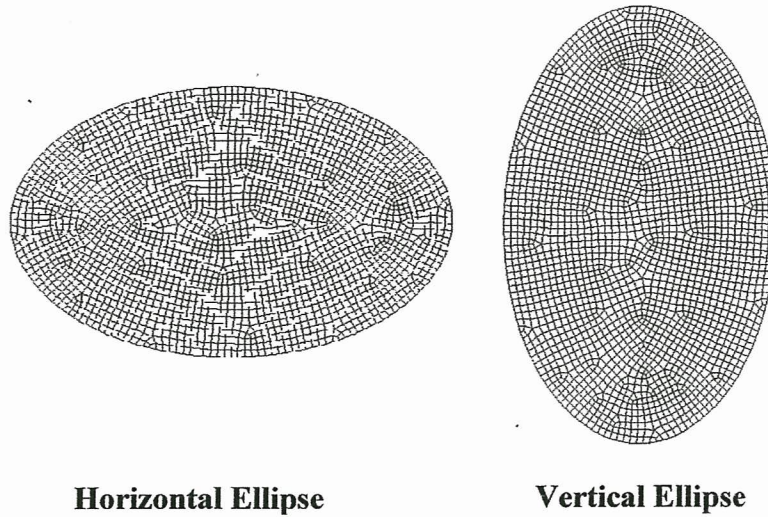


Figure 6.1: Elliptical Mesh Cross Sections

The selected length of the major axis is 16.1 mm and the corresponding length of the minor axis is 10 mm. These dimensions were chosen so that the elliptical cross sections would have the same area as the circular models. The same pitch of 30 mm and radius of curvature of 88.9 mm was used so that the data could be compared to that of the circular helix model. These models are shown in Figure 6.2. The inlet of the channel is shown in blue.

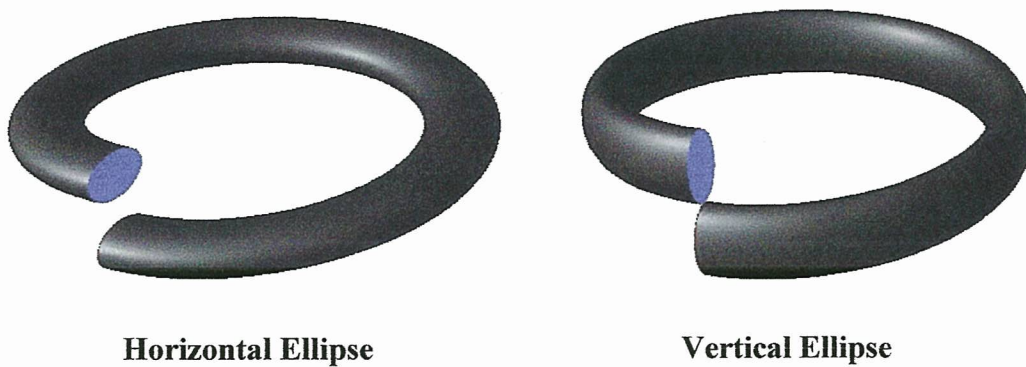


Figure 6.2: Elliptical Helical Channels

For comparison, straight elliptical channels with the same geometric cross section of equivalent length were created. The information for each model can be seen in Table 6.1 and Table 6.2.

Model	Horizontal Elliptical Helix Model			Horizontal Elliptical Straight Model		
Abbreviation	HH			HS		
Major Axis	16.1 mm			16.1 mm		
Minor Axis	10.0 mm			10.0 mm		
Curvature Radius	88.9 mm			N/A		
Curvature Ratio	1/7			N/A		
Pitch	30.0 mm			N/A		
Inlet Velocity	0.1468 m/s	0.2985 m/s	0.5461 m/s	0.1468 m/s	0.2985 m/s	0.5461 m/s
Reynolds Number	242	492	900	242	492	900
Dean Number	129.4	263	481.1	N/A	N/A	N/A
Inlet Temperature	300 K					
Surface Temperature	360 K					

Table 6.1: Horizontal Elliptical Channel Summary

Model	Vertical Elliptical Helix Model			Vertical Elliptical Straight Model		
Abbreviation	VH			VS		
Major Axis	16.1 mm			16.1 mm		
Minor Axis	10.0 mm			10.0 mm		
Curvature Radius	88.9 mm			N/A		
Curvature Ratio	1/7			N/A		
Pitch	30.0 mm			N/A		
Inlet Velocity	0.1468 m/s	0.2985 m/s	0.5461 m/s	0.1468 m/s	0.2985 m/s	0.5461 m/s
Reynolds Number	242	492	900	242	492	900
Dean Number	129.4	263	481.1	N/A	N/A	N/A
Inlet Temperature	300 K					
Surface Temperature	360 K					

Table 6.2: Vertical Elliptical Channel Summary

6.2 Fluid Flow in a Helical Elliptical Channel

To observe the developing fluid flow through the elliptical channels, the same Reynolds numbers as the circular helix model were used: $Re = 242, 492, \text{ and } 900$. Using the same Reynolds numbers will allow for easy comparison to the circular models. The developing axial velocity profiles for both the straight and helical channel for the horizontal helical model are shown for 60° increments in Figure 6.3, Figure 6.4, and Figure 6.5. The axial velocity vectors for the corresponding cross section of the horizontal elliptical helical model are shown as well.

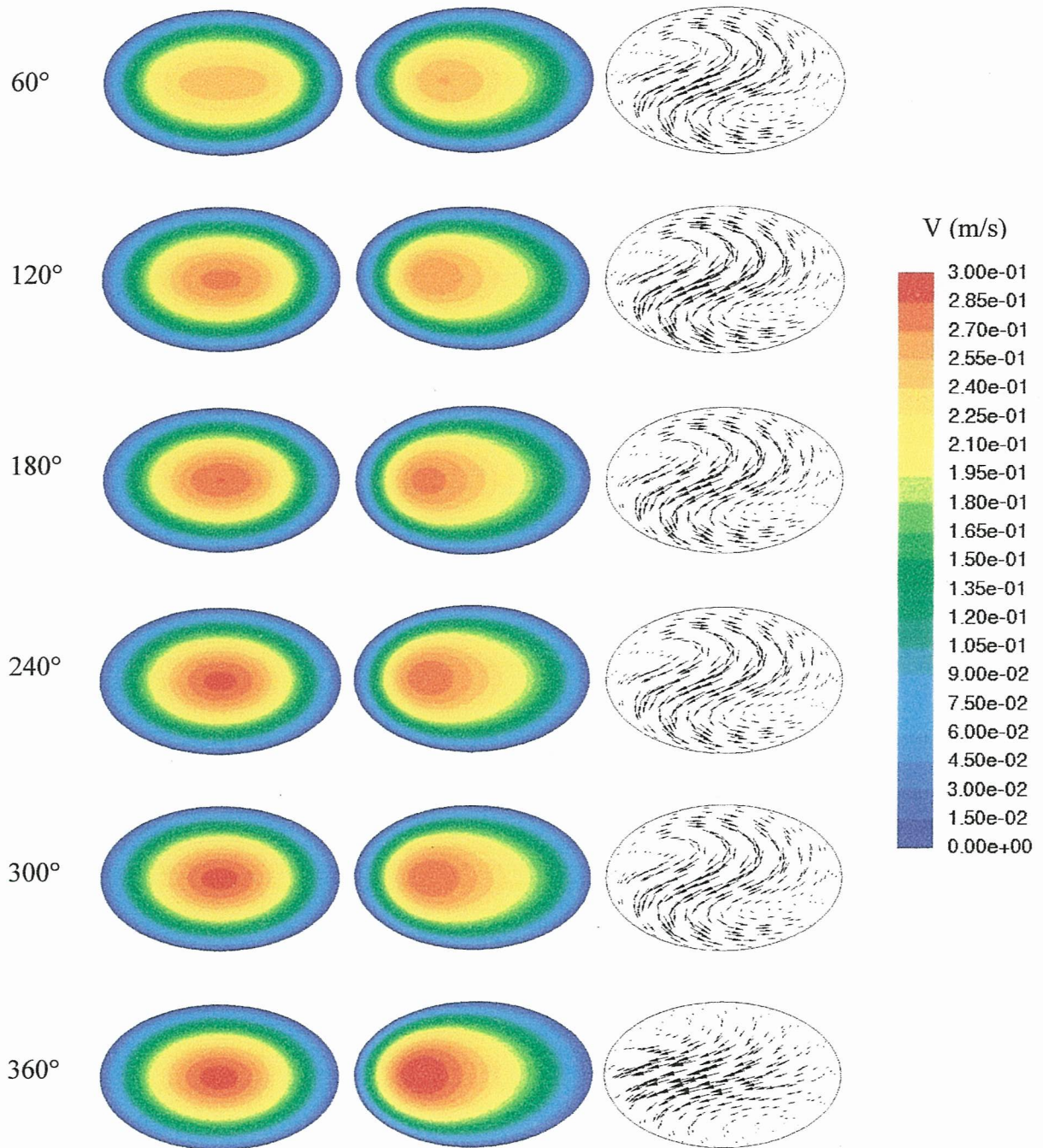


Figure 6.3: Developing Axial Velocity Profiles in a Horizontal Elliptical Helical Channel ($Re = 242$, $De = 129.4$)

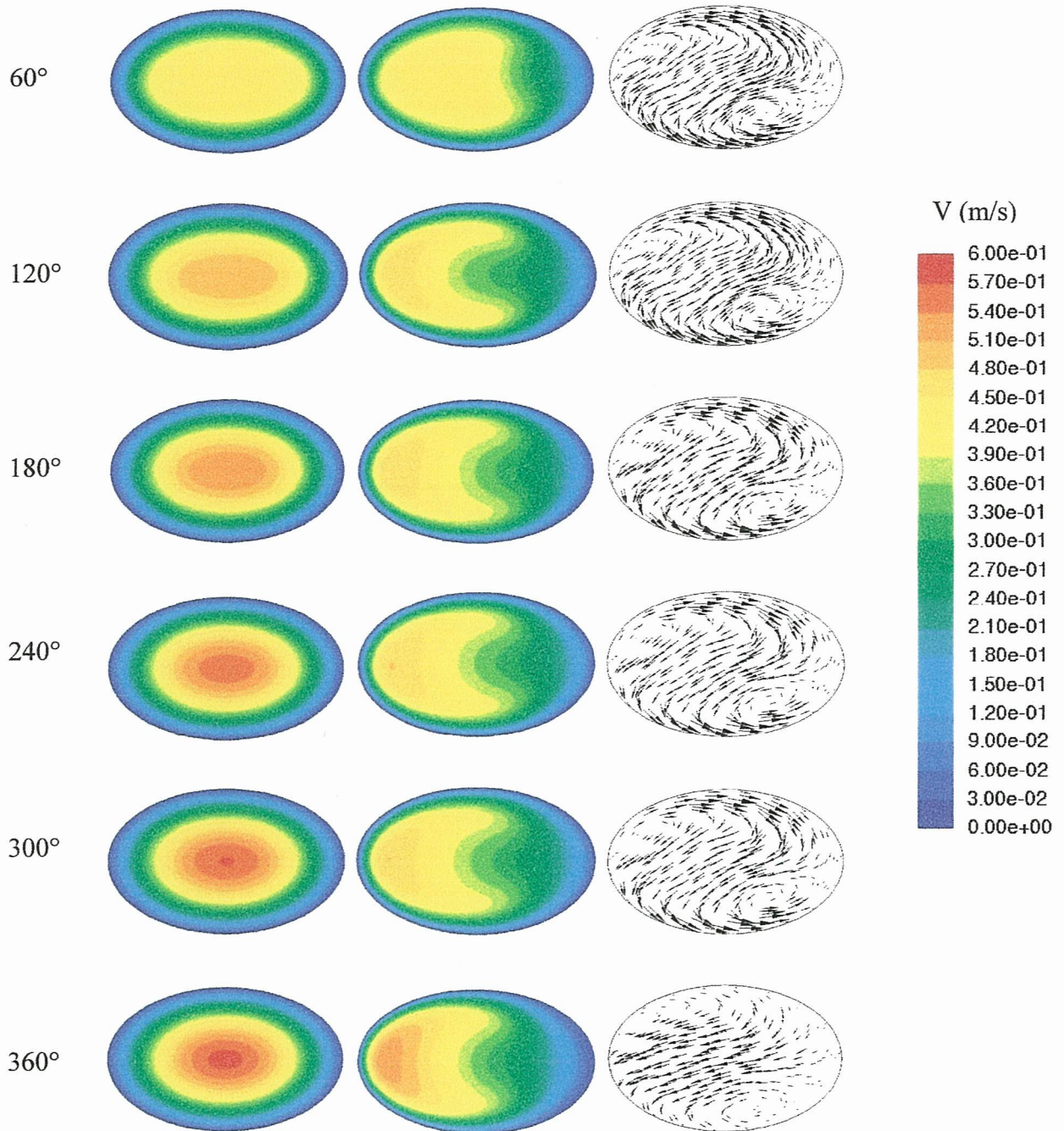


Figure 6.4: Developing Axial Velocity Profiles in a Horizontal Elliptical Helical Channel ($Re = 492$, $De = 263.0$)

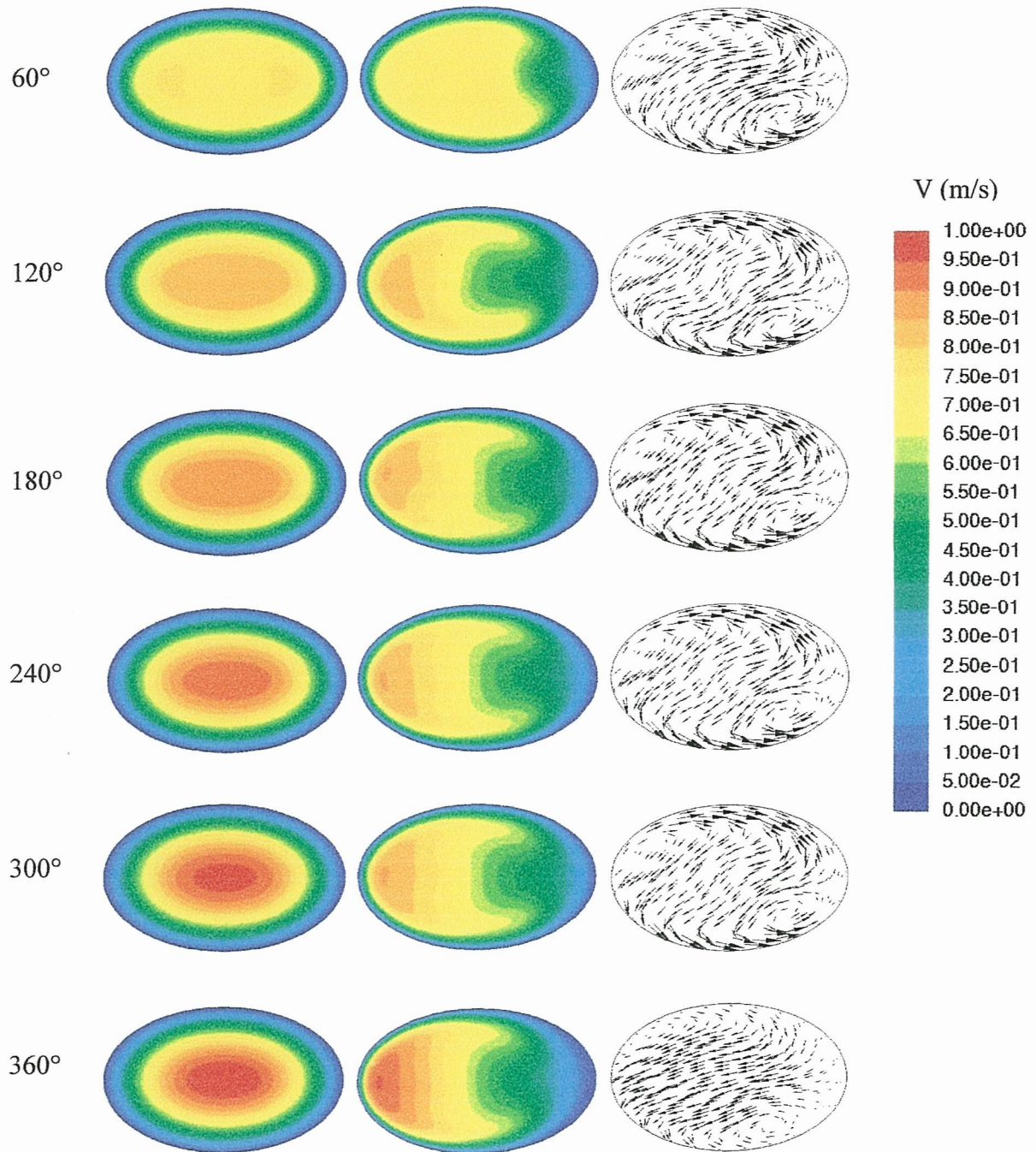


Figure 6.5: Developing Axial Velocity Profiles in a Horizontal Elliptical Helical Channel ($Re = 900$, $De = 481.1$)

The results are similar to those for the circular helical model. The straight model has the location of the maximum axial velocity along the center axis of the channel and the profile is symmetric about the horizontal and vertical axes. In the helical model, the location of the maximum axial velocity shifts towards the outer wall as the flow develops. As the Reynolds number increases, the location of the maximum axial velocity shifts closer to the outer wall of the channel of the helical model. It does not appear that the velocity has fully developed at the end of the helical models as it did in the circular models.

Again, the development of two Dean vortices can be seen. The vortices appear closer to the horizontal axis than the circular helical model, but still in the same relative location in the outer upper quadrant and inner lower quadrant. The upper vortex again appears to be larger than the lower vortex.

The axial velocity profiles for the vertical elliptical helical model are shown in Figure 6.6, Figure 6.7, and Figure 6.8. Again, a straight channel with the same vertical ellipse cross section is modeled for comparison. The axial velocity vectors for the helical model are also shown.

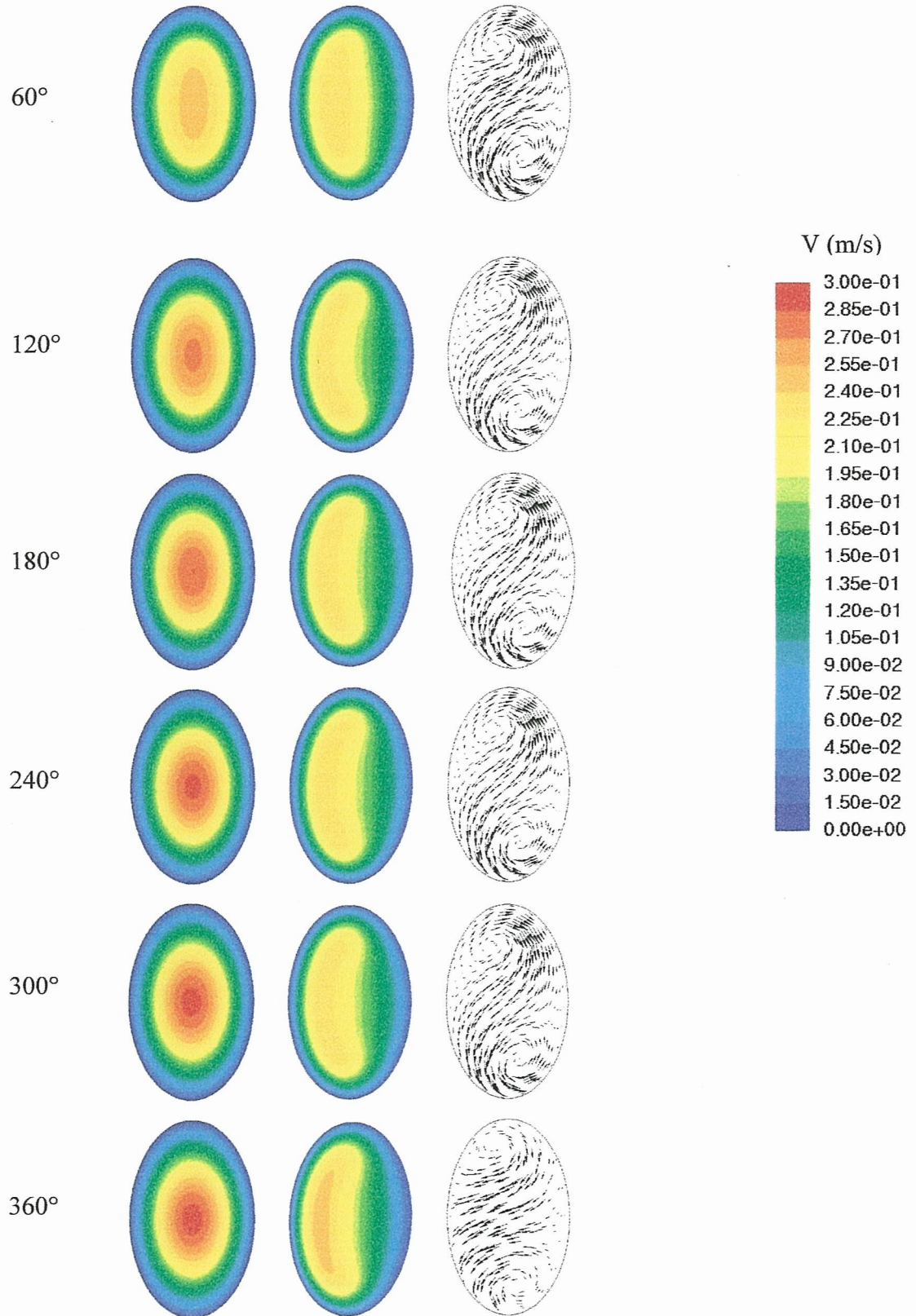


Figure 6.6: Developing Axial Velocity Profiles in a Vertical Elliptical Helical Channel ($Re = 242$, $De = 129.4$)

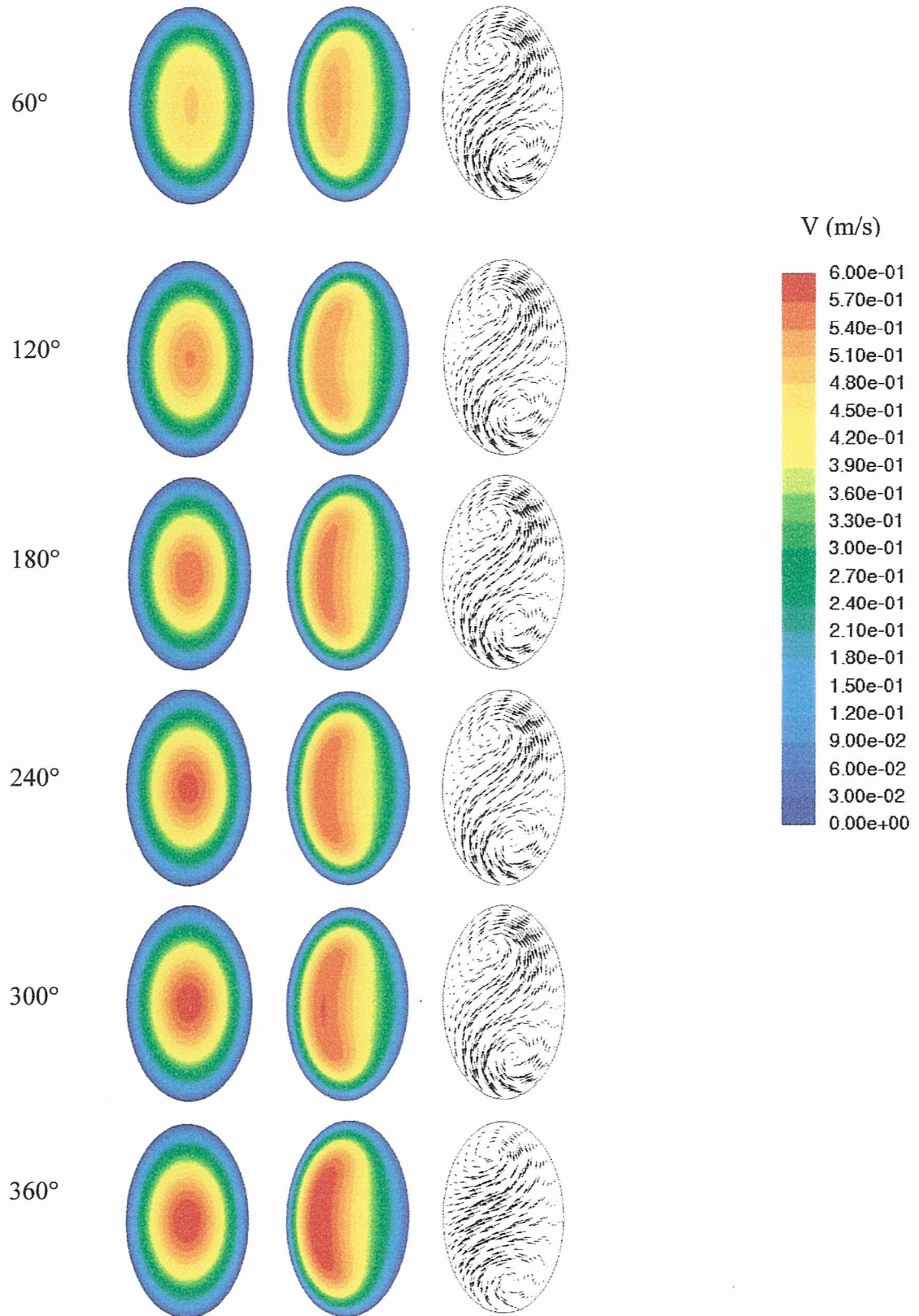


Figure 6.7: Developing Axial Velocity Profiles in a Vertical Elliptical Helical Channel ($Re = 492$, $De = 263.0$)

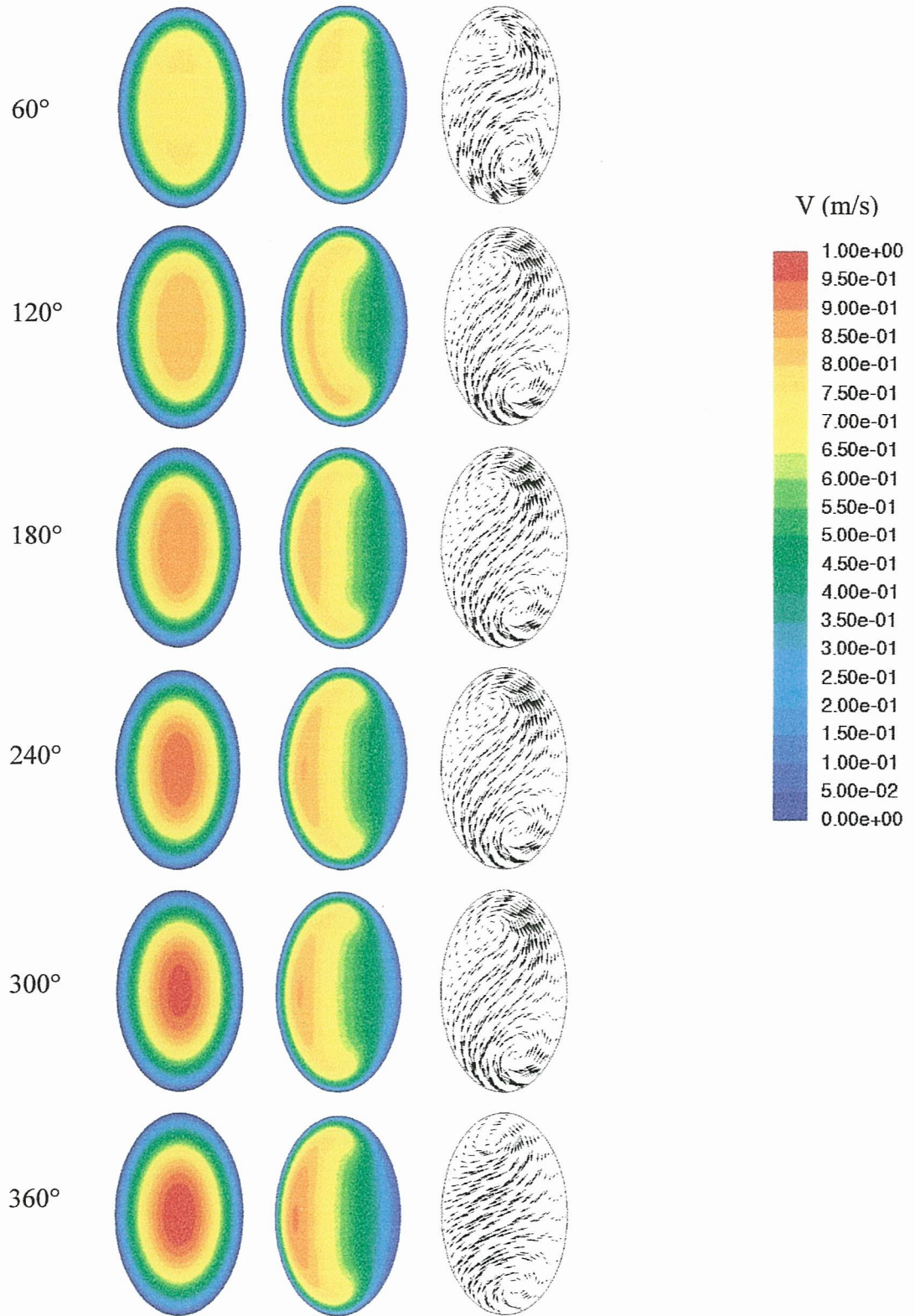


Figure 6.8: Developing Axial Velocity Profiles in a Vertical Elliptical Helical Channel ($Re = 900$, $De = 481.1$)

The data for the vertical elliptical channel are similar to the previous helical cases. The location of the maximum axial velocity does shift towards the outer wall of the channel, although it is less obvious because of the long thin cross section due to the geometry, and as the Reynolds number increases, the location of the maximum velocity becomes closer to the outer wall of the channel.

Two vortices develop in each case, with their centers pushed towards the upper and lower walls of the channel. The vortices tend to shift toward the outer upper quadrant and lower inner quadrant of the channel. For the vertical ellipse, the vortices appear to be relatively the same size in comparison to the other cases.

6.3 Heat Transfer in a Helical Elliptical Channel

To see how the Dean vortices observed in the fluid flow results affect the heat transfer capabilities of the fluid in the helical elliptical channels, a constant surface temperature is applied to the wall of the channel. The air enters the channel with a uniform temperature of 300 K and at a constant surface temperature of 363 K applied along the entire length of the channel. The same temperature dependent air properties are used from the circular models.

The developing temperature profiles for the horizontal elliptical channels are shown in Figure 6.9, Figure 6.11, and Figure 6.13. The same conditions are applied to the straight channel for comparison purposes. The outer wall of the helical channel is shown to the left of the channel.

Figure 6.10, Figure 6.12, and Figure 6.14 show the mean temperature of the developing temperature profile of the fluid.

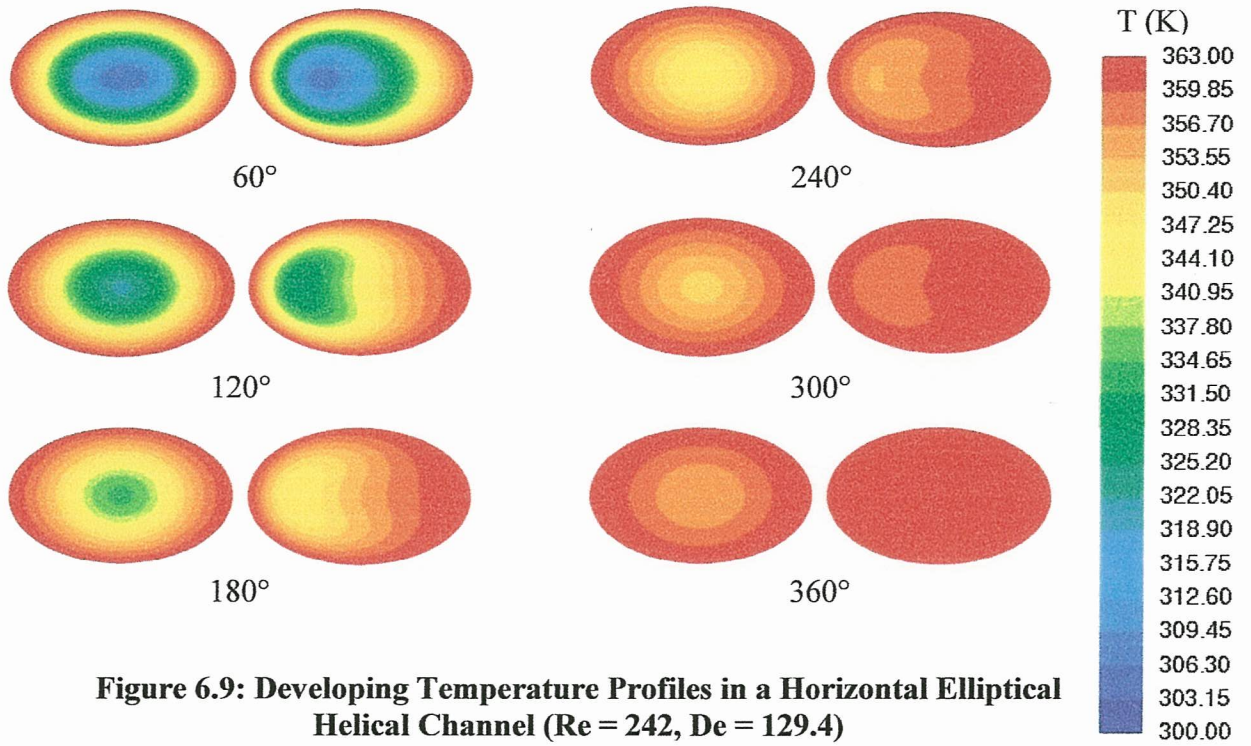


Figure 6.9: Developing Temperature Profiles in a Horizontal Elliptical Helical Channel ($Re = 242$, $De = 129.4$)

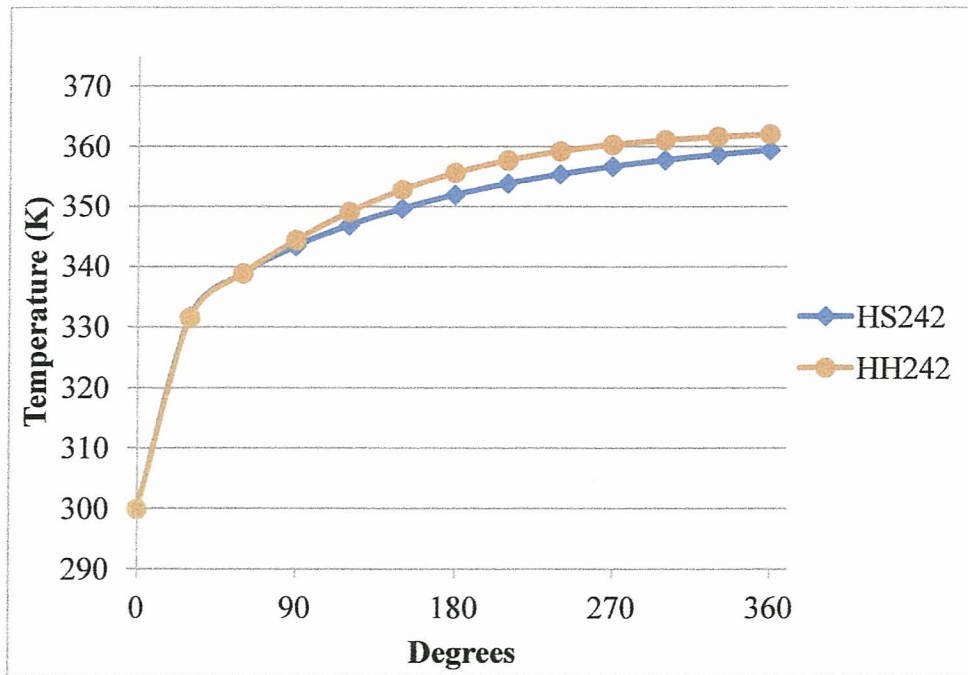


Figure 6.10: Mean Temperature in a Horizontal Elliptical Helical Channel ($Re = 242$, $De = 129.4$)

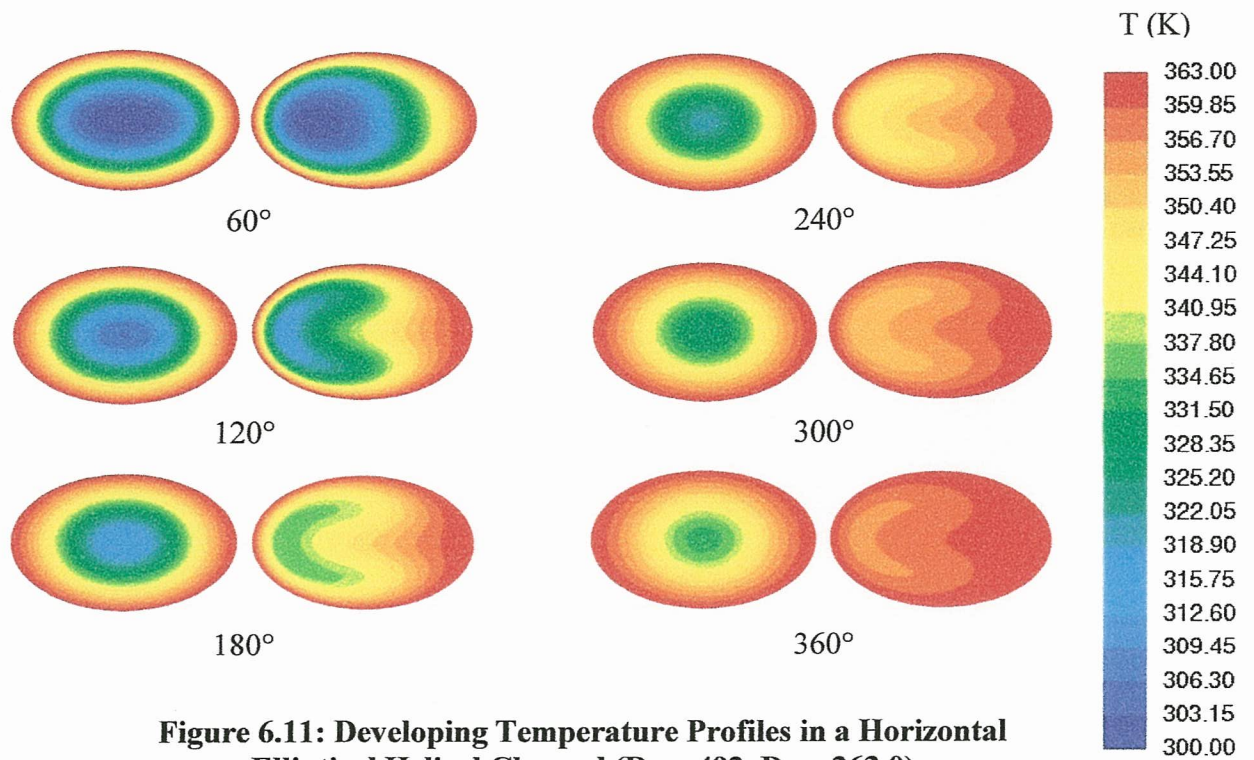


Figure 6.11: Developing Temperature Profiles in a Horizontal Elliptical Helical Channel ($Re = 492$, $De = 263.0$)

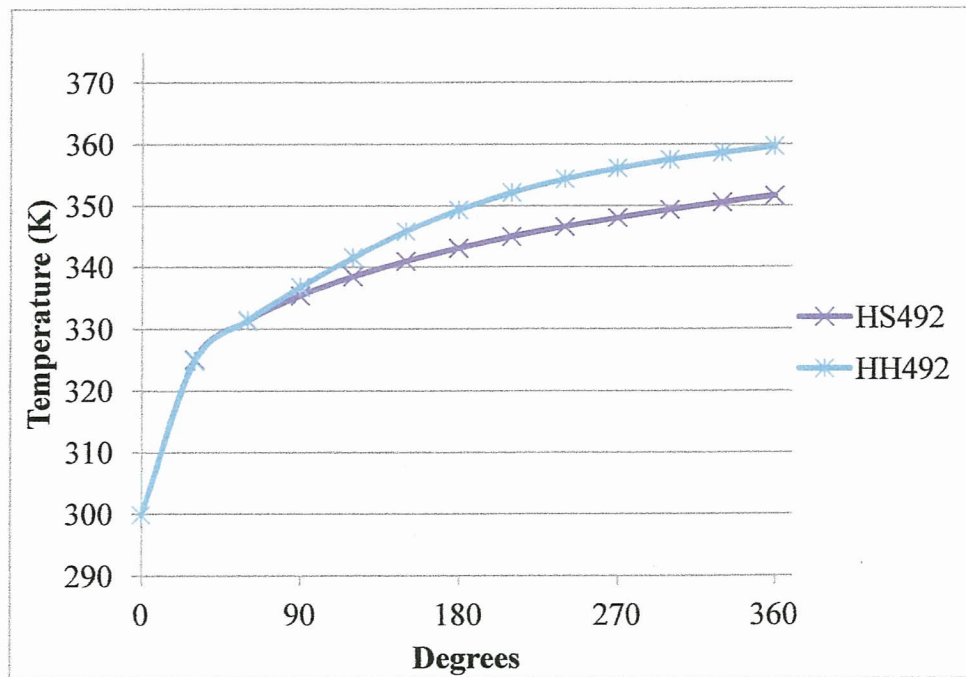


Figure 6.12: Mean Temperature in a Horizontal Elliptical Helical Channel ($Re = 492$, $De = 263.0$)

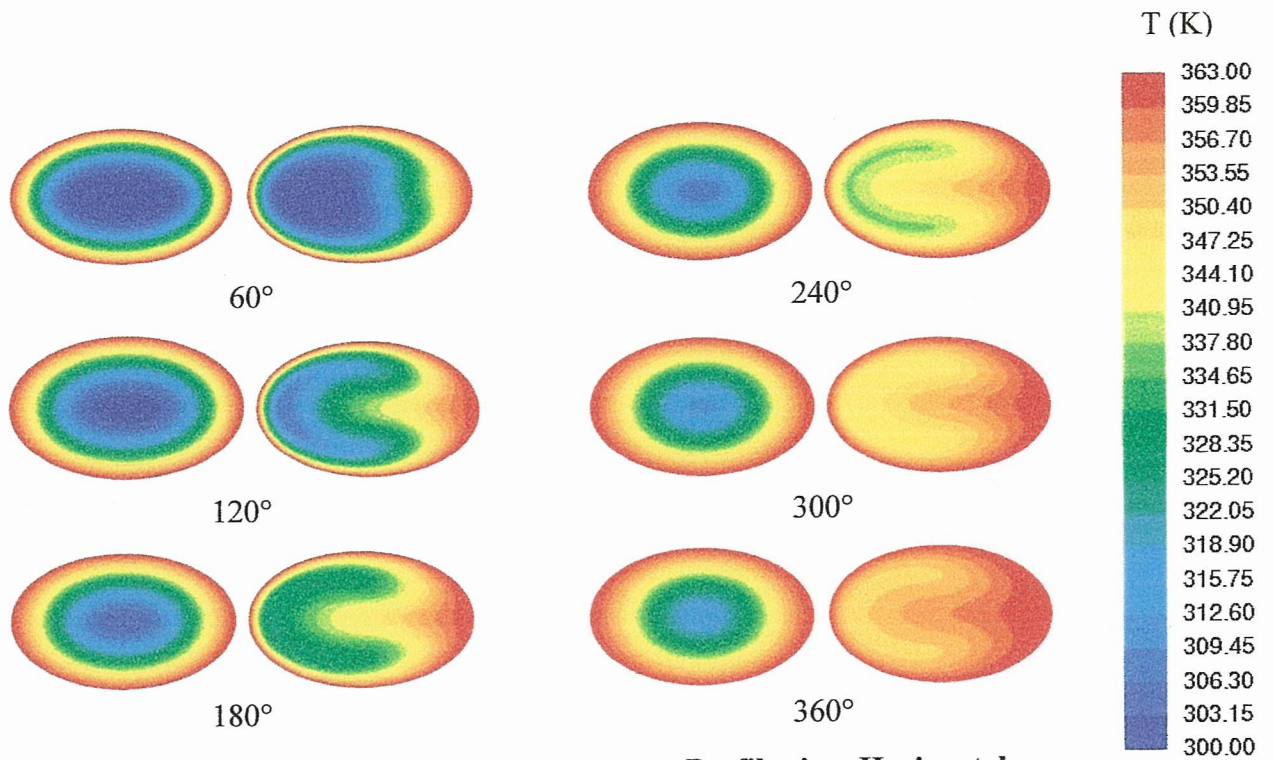


Figure 6.13: Developing Temperature Profiles in a Horizontal Elliptical Helical Channel ($Re = 900$, $De = 481.1$)

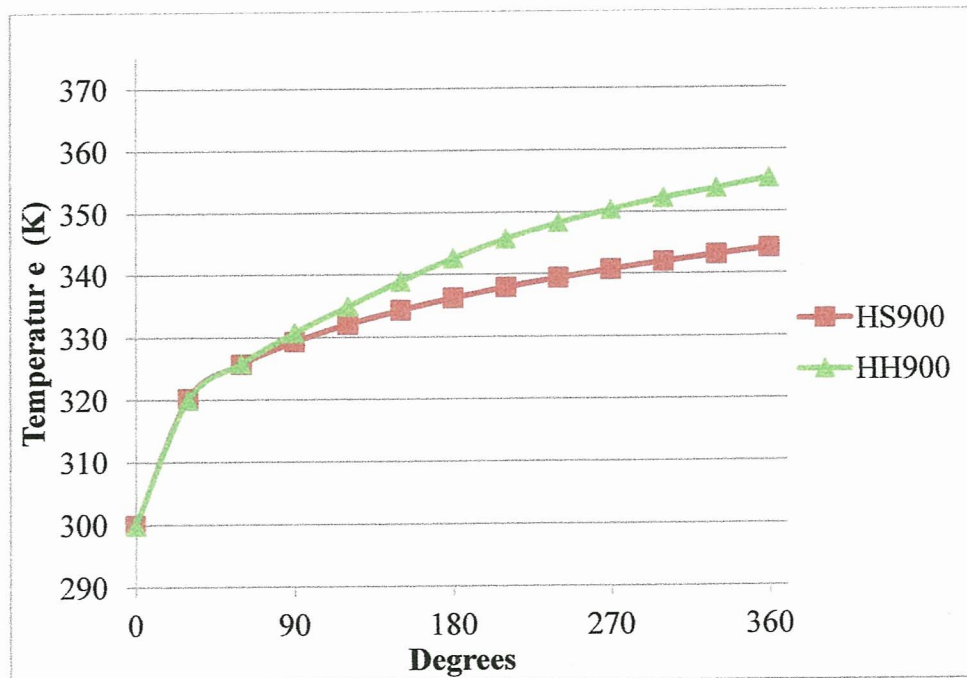


Figure 6.14: Mean Temperature in a Horizontal Elliptical Helical Channel ($Re = 900$, $De = 481.1$)

As seen in the circular heat transfer models, the temperature profiles develop similarly to the axial velocity profiles. The temperature profiles of the straight model center around the axis of the channel, where the coolest part of the fluid is in the middle. The helical model forces the cooler fluid towards the outer wall allowing it to come in contact with the heat source.

By the end of the helical channel for $Re = 242$, the fluid has a uniform temperature almost equivalent to the wall surface temperature at 362 K; this was also the case for the circular helical model for the same Reynolds number. With an outlet-inlet temperature difference of 62.08 K, this is an increase of 4.4% over the straight model which only rises 59.45 K from inlet to outlet for $Re = 242$. The models for $Re = 492$ and $Re = 900$ do not reach a uniform temperature at the outlet of the helical channel, but do reach higher mean temperatures than their straight model counterparts. There is a larger gap between the outlet temperatures for $Re = 492$; the straight model rises 51.67 K and the helical model rises 59.68 K, an increase of 15.5%. The largest temperature difference is seen for $Re = 900$ with a difference of 11 degrees or 25.7% between the two models; the straight model has a temperature difference of 44.08 K and the helical model has a temperature difference of 55.40 K. These results are very similar to the circular helical models.

The developing temperature profiles for the vertical elliptical channels are shown in Figure 6.15, Figure 6.17, and Figure 6.19. The outer wall of the helical channel is shown to the left of the channel. Figure 6.16, Figure 6.18, and Figure 6.20 show the mean temperature of the fluid along the channel as the flow develops.

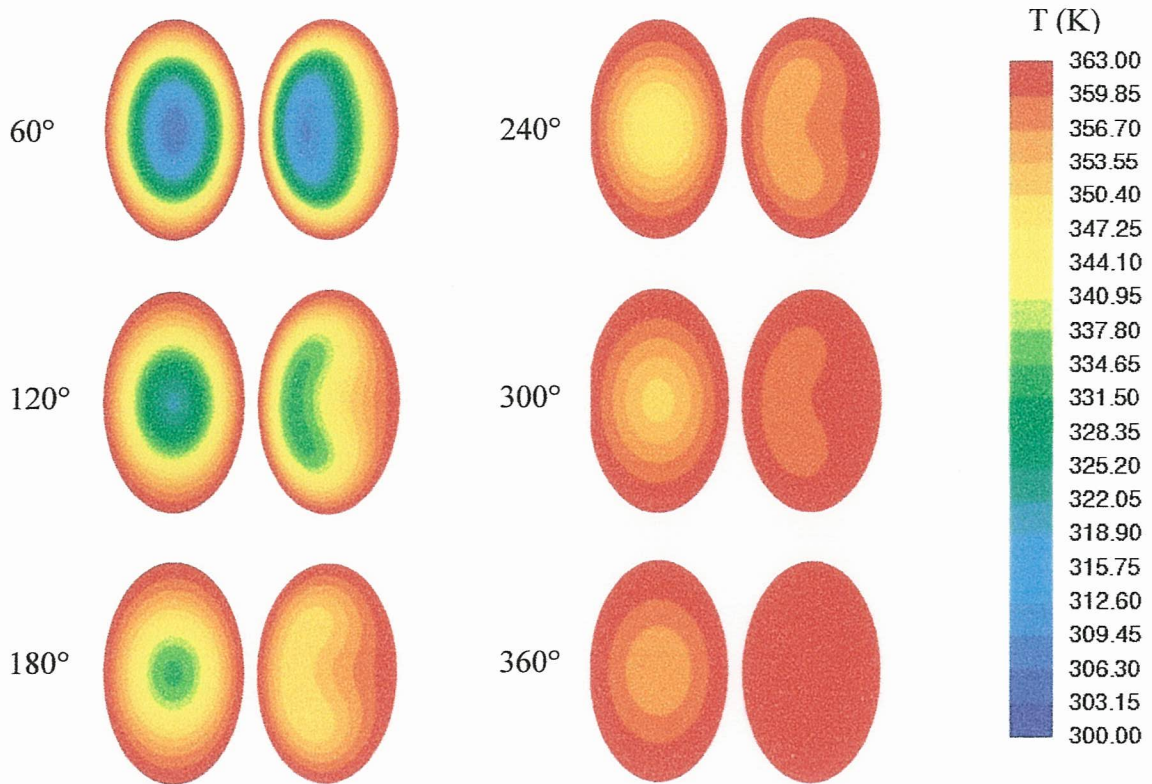


Figure 6.15: Developing Temperature Profiles in a Vertical Elliptical Helical Channel ($Re = 242$, $De = 129.4$)

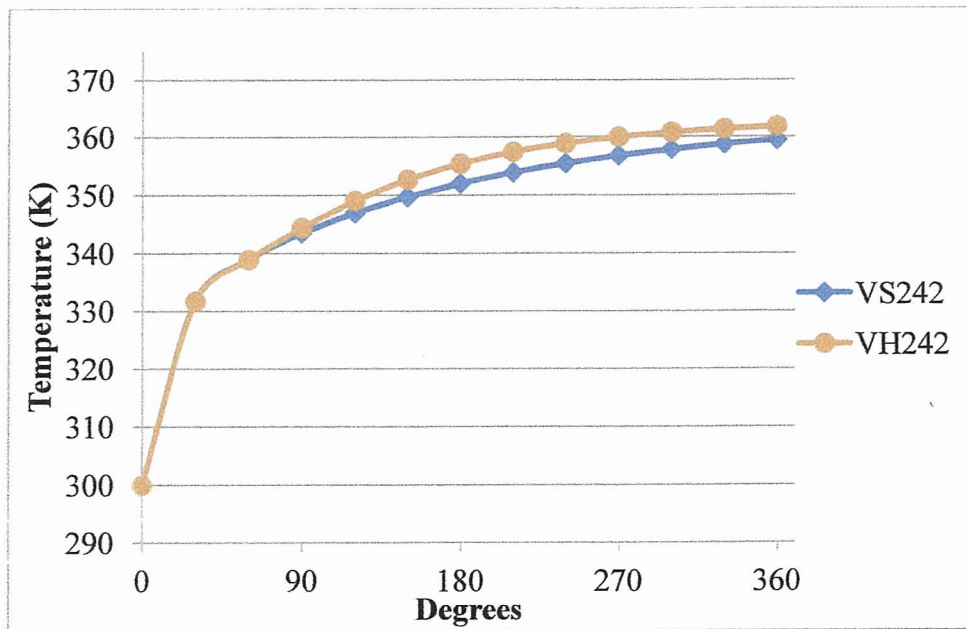


Figure 6.16: Mean Temperature in a Vertical Elliptical Helical Channel ($Re = 242$, $De = 129.4$)

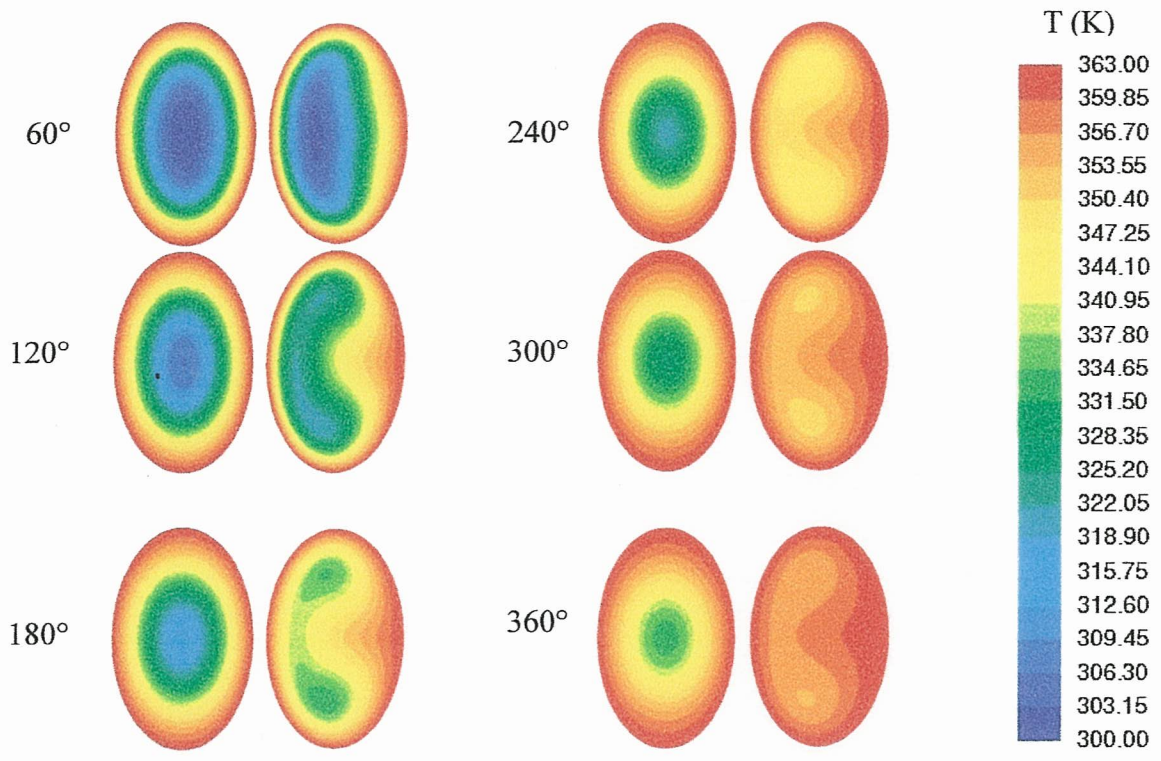


Figure 6.17: Developing Temperature Profiles in a Vertical Elliptical Helical Channel ($Re = 492$, $De = 263.0$)

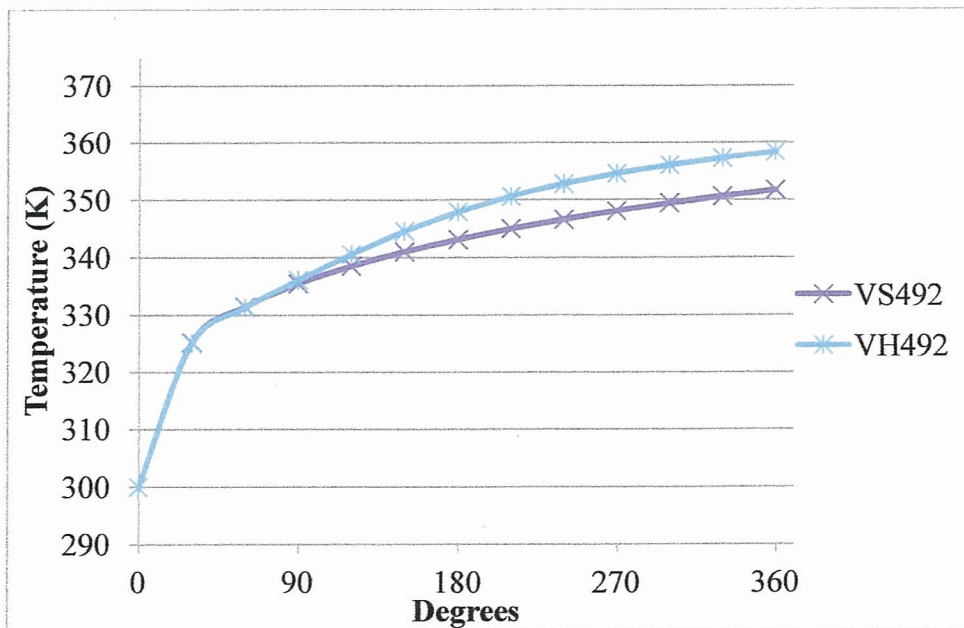


Figure 6.18: Mean Temperature in a Vertical Elliptical Helical Channel ($Re = 492$, $De = 263.0$)

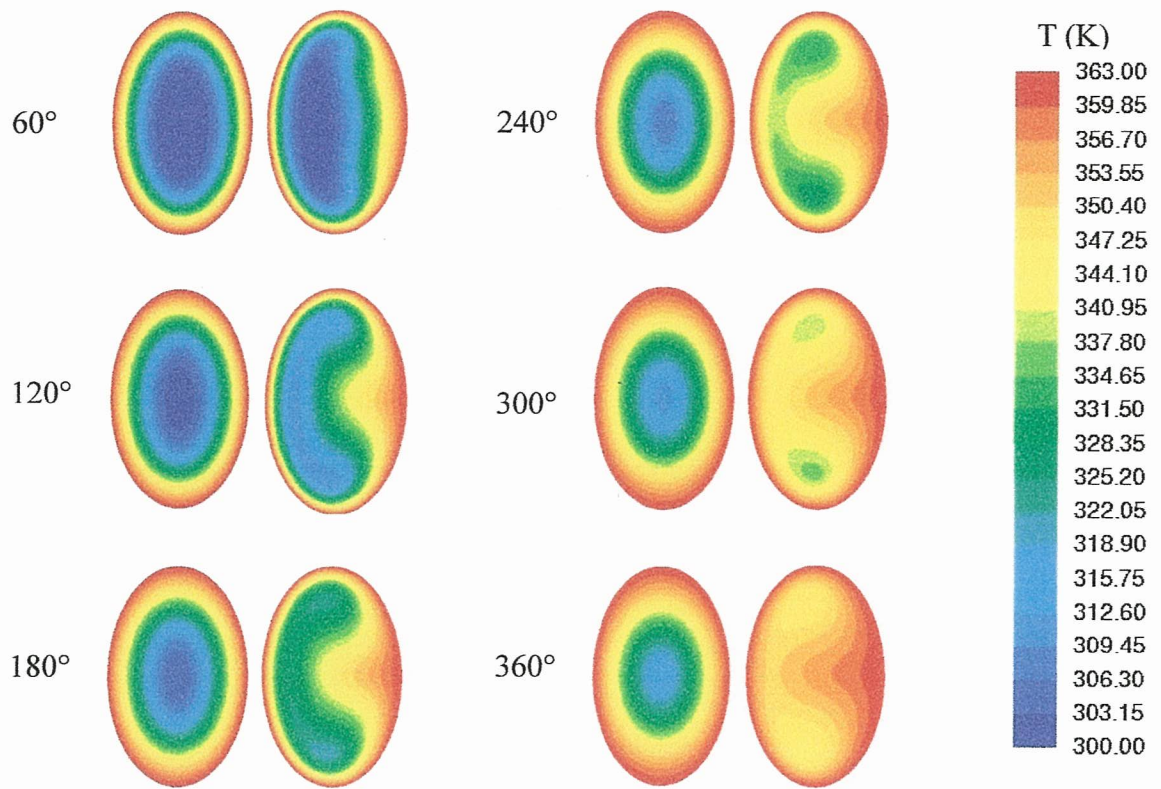


Figure 6.19: Developing Temperature Profiles in Vertical Elliptical Helical Channel ($Re = 900$, $De = 481.1$)

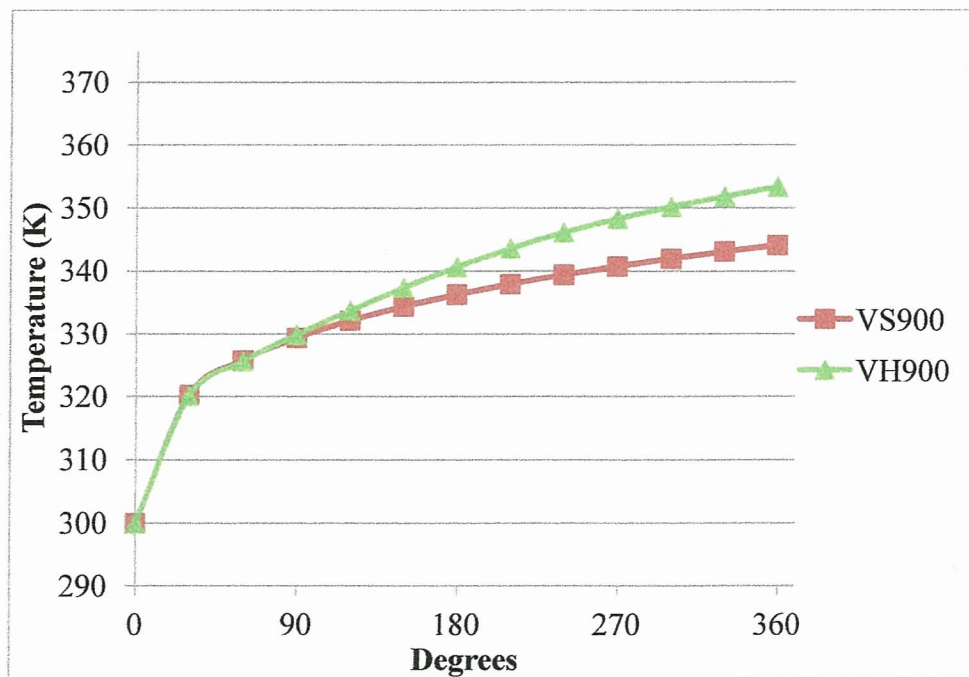


Figure 6.20: Mean Temperature in a Vertical Elliptical Helical Channel ($Re = 900$, $De = 481.1$)

Similar to the previous models, the temperature profiles develop like the velocity profiles for the channel. The straight channel profiles center around the axis of the channel as the vertical elliptical helix model shifts the cooler fluid towards the outer wall of the channel and into contact with the heat source.

For $Re = 242$ for the helical model, the fluid reached a uniform temperature of nearly 362 K at the outlet of the channel. This was also the case for both the circular helix and horizontal elliptical helix models for $Re = 242$. The straight channel for $Re = 242$ only has a temperature difference of 59.45, the same as the horizontal elliptical straight model, which is again a 3.9% increase. For $Re = 492$ and $Re = 900$, the mean outlet temperature is the same as the horizontal elliptical model (351.67 K and 344.08 K, respectively). This is to be expected as the two straight channels have the same amount of surface area exposed to the heat source. The mean outlet temperatures for the $Re = 492$ and $Re = 900$ differ slightly from the horizontal elliptical helical models. The vertical horizontal elliptical models has an outlet-inlet temperature difference of 58.32 K for $Re = 492$ and 53.29 K for $Re = 900$. This produces an increase in mean outlet temperature of 12.9% for $Re = 492$ and 20.9% for $Re = 900$.

6.4 Results Comparison

There are obvious differences between the straight and helical models for each cross sectional geometry. This section will look at a comparison of the all the results. The reason for elliptical cross section models was to evaluate how the development of Dean vortices affects the heat transfer capabilities of the fluid. For comparison, the mean outlet temperature for all of the models is plotted for each Reynolds number. Figure 6.21 shows the results for $Re = 242$.

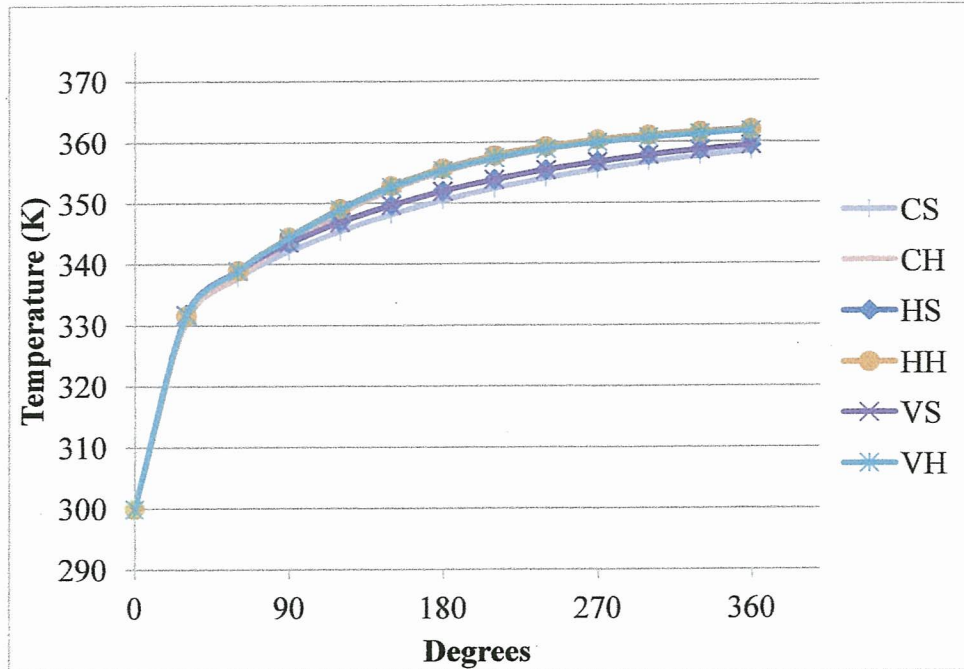


Figure 6.21: Mean Temperature Comparison for $Re = 242$, $De = 129.4$

The mean temperature develops in a similar fashion for all cases at $Re = 242$. All of the helical models reach a mean outlet temperature of almost 362 K, only one degree lower than the applied wall surface temperature. The temperature difference for the straight channels is slightly lower, with a temperature of 59.45 K for both elliptical models; the circular model is one degree lower at 58.48 K from inlet to outlet. To compare the heat transfer capabilities of the fluid at $Re = 242$, the Nusselt number (Nu) is plotted for the developing flow in Figure 6.22.

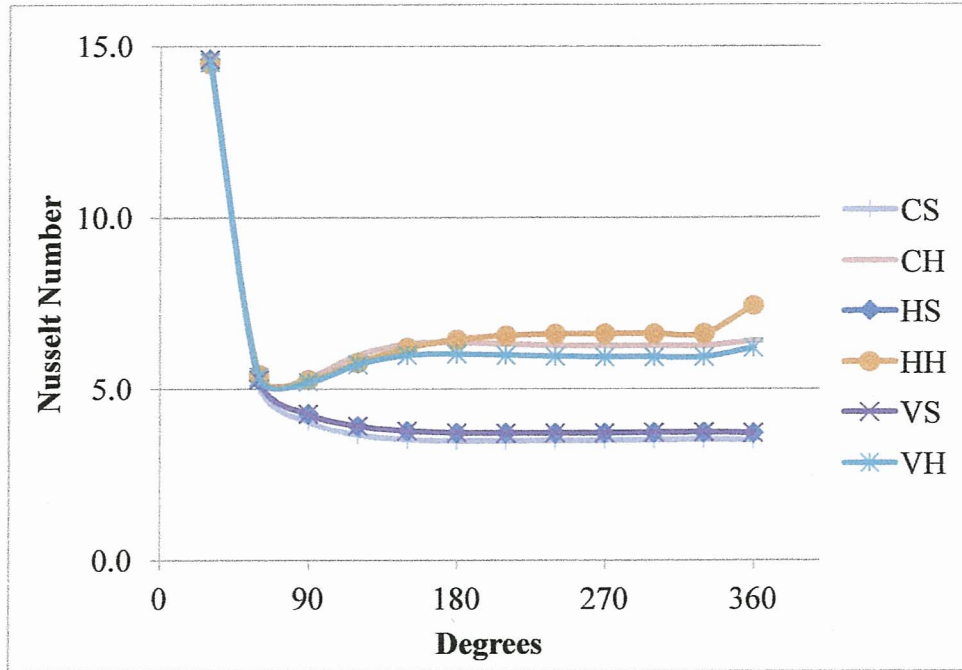


Figure 6.22: Nusselt Number Comparison for $Re = 242$, $De = 129.4$

There is a big change in Nusselt number at the beginning of the channel, but as the flow develops, the Nusselt number approaches an asymptote as the flow becomes fully developed for each case. For the helical cases, the Nusselt number jumps slightly at the outlet, this is most likely due to a numerical issue with the pressure outlet definition at the outlet plane of the channel. For a straight circular channel with fully developed laminar flow with an applied uniform surface temperature, $Nu = 3.66$. For all three straight channels, the Nusselt number approaches an asymptote close to this value. The helical cases approach a higher Nusselt number between 6.0 and 7.0, the horizontal elliptical helical model exhibits the highest Nusselt number of all the cases for $Re = 242$. The value from the outlet plane was not considered when determining the Nusselt due to the possible numerical error.

For $Re = 492$, the mean temperatures along the channels are shown in Figure 6.23 for the developing flow. The difference between the straight and helical channels is a bit more prominent for $Re = 492$. There is a clear variation in the mean outlet temperature of the straight and helical channels; all three helical channels reach a higher mean temperature than the straight channels.

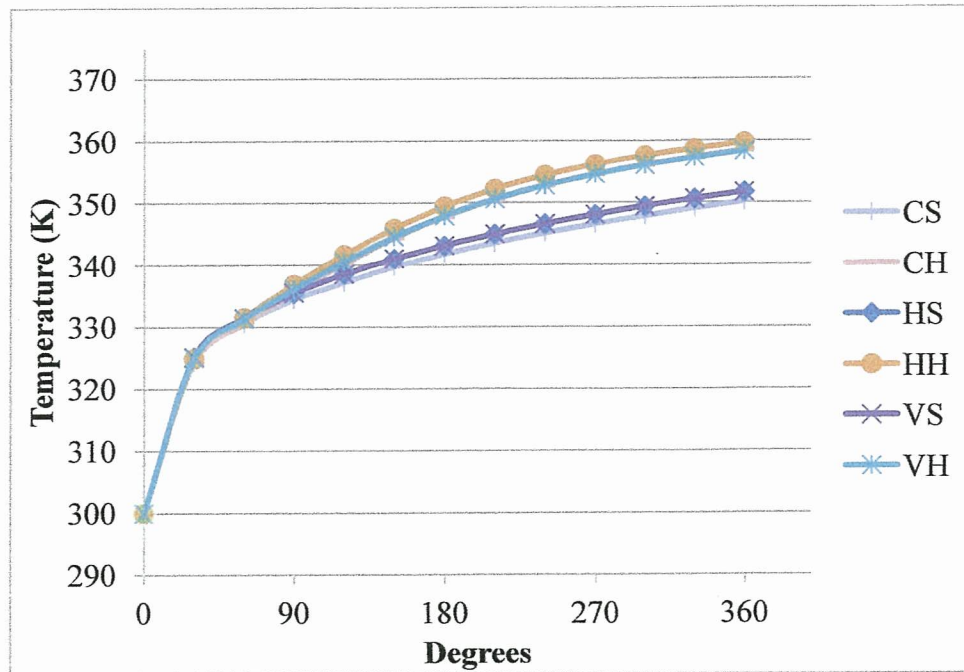


Figure 6.23: Mean Temperature Comparison for $Re = 492$, $De = 263.0$

Both the circular helix and vertical elliptical helix reach a temperature difference of approximately 58 K, while the horizontal elliptical helix has an increase of temperature of 59.68 K. The Nusselt numbers for $Re = 492$ are plotted against one another to observe the differences in heat transfer capabilities in Figure 6.24. The straight channel cases level off close to the value $Nu = 3.66$, as expected. The Nusselt number value for the helical channel cases is slightly higher than for $Re = 242$. The values are between 7.0 and 9.0, with the horizontal elliptical helix model on the higher end of the range. This makes

sense as the mean outlet temperature was the highest for the horizontal elliptical helix model. The same numerical error is noted at the outlet plane with the Nusselt number increasing at this plane, this plane was not included in the calculation of the Nusselt number.

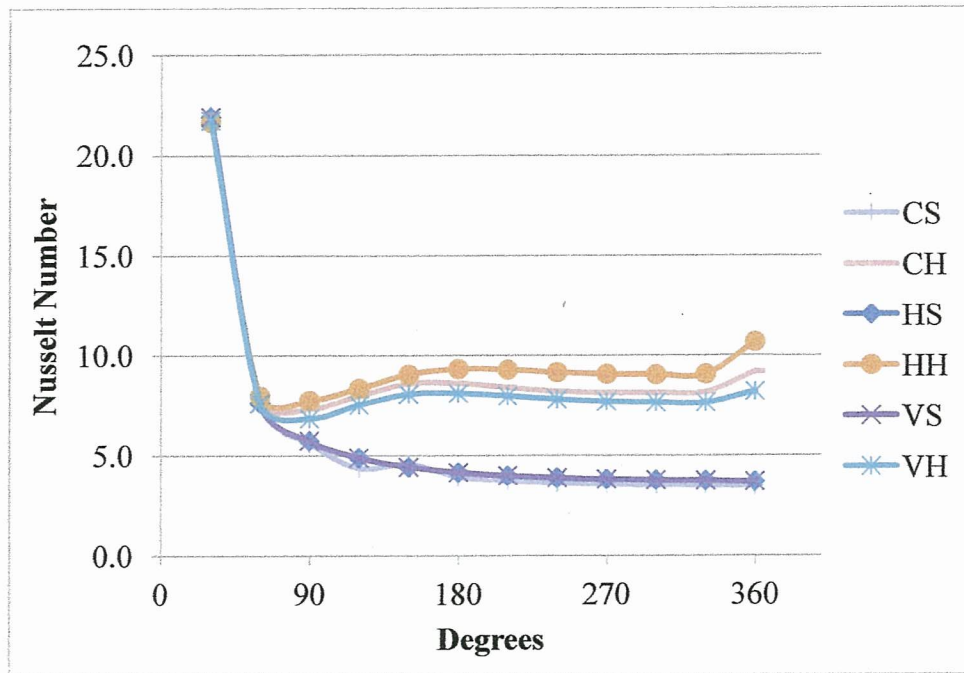


Figure 6.24: Nusselt Number Comparison for Re = 492, De = 263.0

The mean temperatures for all cases for Re = 900 are shown in Figure 6.25. The straight elliptical channels both have an outlet-inlet temperature difference of 44.08 K, while the straight circular channel only rises 42.66 K. The helical cases get to higher values with the horizontal elliptical helical case being the highest with a temperature difference of 55.40 K. The circular helix rises 53.74 K from inlet to outlet and the smallest temperature difference of 53.29 K is the vertical elliptical channel.

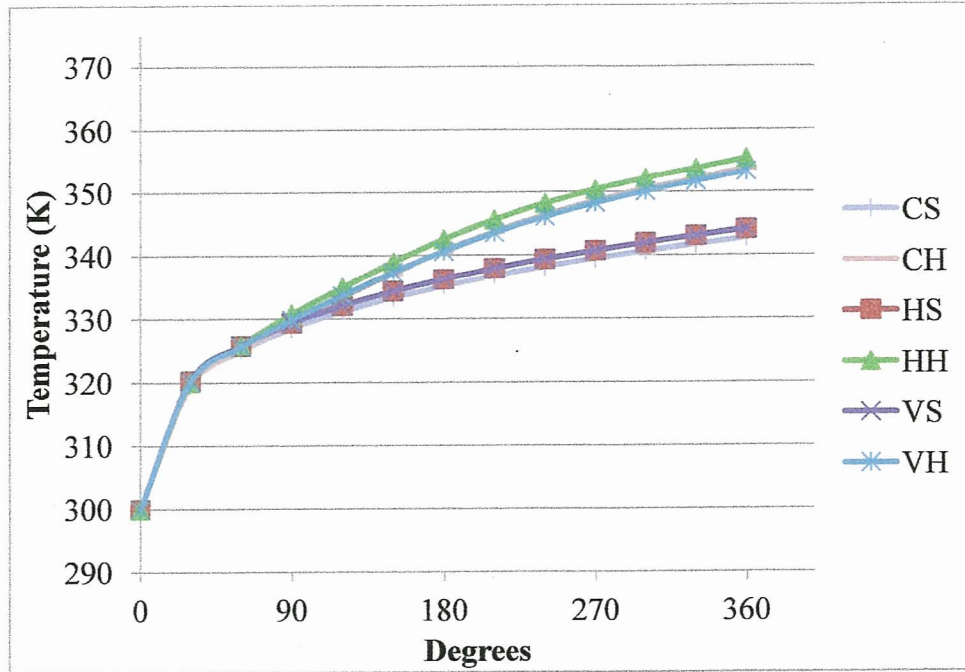


Figure 6.25: Mean Temperature Comparison for $Re = 900$, $De = 481.1$

The mean outlet temperatures for these cases do not reach as high of a temperature as those for $Re = 242$ or $Re = 900$. This is due to the higher velocity of the fluid, the fluid flows faster through the channel, giving it less contact time with the heat source along the channel wall. The Nusselt numbers are plotted in Figure 6.26 for $Re = 900$. The values for the straight channels flatten out around the value of $Nu = 3.66$. The Nusselt numbers are highest for the helical cases for $Re = 900$ with the values ranging from 10.0 to 12.0. Again, a possible numerical error is noted at the outlet of the channel and this value is not taken into consideration for the Nusselt number for the specified helical geometries. The horizontal elliptical helix case has the highest Nusselt number, which is expected as it had the highest temperature increase of all the geometries.

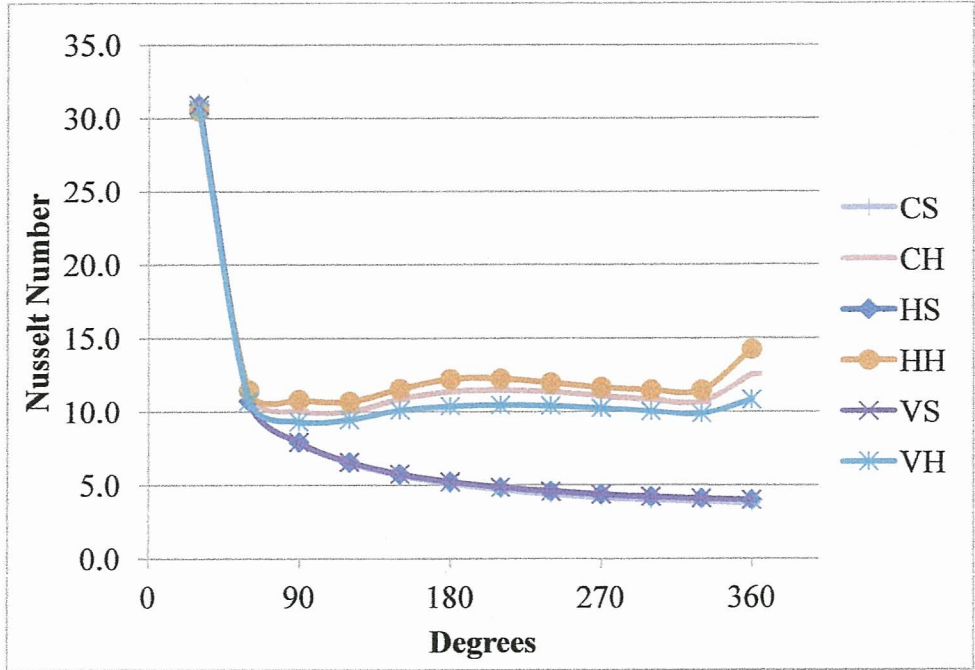


Figure 6.26: Nusselt Number Comparison for Re = 900, De = 481.1

A summary of the outlet-inlet temperature differences in degrees Kelvin for all of the straight and helical geometries is shown in Table 6.3. The percent increases of the helical models over their straight model counterparts are shown below the temperature difference values.

	CS	CH	HS	HH	VS	VH
Re = 242	58.48	61.76 5.6%	59.45	62.08 4.4%	59.45	61.80 3.9%
Re = 492	50.14	58.43 16.5%	51.67	59.60 15.5%	51.67	58.32 12.9%
Re = 900	42.66	53.74 26.0%	44.08	55.40 25.7%	44.08	53.29 20.9%

Table 6.3: Outlet-Inlet Temperature Difference (K) Summary

The largest temperature differences are shown for the horizontal elliptical helix models for each tested Reynolds numbers. Although, it should be noted that the circular helical model had a higher percentage increase for the temperature difference compared to its straight model. A summary of the Nusselt number for the cases is shown in Table 6.4.

	CS	CH	HS	HH	VS	VH
Re = 242	3.49	6.26	3.70	6.60	3.70	5.92
Re = 492	3.46	8.16	3.69	9.05	3.69	7.62
Re = 900	3.74	10.71	3.99	11.49	3.99	9.87

Table 6.4: Nusselt Number Summary

The Nusselt number for a straight channel with an applied uniform surface temperature is 3.66. All of the straight models produced values close to this expect value, confirming that the data is sufficient. The helical models produce higher Nusselt numbers than the straight models with the value of the Nusselt number increasing as the Reynolds number increases. The horizontal elliptical helix model had the highest Nusselt number, 11.49, which is to be expected as it had the largest outlet-inlet temperature difference.

Another item to consider before selecting a design is the friction factor of the model. The friction factor is based on the pressure drop through the channel. The friction factor for each model is shown in Table 6.5.

	CS	CH	HS	HH	VS	VH
Re = 242	0.176	0.216	0.198	0.233	0.195	0.232
Re = 492	0.083	0.125	0.093	0.138	0.093	0.129
Re = 900	0.044	0.080	0.050	0.089	0.050	0.081

Table 6.5: Friction Factor Summary

The friction factor decreases as the Reynolds number increases for all cases. The helical cases do exhibit an increase in the friction factor, with the horizontal elliptical helix cases having the largest friction factor for each Reynolds number. The helical models all had higher Nusselt numbers than their corresponding straight models, so increase in heat transfer comes with an increase in friction along the channel as well.

In order to determine which model produces the best heat transfer relative to its friction factor, a figure of merit was produced to compare the models. The figure of merit, F_M , is the ratio of the Nusselt number to the friction factor. The figure of merit is shown in Figure 6.27. The figure of merit increases as the Reynolds number increases for every case. The circular helix model produced the highest figure of merit due to a large temperature difference through the channel and a low friction factor.

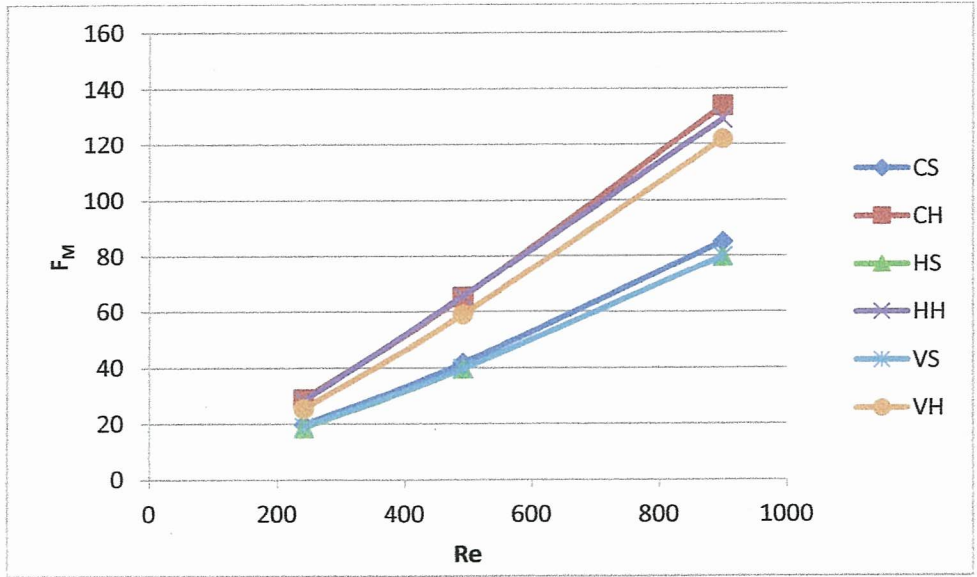


Figure 6.27: Figure of Merit

CHAPTER VII

180° CIRCULAR CHANNEL

7.1 Computational Models

Straight pipe heat exchangers can take up a lot of space. To conserve space when designing heat exchangers, turns are added in the pipes. Two models were created to simulate a 180° degree turn in a channel with a circular cross-section. The first model is a smooth curved 180° turn with a curvature radius of 88.9 mm. The second model is a combination of three circular channels creating a more squared 180° degree turn in the full channel. The two parallel channels of the combination channel are the same distance apart as the straight portions of the curved channel, 177.8 mm. Both circular cross sections have a diameter of 25.4 mm. The two models can be seen in Figure 7.1. The inlet for each channel is shown in blue and the outlet is shown in red.

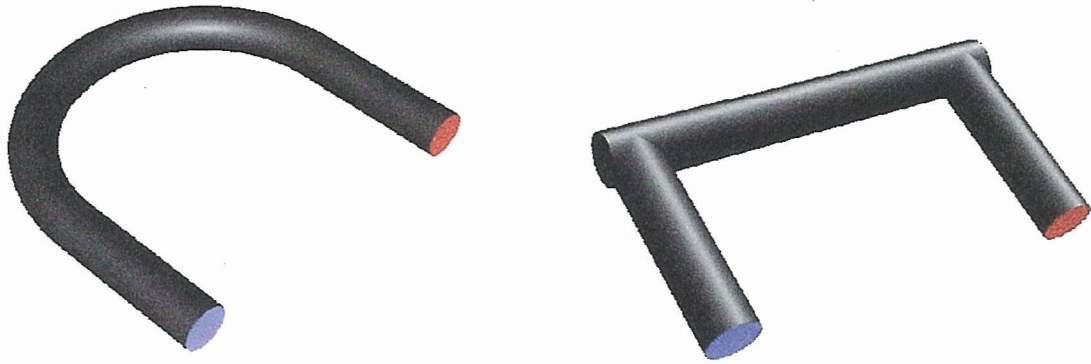


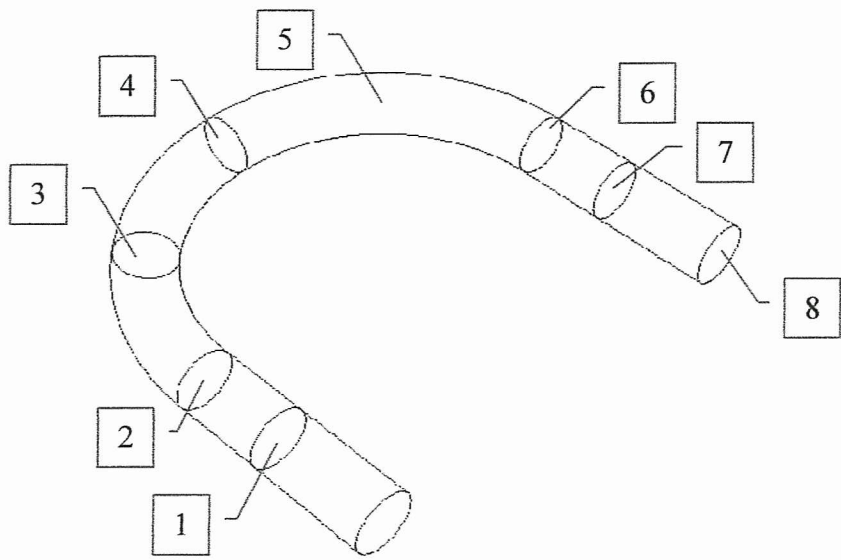
Figure 7.1: 180° Circular Channel Models

Both geometries have their benefits when it comes to manufacturing. The smooth curve would be easier to make for a standalone channel as it would only require the bending of a pipe. The combination of the three channels would be easier to manufacture if the pathway was within a solid part. These computational models will compare the advantages and disadvantages of the two models. Information for each case is shown in Table 7.1.

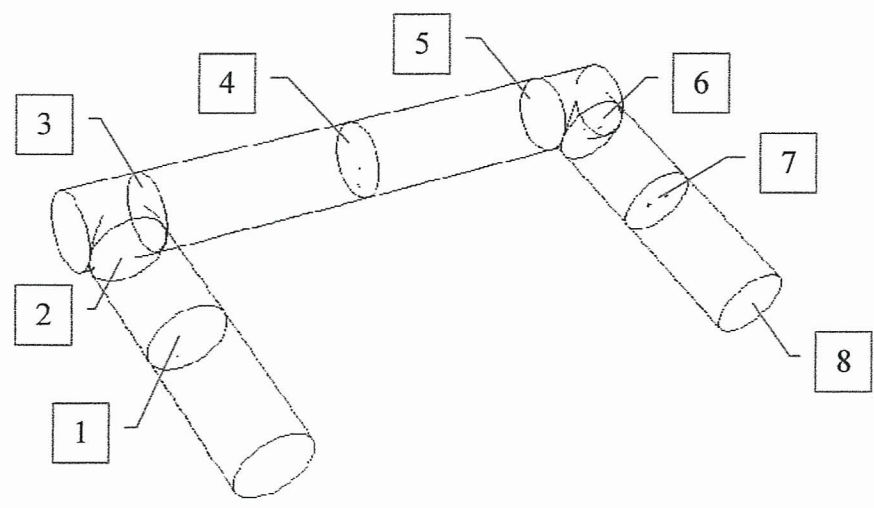
Model	Curved 180° Turn			Squared 180° Turn		
Abbreviation	CT			ST		
Diameter	25.4 mm			25.4 mm		
Curvature Radius	88.9 mm			N/A		
Curvature Ratio	1/7			N/A		
Length	457.1 mm			381.0 mm		
Inlet Velocity	0.1468 m/s	0.2985 m/s	0.5461 m/s	0.1468 m/s	0.2985 m/s	0.5461 m/s
Reynolds Number	242	492	900	242	492	900
Dean Number	129.4	263	481.1	N/A	N/A	N/A
Inlet Temperature	300 K					
Surface Temperature	360 K					

Table 7.1: 180° Circular Channel Summary

For these models, the mean temperature and the pressure are taken at the cross sections shown in Figure 7.2. The mean temperature and pressure at the outlet is also considered.



(a)



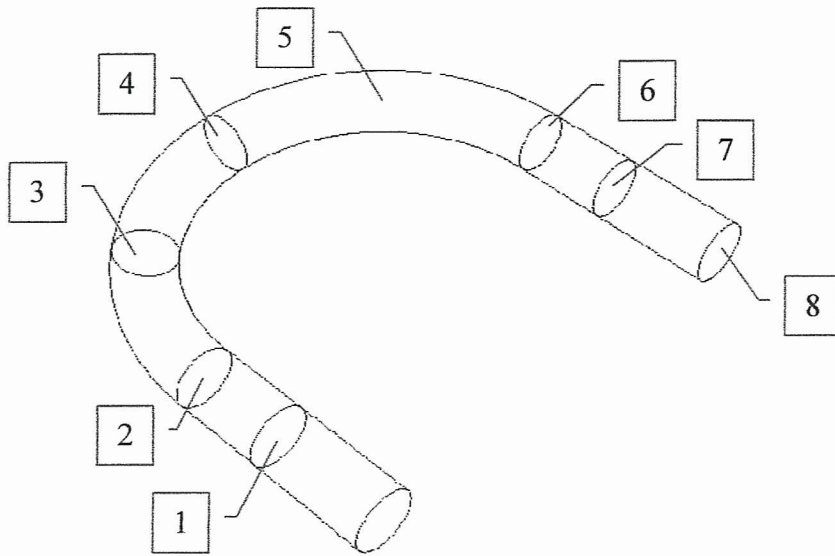
(b)

Figure 7.2: Cross Sectional Planes for (a) Curved Channel and (b) Squared Channel

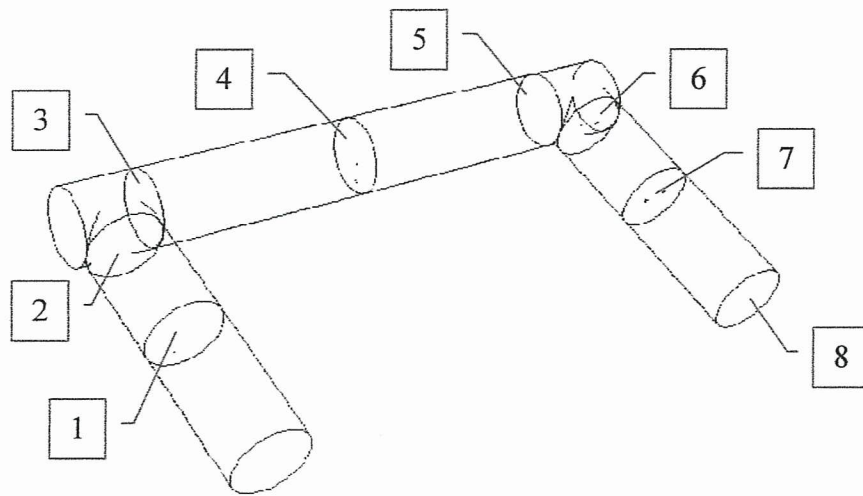
Model	Curved 180° Turn			Squared 180° Turn		
Abbreviation	CT			ST		
Diameter	25.4 mm			25.4 mm		
Curvature Radius	88.9 mm			N/A		
Curvature Ratio	1/7			N/A		
Length	457.1 mm			381.0 mm		
Inlet Velocity	0.1468 m/s	0.2985 m/s	0.5461 m/s	0.1468 m/s	0.2985 m/s	0.5461 m/s
Reynolds Number	242	492	900	242	492	900
Dean Number	129.4	263	481.1	N/A	N/A	N/A
Inlet Temperature	300 K					
Surface Temperature	360 K					

Table 7.1: 180° Circular Channel Summary

For these models, the mean temperature and the pressure are taken at the cross sections shown in Figure 7.2. The mean temperature and pressure at the outlet is also considered.



(a)



(b)

Figure 7.2: Cross Sectional Planes for (a) Curved Channel and (b) Squared Channel

7.2 Fluid Flow Results

The same three Reynolds numbers are used for these channels, $Re = 242, 492,$ and 900 . The velocity profiles for the smooth curved channel should develop similarly to the previous cases in this thesis. The sharp turns of the squared channel could cause some turbulence within the fluid. The outer wall of the channel is always shown to the left in the figures.

For $Re = 242$, the smoothly curved channel develops as expected as shown in Figure 7.3. The location of the maximum axial velocity shifts towards the outer wall of the channel and the profile is symmetric across the horizontal mid-plane. Two Dean vortices develop in the upper and lower halves of the channel and these also appear symmetric. There is definitely a difference in the flow development for the squared curve. Entering the first 90° turn at plane 2, the location of the maximum axial velocity shifts towards the inner wall of the channel. As the fluid comes out of the first 90° turn at plane 3, the location of the maximum axial flow shifts back towards the center of the channel and the velocity profile is not as smooth along the inner wall of the channel. At plane 4, the velocity profile closely resembles that of the smooth curve with the location of the maximum axial velocity shifting towards the outer wall of the channel. The velocity profile at plane 5 looks similar to that at plane 2 with the location of the maximum axial velocity moving back toward the inner wall of the channel. When the fluid exits the second 90° turn at plane 6, it also resembles the prior turn at plane 3; the location of the maximum shifts back towards the center of the channel. Plane 7 and the outlet is similar to the profiles for the smooth curve, with the outlets appearing nearly identical, but with a slightly higher maximum velocity value for the smooth channel.

Dean vortices develop, but are not always present at each plane. In planes 2 and 5, where the location of the maximum velocity has shifted towards the inner wall, the vortices disappear and the velocity vectors actually change direction and go towards the inner wall. By the time the fluid has reached the outlet of the channel, the vortices in both the smooth and squared channel look alike.

For $Re = 492$, the results from the smooth curve resemble those from $Re = 242$, which can be seen in Figure 7.4. The location of the maximum velocity shifts forwards the outer wall of the channel and is symmetric about the horizontal mid-plane of the channel. Two Dean vortices develop in the upper and lower halves of the channel appear to be symmetric. The flow in the squared curve develop similar to that for $Re = 242$. At planes 2 and 5, the location of the maximum axial velocity shifts towards the inner wall of the channel. There is disturbance along the inner wall as the location of the maximum shifts back towards the middle at planes 3 and 6. At plane 4 and at the outlet the velocity profiles are similar to that of a curved channel, with the maximum velocity shifting towards the outer channel wall. There is a slight variance at plane 7 as the velocity profile has created a pocket of slower axial velocity in the center of the channel. The outlet profile of both channels is similar, but the smooth curve reaches a slightly higher maximum axial velocity. Two Dean vortices develop in the flow, but at places 2 and 5, the direction of flow reverses within the plane and the vortices disappear. By the outlet of the squared channel, two identical symmetric vortices are shown and appear very similar to those at the outlet of the smooth curved channel.

Figure 7.5 shows the flow development for the two channels for a $Re = 900$. There appears to be more disturbances in the developing velocity profiles at the higher

velocity. The flow begins to develop similar to the previous two cases through plane 3. At plane 4, the velocity profile curls in on itself and the location of the maximum axial velocity is in the outer upper quadrant of the channel and the profile is no longer symmetric about the horizontal mid-plane. The maximum shifts back towards the inner wall of the channel at plane 5, but the profile is not as smooth as the previous cases and it is not quite symmetric. There is more disturbance coming out of the second turn at plane 6, the maximum begins to shift towards the center again although slightly above the horizontal mid-plane. At plane 7 the axial velocity profile appears more symmetric, but again, a pocket of slower axial velocity has developed in the center of the channel. The axial velocity profile at the outlet transitions to more typical profile with the higher velocity fluid in the middle of the channel. Like the two previous cases, two Dean vortices develop within the flow. These vortices disappear and the axial velocity changes direction in the planes 2 and 5 as was seen with the two other cases. There is a slight change to the vortices at plane 4, the vortices shift towards the outer upper quadrant and the inner lower quadrant and are no longer symmetric about the horizontal mid-plane. The two vortices reappear as the fluid comes out of the second turn of the channel, although they are still not quite symmetric about the mid-plane, but are more symmetric across the diagonal from the outer upper quadrant to the inner lower quadrant.

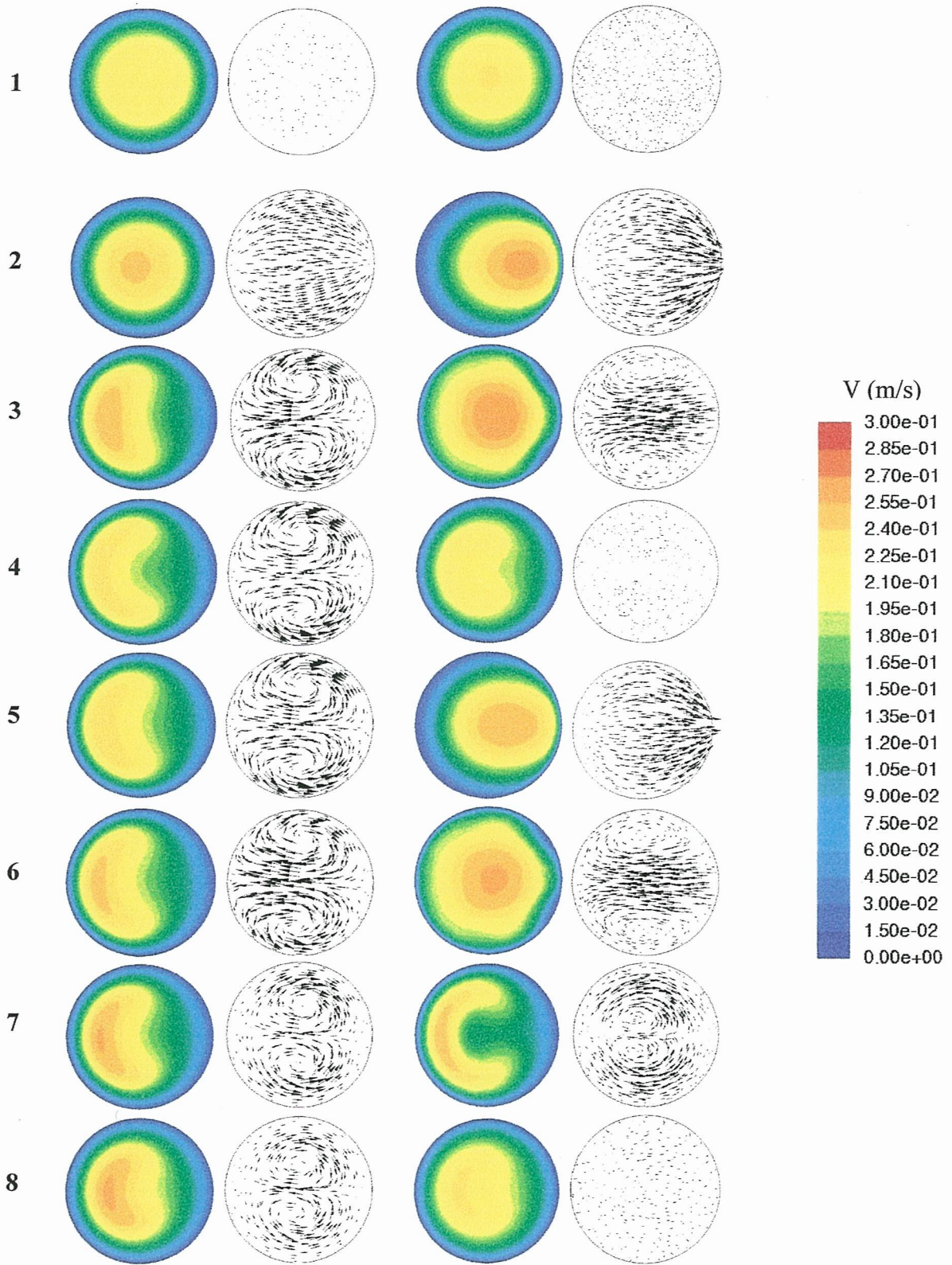


Figure 7.3: Developing Axial Velocity Profiles in 180° Channel ($Re = 242$)

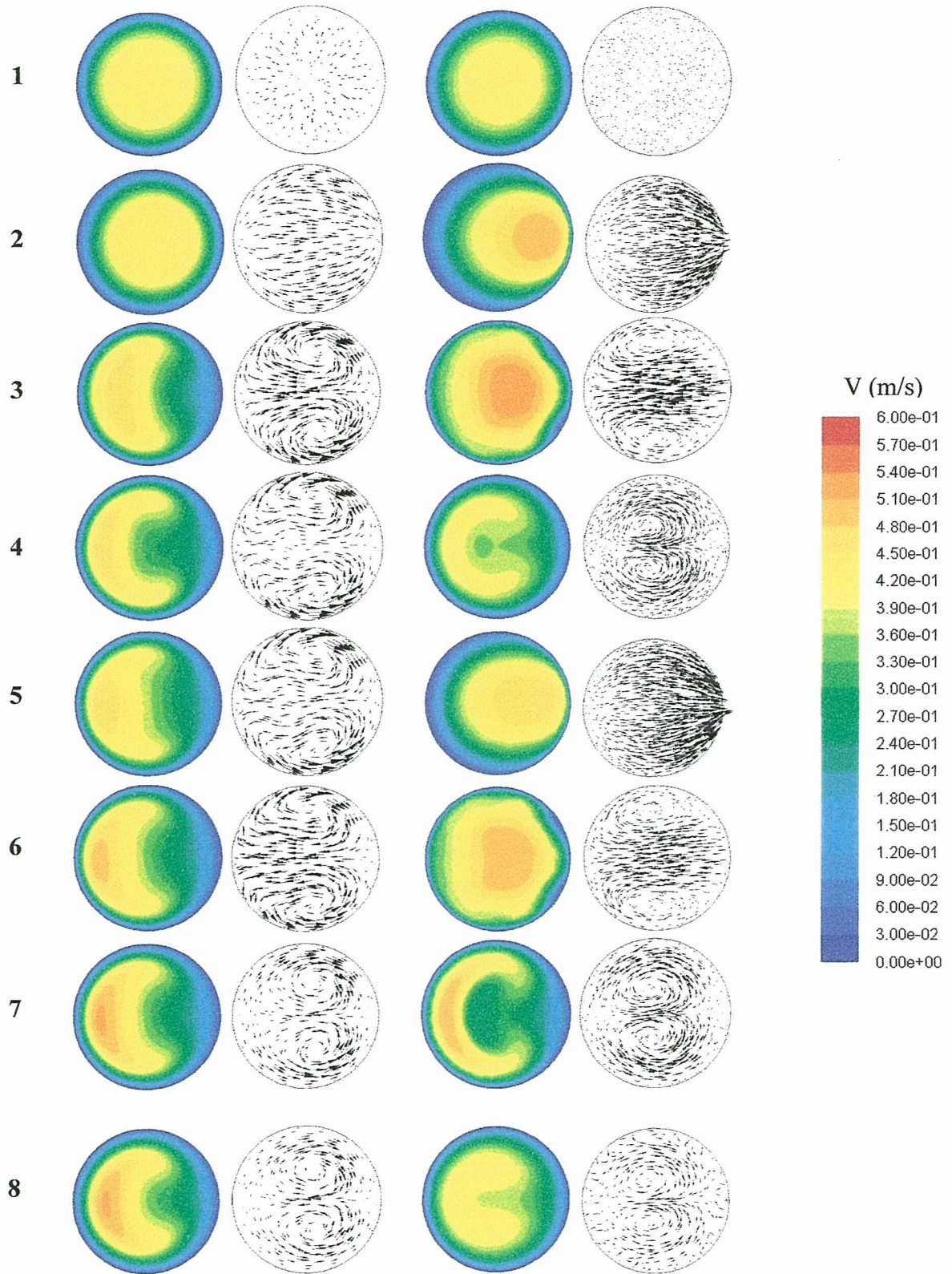


Figure 7.4: Developing Axial Velocity Profiles in 180° Channel ($Re = 492$)

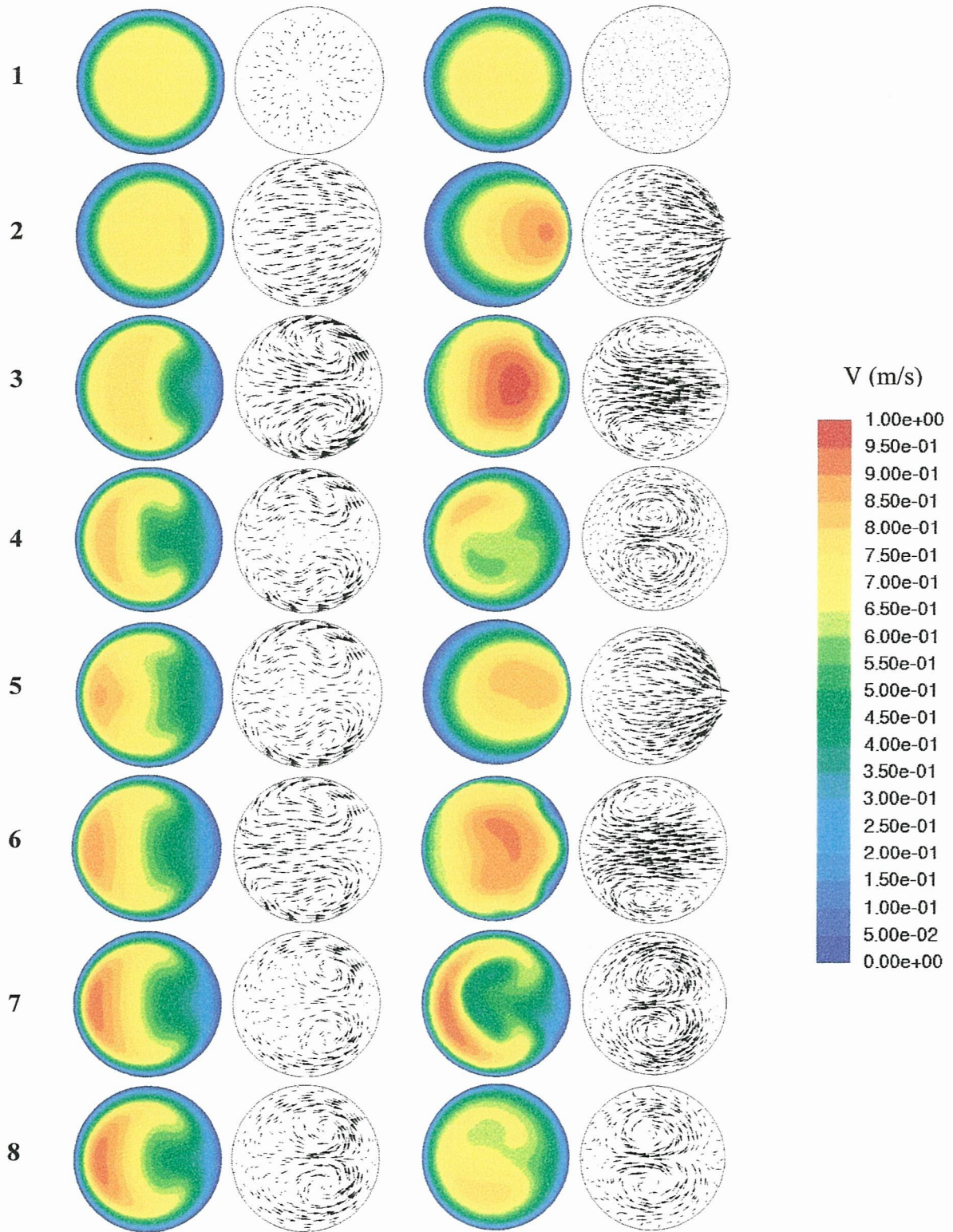


Figure 7.5: Developing Axial Velocity Profiles in 180° Channel ($Re = 900$)

7.3 Heat Transfer Results

Although the squared channel may be easier to manufacture for an internal channel, its use must consider if this squared design can produce the same or better results than the rounded curve. As these channels would most commonly be used in heat exchanger applications, a constant surface temperature of 363 K is applied to each of the channels for each of the three Reynolds numbers. The fluid enters the inlet at a uniform temperature of 300 K. The developing temperature profiles are shown with the smooth curved channel on the left and the squared channel on the right. The outer wall of the channel is shown to the left for each cross section. The mean temperature at each cross section is plotted by distance along the length of the channel. The distance along the channel is non-dimensionalized for comparison; 0.00 being the inlet of each channel and 1.00 being the outlet.

For $Re = 242$, the temperature profile develops as expected, with the secondary flow pushing the cooler fluid towards the outer wall allowing it to come into contact with the heat source as seen in Figure 7.6. The location of the coolest fluid temperature moves around in the squared channel as the fluid moves downstream. At plane 4 the temperature profile looks as if the fluid was traveling through a typical straight channel. The mean temperatures along the channel are shown in Figure 7.7. By the outlet, the temperature profiles are nearly identical and both mean temperatures are the same at 360 K. Using the exact values, there is only a temperature difference of 0.4% in favor of the curved channel.

The increased velocity for $Re = 492$ produces slightly different results for the squared channel. The temperature profiles, shown in Figure 7.8, develop similarly to the

associated velocity profiles for the smooth curved channel. The location of the coolest fluid shifts around within the channel. At planes 4 and 7, the temperature profiles look very similar to its smooth curve channel counterparts. There is some disturbance within the fluid as it exits out of the two 90° turns at planes 3 and 6. This interruption in flow causes the fluid to mix, which results in only a slight temperature increase across the plane, but dispersing the heat across the fluid. In Figure 7.9, the mean fluid temperature fluctuates as the fluid goes through the two 90° turns. Even with the temperature fluctuation, the squared channel has a higher outlet-inlet temperature difference of 56.70 K, the smooth curve channel only rises 54.83 K by the outlet. This is an increase of 3.7%.

For $Re = 900$, the temperature profiles develop in a similar fashion to the cases for $Re = 492$ as shown in Figure 7.10. The same disturbance is seen coming out of the turns at planes 3 and 6. Due to the higher velocity of the fluid, this disturbance does not have as large of an effect on the mean fluid temperature, as there is not as large of a fluctuation as there was for $Re = 492$. The mean temperatures are shown for both channels in Figure 7.11. The outlet profiles for both channels are similar, but the squared channel again has a higher temperature difference, 53.55 K, than the smooth curve channel, 48.81 K which is an increase of 9.7%.

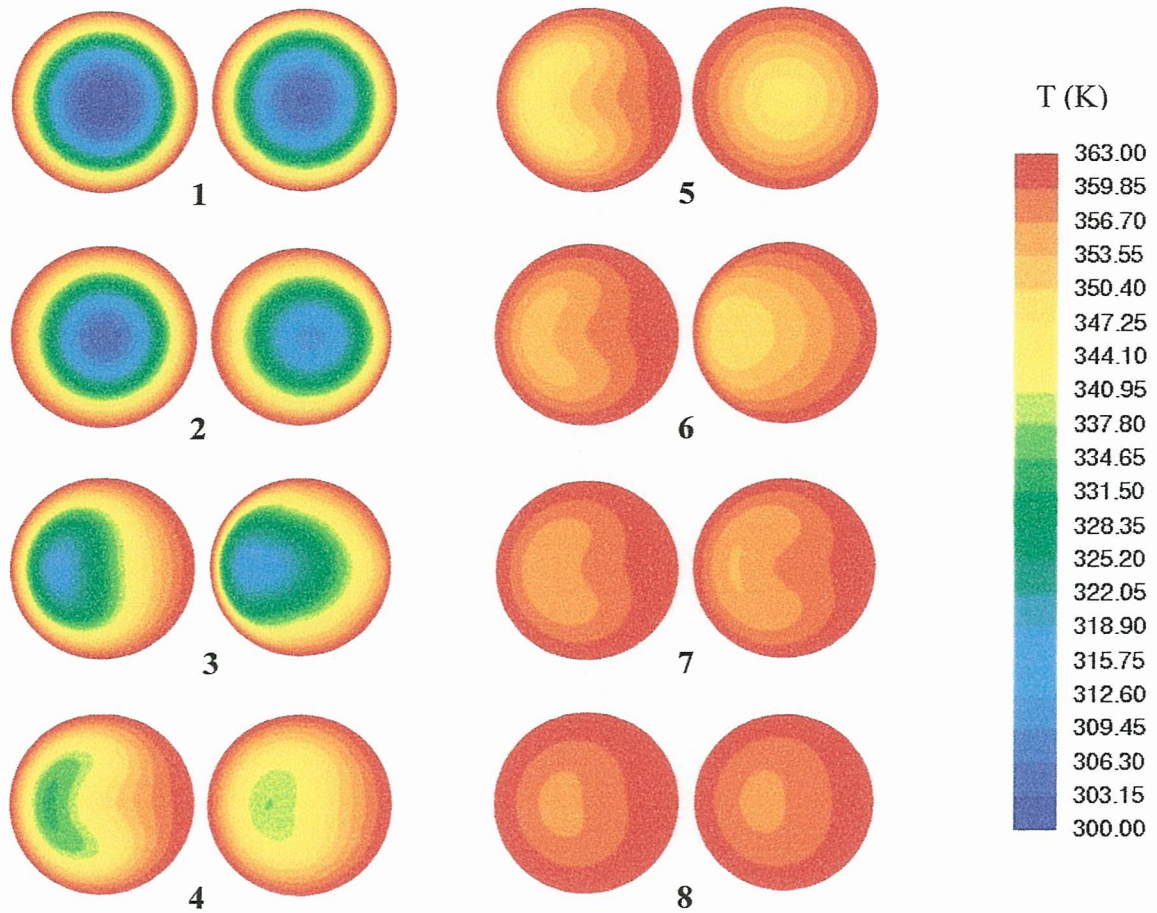


Figure 7.6: Developing Temperature Profiles in a 180° Channel ($Re = 242$)

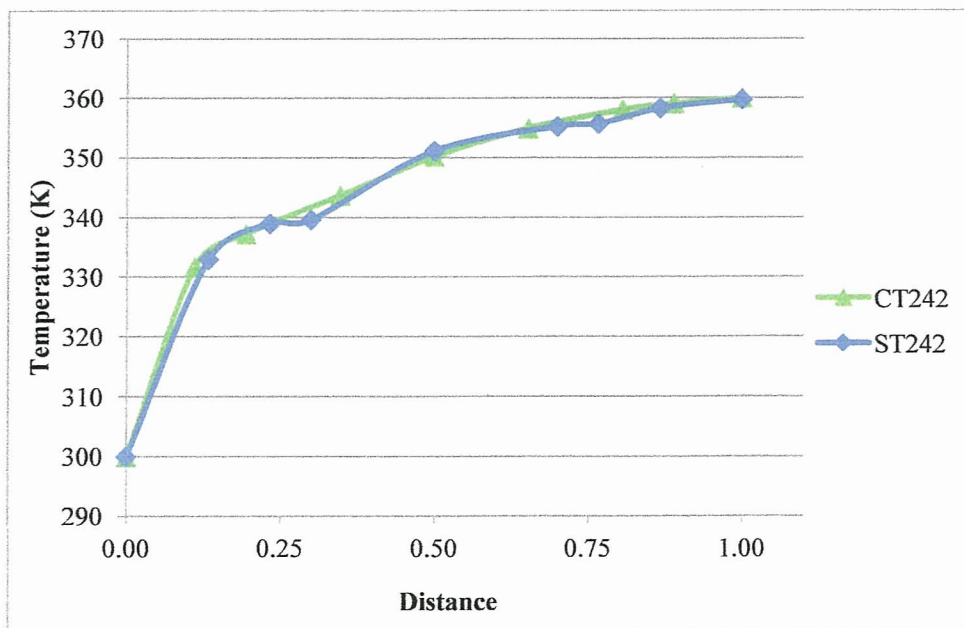


Figure 7.7: Mean Temperature in a 180° Channel ($Re = 242$)

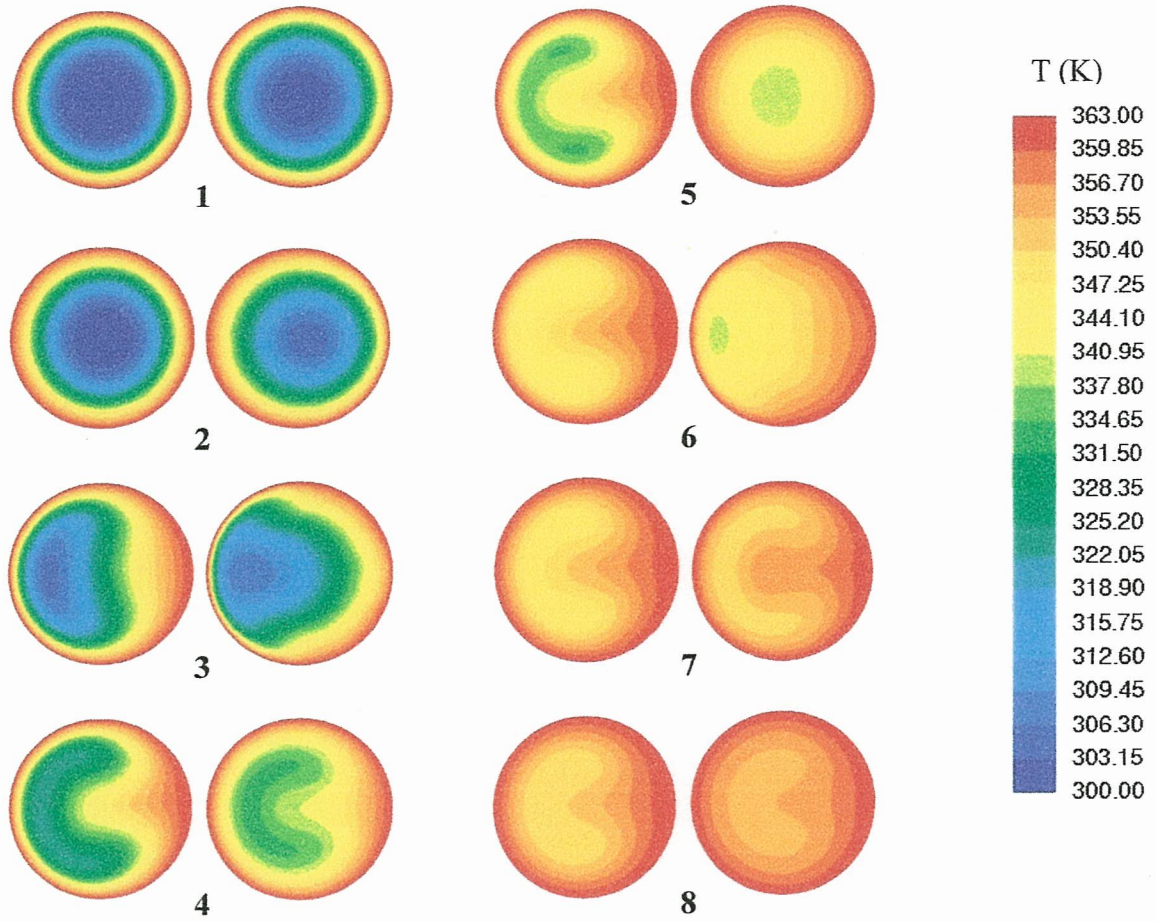


Figure 7.8: Developing Temperature Profiles in a 180° Channel ($Re = 492$)

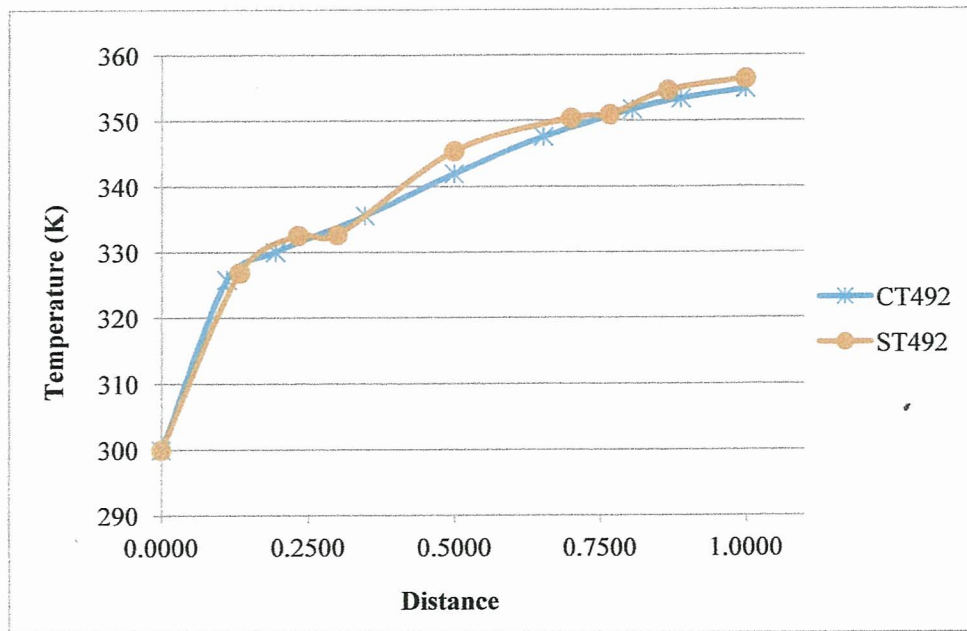


Figure 7.9: Mean Temperature in a 180° Channel ($Re = 492$)

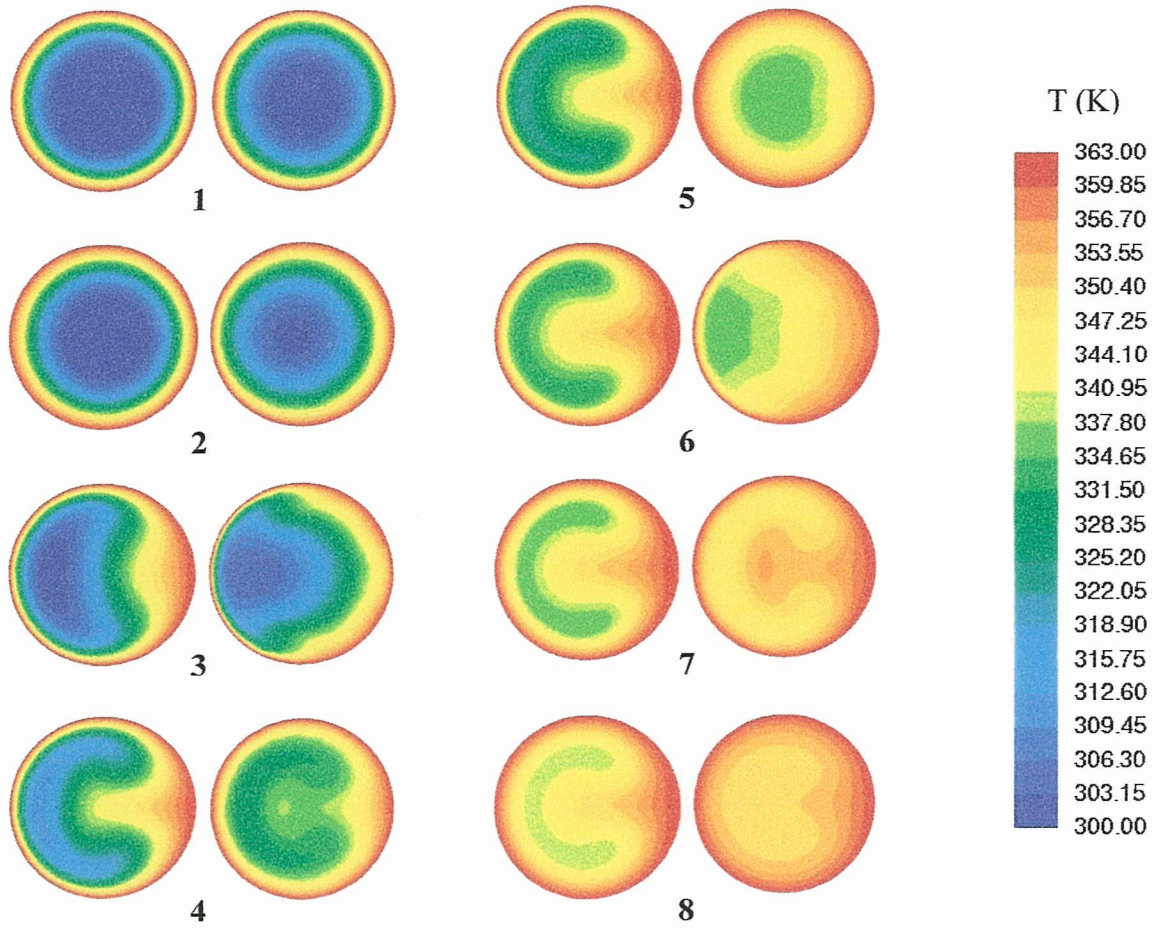


Figure 7.10: Developing Temperature Profiles in a 180° Channel ($Re = 900$)

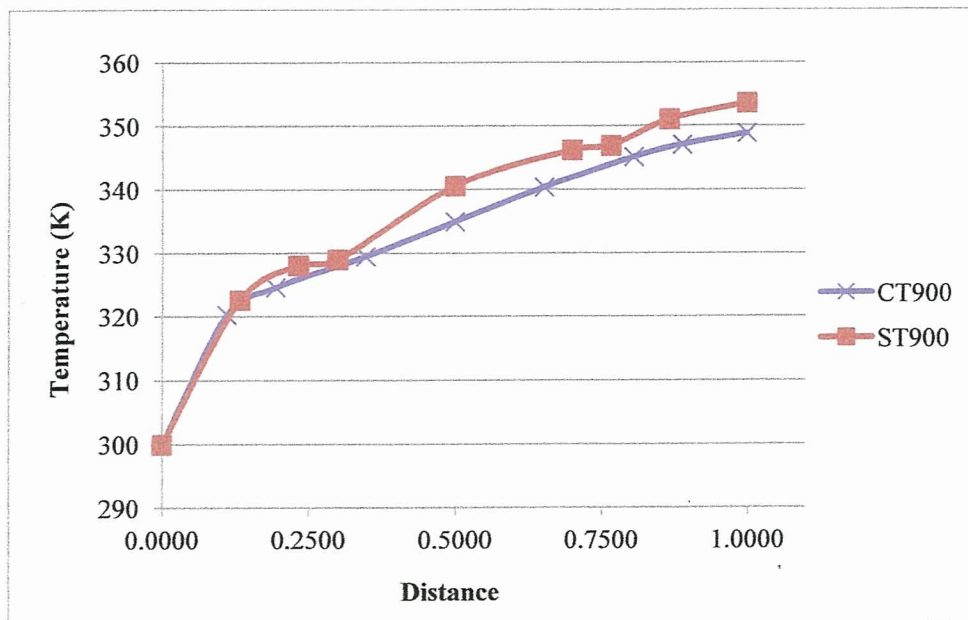


Figure 7.11: Mean Temperature in a 180° Channel ($Re = 900$)

The temperature differences in Kelvin are summarized for both models in Table 7.2.

	CT	ST
Re = 242	59.96	59.71
		-0.4%
Re = 492	54.83	56.37
		3.0%
Re = 900	48.81	53.55
		9.7%

Table 7.2: Temperature Difference Summary for 180° Channel

For $Re = 242$, the temperature difference is nearly identical with the curved channel producing a slightly higher difference, an increase of only 0.4% over the square channel.

At higher Reynolds numbers, the square channel produces a higher outlet-inlet temperature difference with an increase of 3.0% for $Re = 492$ and 9.7% for $Re = 900$ over their curved counterparts.

CHAPTER VIII

CONCLUSIONS

8.1 Conclusions

Computational models were created for helical channels for two different geometric cross sections: a circle and an ellipse with the same cross-sectional area. The elliptical cross section was analyzed for the major axis of the ellipse in both the horizontal and vertical positions. All the cases were studied for three different Reynolds numbers (242, 492, and 900) and keeping the Dean number for each case below 522 for stability purposes. A constant surface temperature of 360 K was applied along the entire length of the channel to determine how the Dean vortices within the flow affect the heat transfer properties of the fluid. Straight channels with the same geometric cross section and of equivalent length were also modeled for comparison.

In each case, the helical models had a higher Nusselt number and outlet-inlet temperature difference than their straight model counterpart, with percent increases ranging from 3.9-26.0%. The higher percentage increases coincided with the higher Reynolds numbers. The secondary flow within the fluid helps to distribute the heat within the fluid allowing it to reach a higher temperature more quickly. The horizontal elliptical helix model had the highest outlet-inlet temperature difference of all of the

helical models for each Reynolds number. This large temperature difference also resulted in the highest Nusselt number for each Reynolds number for this geometry. Although the horizontal elliptical helix model had the highest temperature difference and Nusselt number, it also produced the highest friction factor out of all the models for each Reynolds number. The circular helical model actually produced the highest percentage increase in temperature difference over its straight counterpart. The figure of merit which compares the Nusselt number to the friction factor shows that the circular helical model has the highest value for every Reynolds number. This makes this cross-sectional geometry the best design choice out of these cases.

Two other computational models were studied for two channels each with a 180° turn. The first was a smooth rounded curve and the second combined three channels with perpendicular intersections. Both channels had the same circular cross section and were analyzed for the same three Reynolds numbers as the helical cases. The same constant surface temperature of 360 K was applied along the entire length of both channels. For lower Reynolds numbers, the channels had approximately the same mean outlet temperature. The curved channel had a slightly higher outlet-inlet temperature difference, a 0.4% increase over the square channel. At the higher Reynolds numbers, the squared channel achieved a higher outlet-inlet temperature difference due to the turns of the channel causing a disturbance within the fluid. This disturbance allowed the fluid to mix and distribute the heat across the fluid. The squared channel may be a more efficient design as it produces a higher outlet-inlet temperature difference, but manufacturing capabilities need to be considered before settling on the design. The squared channel produced an increase of 3.4-9.7% to the temperature difference across

the channel. At lower Reynolds numbers, the results are nearly identical, so either channel design could be used, so whichever design has the lower manufacturing costs is desirable. For higher Reynolds numbers, the square channel produces a higher temperature difference across the channel. The manufacturing costs need to be considered, but they increase in outlet-inlet temperature difference of the square channel may lead this geometry to be a better design.

8.2 Future Work

All of the models had undeveloped flow profiles at the inlet with Dean numbers below 522. Keeping the Dean number below 522 keeps the fluid in a stable state. It would be interesting to look at other laminar flows with Dean numbers above 522 to see how the secondary flow develops and affects the heat transfer. At Dean numbers above 522, it is possible for more than two Dean vortices develop; these additional vortices for further aid in the heat transfer properties of the fluid. Other heat transfer cases such as a surface temperature only applied at certain points of the channel, to take advantage of the secondary flow at its strongest points. Also, a constant heat flux situation could be observed to see the effects.

Turbulent flow was not considered in this thesis, but would be another topic for research. The chaotic behavior associate with turbulent flow could further aid in the heat transfer properties of the fluid. As was shown, the percent difference increased as the Reynolds number increased, so it could be implied that the difference between helical and straight models would further differentiate as the Reynolds number increased for laminar flow models. It could be tested to see if this trend continues into the turbulent flow regime. Most of the turbulent flow data that has been done has been for circular or

rectangular channels, similar to the laminar flow data. It would be interesting to see how the turbulent flow behaves in the elliptical channels.

REFERENCES

1. Agrawal, A. T. (1978). Laser anemometer study of flow development in curved circular pipes. *Journal of Fluid Mechanics* , 85 (Part 3), 497-518.
2. Cengel, Yunus A., and John M. Cimbala. 2010. *Fluid Mechanics: Fundamentals and Applications*. 2nd Ed. McGraw-Hill. New York.
3. Dean, W.R. (1928). Fluid Motion in a Curved Channel. *Proceedings of the Royal Society of London. Series A, Containing Papers of a Mathematical and Physical Character*, 121(787), 402-420.
4. Germano, M. (1982). On the effect of torsion on a helical pipe flow. *Journal of Fluid Mechanics*, 125, 1-8.
5. Germano, M. (1989). The Dean equations extended to a helical pipe flow. *Journal of Fluid Mechanics*, 203, 289-305.
6. Grundmann, R. (1985). Friction diagram of the helically coiled tube. *Chemical Engineering and Processing* , 19, 113-115.
7. Jayakumar, J. S. (2008). Experimental and CFD estimation of heat transfer in helically coiled heat exchangers. *Chemical Engineering Research and Design*, 86 (3), 221-232.
8. Kays, William, Michael Crawford, and Bernhard Wiegand. 2005. *Convective Heat and Mass Transfer*. 4th Ed. McGraw Hill. New York.
9. Nobari, M. E., and E. Amani (2009). A numerical investigation of developing flow and heat transfer in a curved pipe. *International Journal of Numerical Methods for Heat and Fluid Flow*, 19 (7), 847-853.
10. Siggers, J.H. and S.L. Waters (2005). Steady flows in pipes with finite curvature. *Physics of Fluids*, 17, 077102.
11. Yang, Zhong-hua, and H.B. Keller (1986). Multiple Laminar Flows Through Curved Pipes. *Applied Numerical Mathematics*, 2, 257-271.
12. Zitny, R, et al. (2004). Heat Transfer Enhancement and RTD in Pipes with Flow Inversion. *Heat Transfer Engineering*, 25 (4), 67-79.